Development of a Propeller Source Noise Model

M. Haddaoui

Technische Universiteit Delft

TU Delft Delft University of Technology

Challenge the future

Development of a Propeller Source Noise Model

by

M. Haddaoui

in partial fulfillment of the requirements for the degree of

Master of Science
in Aerospace Engineering

at the Delft University of Technology,
to be defended publicly on Thursday July 4, 2019 at 1:30 PM.

Student number:	4205596	
Supervisor:	Dr. ir. M. Snellen	
Thesis committee:	Prof. dr. D. G. Simons,	ANCE TU Delft
	Dr. ir. M. Snellen,	ANCE TU Delft
	Dr. ir. R. Vos,	FPP TU Delft
	Dr. ir. M. I. Gerritsma,	Aerodynamics TU Delft

TU Delft Delft University of Technology

Acknowledgments

A long journey has come to an end. I feel blessed that I have had the opportunity to complete a challenging and inspiring study program. My academic career at the TU Delft has come to an end and I will always look back feeling fulfilled. I am grateful for reaching this milestone and this would not have been possible without the support of many important people.

First of all, I would like to express my gratitude to my supervisor Dr.ir. Mirjam Snellen for her guidance, valuable advice and feedback throughout my thesis project. I also wish to thank Prof.dr. Dick Simons for attending the important meetings and for asking valuable questions. I also would like to acknowledge Thijs Bouwhuis who has been a sparring partner for me and was willing to proofread my entire thesis report. Additionally, I would like to thank Dr.ir. Roelof Vos and Dr.ir. Marc Gerritsma for being part of the assessment committee and for their efforts to assess the work that I have conducted during my thesis.

Last but not least, special thankfulness goes to my family members and friends who provided emotional support throughout my studies and life.

M. Haddaoui
Delft, June 2019

Summary

Turboprop engines are known for their high propulsive efficiency and low fuel consumption on short-range missions. With growing concerns about the environmental impact of aircraft, airline companies regained interest in turboprop driven aircraft. A major drawback of turboprops is the noise they produce. At the Aircraft Noise and Climate Effects (ANCE) section at the TU Delft a project in cooperation with the Netherlands Aerospace Centre (NLR) is ongoing. The aim of that project is the further development of the so called "Virtual Community Noise Simulator" (VCNS) tool. This tool already has capabilities to predict and simulate noise of aircraft flyovers in a virtual reality environment. Currently this can only be done for aircraft with a turbofan engine. Therefore NLR is looking for a way to extend the tool by adding the noise prediction capability for propellers driven aircraft. The dominant noise source of a turboprop engine is the propeller. Therefore a noise prediction model for propellers needs to be selected and implemented. The goal of this thesis is to develop a source noise model for propellers which has the future goal of being integrated in a tool like the VCNS or an aircraft design chain.

This thesis has investigated a propeller noise theory called the Helicoidal Surface theory. The propeller noise sources that are taken into account are the harmonic noise sources: steady loading noise and the thickness noise. The propeller noise theory requires several aerodynamic parameters of the propeller. XRotor and XFoil are used to obtain the aerodynamics of the propeller. The Helicoidal Surface theory together with XFoil and XRotor are successfully implemented in Matlab. The tool that is developed is called the HeliX-tool. The assumptions made for the development of the HeliX-tool is that the propeller operates in an isolated configuration and only has an axial inflow.
The validation of the HeliX-tool is divided into the validation of the performance/aerodynamics part of the propeller and the acoustics of the propeller. The validation is performed using literature data and two NLR tools: MAEPROP and Rollac. MAEPROP is used for the validation of the aerodynamics part of the propeller and Rollac is used to generate acoustic results. The propeller that is selected for the validation is the SR-2 propeller. This is a propeller that is developed and extensively researched by NASA. Literature data used for the validation consists of an in-flight measurement and windtunnel measurements. The HeliX-tool is applied for a variety of propeller operating conditions. From the validation it is found that for high local Mach numbers (>0.7 Mach) large deviations are obtained for the aerodynamics of the propeller and hence for the acoustics. This is due to the fact that the HeliX-tool does not have the capabilities to accurately predict the aerodynamics of the propeller at these Mach numbers. XRotor uses a Prandtl-Glauert compressibility correction which should not be applied for Mach numbers higher than 0.7. Furthermore, for high Mach numbers the quadrupole sources become more important as they are used to include non-linear effects. These are not implemented in the current version of the HeliX-tool. Therefore, bad agreement with literature data is found when high Mach numbers are used. For operating conditions that result in local Mach numbers lower than 0.7, good agreement can be generally found with the NLR-tools and literature data. Additional comparisons with the NLR-tools are made to further investigate features of the Helicoidal surface theory like the acoustic non-compactness and the assumptions made regarding the chordwise loading of the propeller blade sections.
The applicability and potential of the HeliX-tool is shown by performing an auralization of a virtual fly-over of a propeller. Auralization is the process of transforming a source noise prediction into an audible result. Several propagation effects are taken into account for this which are the following: ground reflection, spherical spreading, atmospheric absorption and the Doppler frequency shift. A spectrogram and a pressure time signal of 30 seconds are obtained of the propeller fly-over at an altitude of 304.8 meters. Furthermore an audible simulation is generated using the frequency content of the propeller fly-over.

Contents

Nomenclature and Abbreviations

List of Abbreviations

$ANCE$	Aircraft Noise and Climate Effects
$ANOPP$	Aircraft Noise Prediction Program
APU	Auxiliary Power Unit
BPF	Blade passage frequency
DLR	German Aerospace Centre
FA	Face Alignment
FAA	Federal Aviation Administration
INM	Integrated Noise Model
MCA	Mid Chord Alignment
$NASA$	National Aeronautics Space Administration
NLR	Netherlands Aerospace Centre
NPD	Noise-Power-Distance
$OSPL$	Overall Sound Pressure Level
RPM	Revolutions per minute
SPL	Sound Pressure Level
$VCNS$	Virtual Community Noise Simulator

Nomenclature

α	Angle of attack
α_{0L}	Zero-lift angle of attack
β	Blade pitch angle
γ	Specific heat ratio
Γ	Vortex strength
ΔCl	Increment to stall
η	Efficiency
η_{prop}	Propulsive efficiency
θ	Radiation angle
μ	Dynamic viscosity
ρ	Fluid density
ϕ	Local inflow angle
ϕ_s, ϕ_o	Phase lag due to sweep and offset respectively
Ψ	Distribution function
Ω	Angular velocity
B	Number of blades

c	Speed of sound or local blade chord
C_d	Drag coefficient (2D)
C_{d0}	Minimum drag coefficient
C_l	Lift coefficient (2D)
c_{local}	Local blade chord length
$C_{l_{max}}$	Maximum lift coefficient
$C_{l_{min}}$	Minimum lift coefficient
C_m	Pitching moment coefficient
C_P	Power coefficient
C_{pr}	Pressure coefficient
C_Q	Torque coefficient
C_T	Thrust coefficient
D	Propeller diameter
f	Frequency
G	Greens function
J	Advance ratio
J_{mB}	Bessel function of the first kind of order mB
k_x	chordwise non-dimensional wavenumber
k_y	non-dimensional wavenumber
L	Lift
m	Number of harmonics or harmonic number
M_∞, M_x	Freestream Mach number
M_{cr}	Critical Mach number
M_h	Helical tip mach number
M_T	Rotational tip mach number
n	Revolutions per second
P	Power
$P(f)$	Power spectral density
p_{e0}, p_ref	Reference effective pressure
$p(t)$	Pressure time signal
P_{mB}	Fourier coefficients of pressure time signal
Q	Torque
R	Propeller radius
Re_{ref}	Reference Reynolds number
t_b	Maximum thickness to chord ratio
T	Thrust
T_{ij}	Lighthills stress tensor element
V	Velocity
V_∞	Freestream velocity
V_j	Jet velocity

W	Effective velocity
W_a	Freestream velocity of blade element
W_t	Rotational velocity of blade element
$X(f)$	Discrete Fourier Transform
$z, \frac{r}{R}$	Spanwise radial position of blade element

1

Introduction

In the last few decades, turboprops were largely overlooked by commercial carriers. Propeller-driven aircraft were often perceived as loud and outdated. With growing concerns about the environmental impact, airline companies regained interest in propeller-driven aircraft since they may offer solutions to issues jets have trouble addressing. For that reason, turboprop aircraft are making a comeback in the commercial aviation industry, with high fuel efficiency on short-range missions compared to turbofan aircraft. The in-service regional aircraft fleet is approximately shared evenly by the turboprop and regional jets. Aircraft manufacturers like ATR and Bombardier forecast an increase in the turboprop fleet in the next 20 years [1],[2].

Turboprop engines are often used for short haul flights. Their high bypass ratio makes it possible to achieve a high propulsive efficiency. As a result, the fuel consumption is reduced for turboprop engines. Turboprops operate mainly at medium speeds around 0.6-0.7 Mach [3]. At higher speeds, the propeller tips can reach supersonic speeds which creates a shock wave and results in low propulsive effciciency as the flow around the propeller blade is separated. This reduces the efficiency significantly. Furthermore, a high tip speed also creates additional noise, the so called buzz-saw noise. Therefore engine manufacturers design propeller blades such that the tips do not exceed a Mach number higher than 1 when the aircraft is flying at its operational speed.

Still, a major drawback of turboprops is the noise they produce. It is therefore of great importance to design the blades for minimal noise from the start of the design process. As the turboprop engines are operational at lower altitudes compared to conventional turbofan engines, the distance between the noise source and the observer (people) is smaller. This makes it even more crucial to reduce the turboprop noise. A comprehensive parametric turboprop noise model is needed for a quick assessment of noise in the early design phase of the turboprop. This should aim in making the turboprop less noisy and produce lower emissions while remaining fuel efficient. At the Aircraft Noise and Climate Effects (ANCE) section at the TU Delft a project in cooperation with the Netherlands Aerospace Centre (NLR) is ongoing. The aim of that project is the further development of the so called ”Virtual Community Noise Simulator” (VCNS) tool. This tool already has capabilities to predict and simulate noise of aircraft flyovers in a virtual reality environment. A great benefit is the fact that you can actually listen to what a future situation will sound like instead of just assessing noise metrics. Other benefits of this tool are that new routes/aircraft technology can be assessed in terms of noise at a much lower cost due to a reduced need for extensive noise measurements. Currently this can only be done for aircraft with a turbofan engine. Therefore NLR is looking for a way to extend the tool by adding the noise prediction capability for propeller driven aircraft. The objective of this thesis is to extend the VCNS tool, such that it is capable to predict noise emission of turboprop/propeller aircraft. In order to do this, a noise prediction model needs to be selected and implemented. The goal of this thesis is to implement a propeller noise prediction theory/model which has the future goal of being integrated in a tool like the VCNS or an aircraft design chain. Furthermore the gained knowledge about the noise a certain propeller design produces can be used in the design process.

The structure of this report is as follows. In chapter 2 the theoretical background of the research is described. Also the research framework and problem statement are discussed. Chapter 3 describes the methodology that is used for this thesis. Next, chapter 4 describes the validation of the implemented noise prediction model. Validation is performed using literature data and two NLR-tools named MAE-PROP and Rollac. In chapter 5 the noise prediction tool is applied and an auralization of a propeller fly-over is performed. Finally, this thesis is concluded with the conclusion and recommendations in chapter 6.

2

Background

This chapter contains the theorethical background for this master thesis. First, the problem statement is discussed in 2.1. In section 2.2 several aerodynamic noise sources are described. In section 2.3, some basic knowledge about propeller performance is given.

2.1. Problem Statement

Compared to the previous century the aviation industry has grown a lot. The aviation industry brings a lot of benefits with its growth. Not only does it create connectivity between people and businesses around the world, it also creates jobs. Every day more than 100000 flights take off from airports all over the world [4]. Forecasts show that the air traffic volume will double by 2034 compared to 2016 as can be seen in Figure 2.1. This is positive considering the economic benefits it creates.

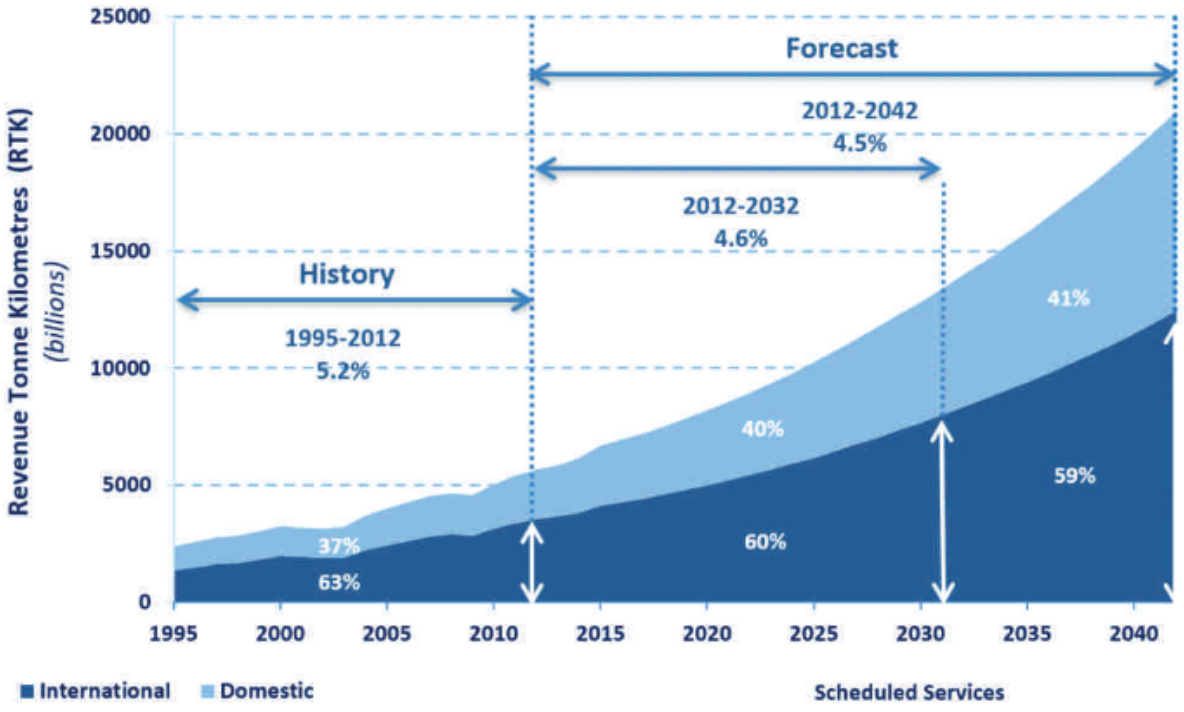

Figure 2.1: Forecast of passenger air traffic [4]

There are also some disadvantages that are associated with this growth. Not only do aircraft produce green house gas and other pollutants, they also produce noise which can be annoying, especially for residents around airports. In order to ensure that the environment remains suitable to live in, research needs to be performed on the impact noise can have on the community. This is usually done by generating noise contours in the proximity of the communities. An example of a noise tool that has the capabilities to evaluate aircraft noise around airports is the Integrated Noise Model (INM) by the Federal Aviation Administration (FAA) [5]. This model uses the Noise-Power-Distance (NPD) relation which takes into account the thrust setting to some extent, distance and other factors to calculate the noise impact. The NPD tables contain information about the sound pressure level (SPL) for different thrust settings. This data is collected from noise measurements carried out under certification conditions. The use of NPD data is beneficial when fast results are required. A limitation of such a prediction tool is that only existing aircraft configurations and engine technology can be evaluated. Furthermore, only the overall noise from an aircraft is determined and it is impossible to distinguish and evaluate the different contributors to aircraft noise.

Instead of using data from flyover measurements it is also possible to assess noise that is predicted using parametric noise source models. This is a more generic approach as it shows the effect of changing the geometry of a noise source or operating condition on the noise emission. Examples of these kind of noise prediction tools are the Aircraft Noise Prediction Program (ANOPP) developed by the National Aeronautics and Space Administration (NASA) and the Parametric Aircraft Noise Analysis Module (PANAM) developed by the German Aerospace Centre (DLR). Both of these tools are semi-empirical models and include source noise models of airframe noise, engine noise, jet noise and fan noise.
The Netherlands Aerospace Centre (NLR) has developed a tool called the Virtual Community Noise Simulator (VCNS) [6]. The VCNS is capable of simulating noise in virtual environments either utilizing recordings of a flyover or auralization. Auralization is the process of transforming a source noise prediction into an audible result. Auralization is interesting when new flight procedures or aircraft designs need to be evaluated. It can also be used for psycho-acoustic analysis as it allows people to judge noise by including visual and audible aspects as can be seen in Figure 2.2. The simulator shows a virtual reality environment through a Head Mounted Display providing a 360 degrees view and presents the sound to the listener through a headphone. The sound that is then observed is dependent on the head direction which gives a more realistic perception of the actual sound.

Figure 2.2: VCNS Helmet Mounted Display and headphones[1]

A benefit of using auralization is that the sound presented to the listener does not depend on recordings and can thus be altered to new aircraft types or components and to new flight procedures or weather conditions. Also the noise characteristics of new aircraft designs can be analysed by the aircraft designer using the VCNS [7]. Currently, the VCNS is able to auralize the noise of turbofan aircraft [6]. The noise

[1]Source of image: $https://www.nlr.org/capabilities/noise-simulator/$

sources that are included in the noise prediction process of the VCNS can be seen in Figure 2.3. This figure indicates that propeller noise is not yet part of the VCNS.

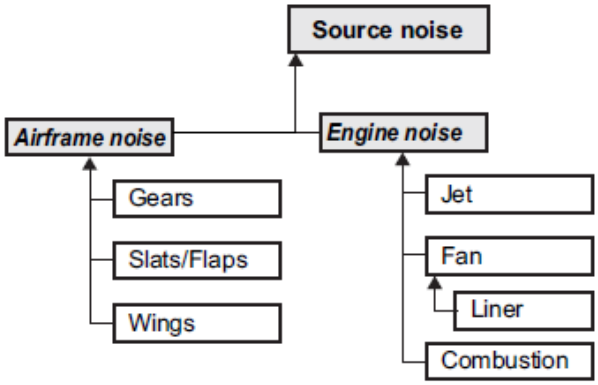

Figure 2.3: Source noise model available in VCNS [8]

The interest in propeller noise is increasing with companies like ATR and Bombardier forecasting an increase in aircraft equipped with turboprop engines in the next 20 years [1],[2]. Turboprop engines have a higher propulsive efficiency at lower speeds than the conventional turbofan engine as can be seen in Figure 2.4. This is one of the reasons that aircraft equipped with turboprop engines are mainly used for short haul flights. With an increase in domestic flights being forecasted, the turboprop engine is an engine that should be taken into consideration. The higher efficiency of a turboprop compared to that of a turbofan is due to the fact that they induce smaller velocity increments to a larger air mass flow. The propulsive efficiency can be computed from

$$\eta_{prop} = \frac{2}{1 + \frac{V_j}{V_\infty}}, \tag{2.1}$$

where V_j is the jet velocity and V_∞ is the free-stream velocity. The propulsive efficiency represents the ratio of the power output to the rate of energy input. Equation 2.1 indicates that the propulsive efficiency increases as the jet velocity gets closer to the free-stream velocity. A small acceleration of a large amount of air is therefore more beneficial than a large acceleration of a small amount of air. Turboprop engine are capable of accelerating a large amount of air at low air speed [9]. This is beneficial during operations like take-off and climb and hence results in better take-off and climb capabilities. It allows the aircraft to spend less time during this phase of the flight and can help reducing the sound exposure level for the area around the airfield. The sound exposure level is a measure of noise and is dependent on the duration of the emitted noise. A shorter duration results in a lower sound exposure level. However, a major difference between a turboprop and a turbofan engine is the missing piece of nacelle around the rotating blades. Therefore the noise emitted is significant and can not be neglected. Furthermore, aircraft equipped with turboprop engines operate at a lower altitude. The distance between the source and observer is smaller during cruise compared to aircraft equipped with turbofan. A smaller distance can result in higher noise levels being obtained. Since a source noise model for propellers is still missing in the VCNS, the focus of this master thesis will be on the development and implementation of a source noise model for propellers.

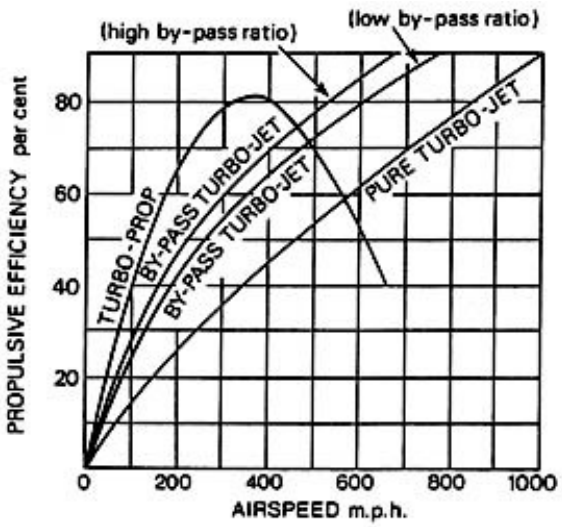

Figure 2.4: Propulsive efficiency for various gas turbine engine configuration with on the x-axis the airspeed in miles per hour and on the y-axis the propulsive efficiency [2]

2.1.1. Research Framework

The research framework is depicted in Figure 2.5. First, the theory about propeller aerodynamics, propeller noise sources and propeller noise prediction is gathered. Then the chosen theory is implemented and validated with publicly available data as well as with another tool with the same capabilities. The results are then compared and a discussion is given. Finally, a conclusion is drawn and recommendations are given.

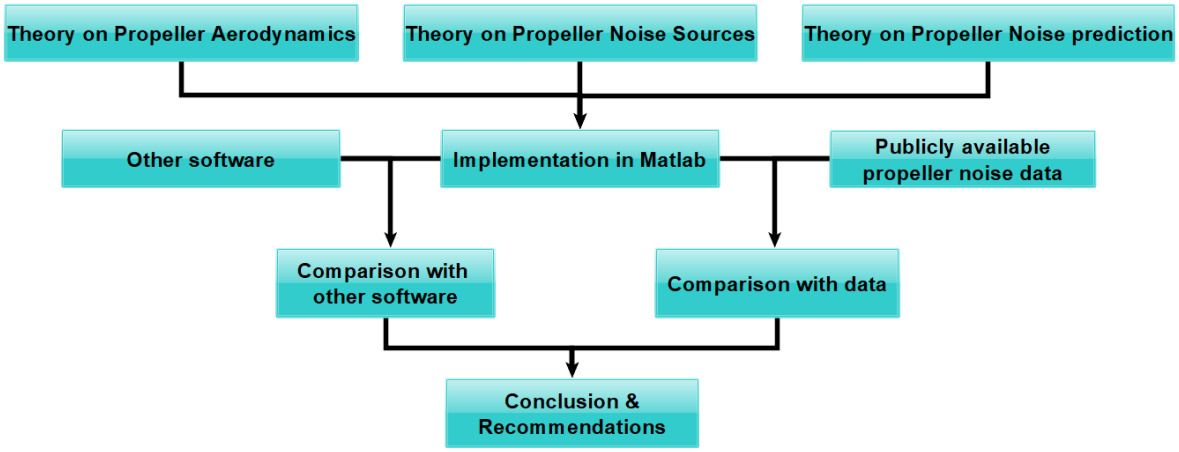

Figure 2.5: Research framework of the thesis

[2]Source of image: http://web.mit.edu/16.unified/www/FALL/thermodynamics/notes/node82.html

2.2. Noise Sources

Aircraft noise prediction is dependent on two disciplines in particular: aerodynamics and acoustics. The two disciplines together form the field of aeroacoustics. Aerodynamic noise is generated as a result of unsteady motion of a fluid or solid body in a medium. As already stated in chapter 1, use can be made of NPD data for estimating aircraft noise. However, noise produced by an aircraft is often also estimated with the method of components [10]. This means that each noise-generating component of an aircraft is considered individually and added together to get an overall view of the noise generated by the aircraft. An advantage of this is that the separate noise prediction source models can be improved individually if the results generated are not in good agreement with measurements. An overview of the noise sources of an aircraft is given in Figure 2.6. It can be seen that the noise sources in a conventional aircraft can be divided into airframe noise and engine noise. Furthermore, these noise sources are dependent on atmospheric conditions and propagation effects. Landing gear noise, flap noise, slat noise, stabiliser noise and wing trailing edge noise are examples of airframe noise. However, the focus for this thesis is on the noise generated by the turboprop engine. The turboprop engine is a turbine engine which drives a propeller as can be seen in Figure 2.7. A turboprop consists of many different parts that generate noise. The noise generated by the turboprop engine can be categorised in engine core noise, jet noise and propeller noise [10].

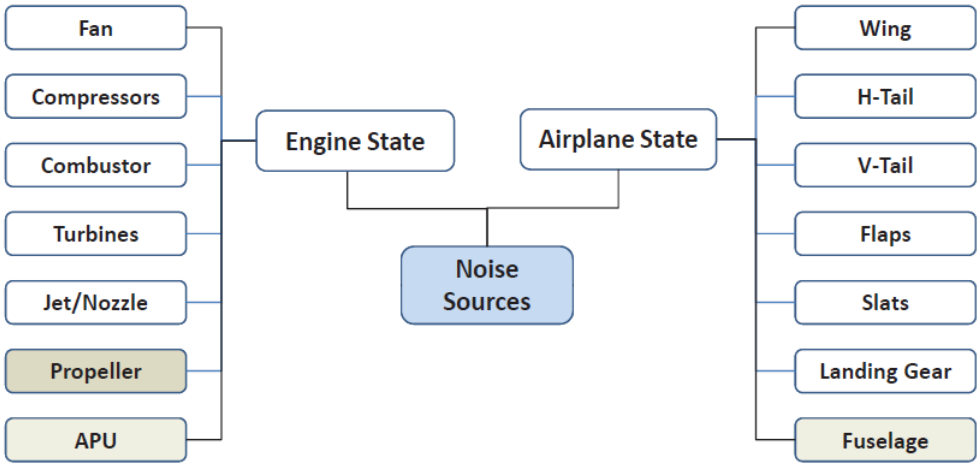

Figure 2.6: Breakdown of several noise-sources in a conventional aircraft [11]

Even though the focus of the thesis is on propeller noise, it is important to get a complete overview on the other noise sources that are present in a turboprop engine. In the next sections the engine core noise and the jet noise are discussed briefly. A brief description of the engine core noise is given in 2.2.1. The jet noise is discussed in 2.2.2. The focus will be mainly on the propeller noise since a propeller noise model is what is still missing in the VCNS noise prediction/simulation tool. Actually, the noise generated by the propeller blades can be assumed to be the dominant source of noise in propeller driven engines [12]. More about the propeller noise can be found in section 2.2.3.

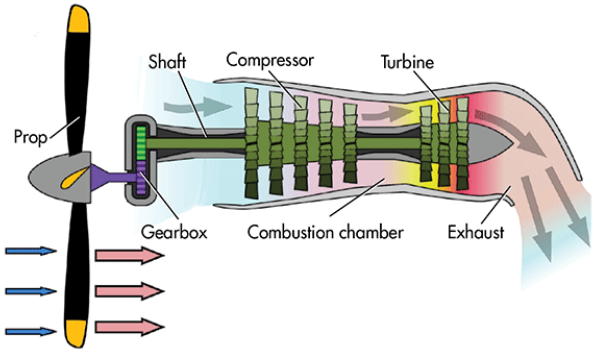

Figure 2.7: Schematic of a turboprop engine showing the different parts of the engine[3]

2.2.1. Engine Core Noise

The engine core noise consists of the turbomachinery and combustion noise. A brief description of each noise source is given in this section.

Turbomachinery Noise

Compressors and turbines consist of rotating and stationary blades, i.e. rotors and vanes, which are placed close to each other. Due to the rotor-stator interaction tonal and broadband noise is generated. The noise generating process of turbomachinery starts with internal disturbances, e.g. blade wakes or vortices, or inflow disturbances, e.g. turbulence. These disturbances result in unsteady blade surface pressures and as a result noise is generated. Discrete tones are generated due to the pressure fluctuations from blade wake interaction with the vanes. This type of noise is mainly important during approach [13]. It is a complex noise source to model due to interaction between the different stages, turbulence and unsteady flow interaction between rotor blades, vanes and supersonic effects at blade tips.

Combustion Noise

The combustion noise consists of mainly broadband noise. As the noise from other noise sources such as fan and jet noise is being reduced more and more, this noise source is becoming more dominant. The noise of a combustor is caused by the heating of the fuel which is done in the combustion chamber [14]. A distinction is made between direct and indirect noise caused by the combustion. Gas expansion in the combustion chamber, which is caused by the fuel combustion, interacts with the flow surrounding it and is called a direct noise. Indirect combustion noise is caused by the hot products that pass through the turbine and exhaust nozzle. The convection that occurs causes the entropy of the flow to change and as a result indirect noise is obtained [15]. At low thrust setting the combustion noise becomes more prominent.

2.2.2. Jet Noise

Jet noise is one of the biggest sources of noise for aircraft. In a turboprop engine the contribution of the jet noise is small as the thrust is mainly generated by the propellers and is only generated for a small amount by the jet. The noise is caused by turbulent mixing and shock noise.

Turbulent mixing

Turbulent mixing is the result of the interaction of two flow regimes with different velocities, like the high velocity jets from the core with the bypass flow from the nozzle or with the ambient air. At the shear layer between the two flow regimes, turbulence is generated due to the mixing of the two flows. Turbulence induces pressure fluctuations and hence jet noise is emitted. This noise is especially important during take-off and is distributed behind the engine [16].

[3]Source of image: url:http://www.machinedesign.com/motorsdrives/what-s-difference-between-turbine-engines

Shock noise
In the presence of supersonic jet speeds in the exhaust, shock noise is generated next to turbulent mixing noise. Shock noise is best known to occur at supersonic aircraft as these types of aircraft have high jet Mach numbers.

2.2.3. Propeller Noise Sources
Propellers come in different shapes and sizes. Even though they differ in geometry, the principle of noise generated by all propellers is the same. A distinction can be made between several types of noise. When considering propellers we distinguish two types of noise [17]:

- Harmonic or tonal noise
- Broadband noise

Harmonic Noise
Due to the rotation of the propeller periodic noise is generated. The noise components that occur periodically are the thickness noise and the (un)steady-loading noise. Thickness noise can be described as the noise that is caused due to the displacement of air flow of molecules by the volume of the blades. This displacement causes the pressure field to fluctuate, which results in the generation of noise. This type of noise becomes more evident with increasing rotational velocity. The thickness noise can be modelled by using a monopole source. The displacement of air results in fluctuations in mass and this leads to a monopole behaviour. A monopole is an elementary source, representing a harmonic pulsating sphere [18]. Since the resulting fluctuations are not the same at different locations on the blade, the thickness noise is described using a disc of monopoles.
Steady-loading noise is determined by the pressure field of the blades which generates lift and drag (or the thrust and torque components). Since the blades move in a medium (air), the moving pressure field of the blades induce pressure fluctuations. Hence loading noise is generated. This noise is significant at low and moderate speeds [13]. The loading noise can be described by using dipoles which also are elementary sources. The dipole source reflects the radiation profile of fluctuating forces [8]. A dipole consists of two monopole sources of equal strength but opposite phase positioned at a small distance from each other. This distance is small compared to the wavelength. In Figure 2.8 and 2.9 the monopole and dipole source are depicted. The arrows indicate the radiation direction of such a source and the dashed lines indicate the amplitude of the source in the different directions.

Figure 2.8: Directivity pattern of a monopole source

Figure 2.9: Directivity pattern of a dipole source

Next to steady sources, unsteady sources exist. Unsteady-loading noise is caused by inflow distortions that occur constantly. This is for example the case when a propeller has a non-axial inflow, i.e. angle

of attack. Due to this constant inflow distortion, changes in blade loading repeat after each revolution. In Figure 2.10 a propeller with non-axial inflow is depicted. During one revolution of the blade, the blade encounters a higher or a lower resulting velocity term as a result of the added inflow velocity component V_z. This combination of the component of the forward speed of the plane with the rotational component of the propeller produces a periodic variation of the angle of attack obtained at the propeller blade section while it is rotating [9]. Depending on the location of the blade during the rotation, the unsteady loading source can either be subtracted from or added to the steady loading noise [17]. As a result asymmetric loading is obtained. The loading for steady loading is symmetric. This is the case when the inflow is in the axial direction.

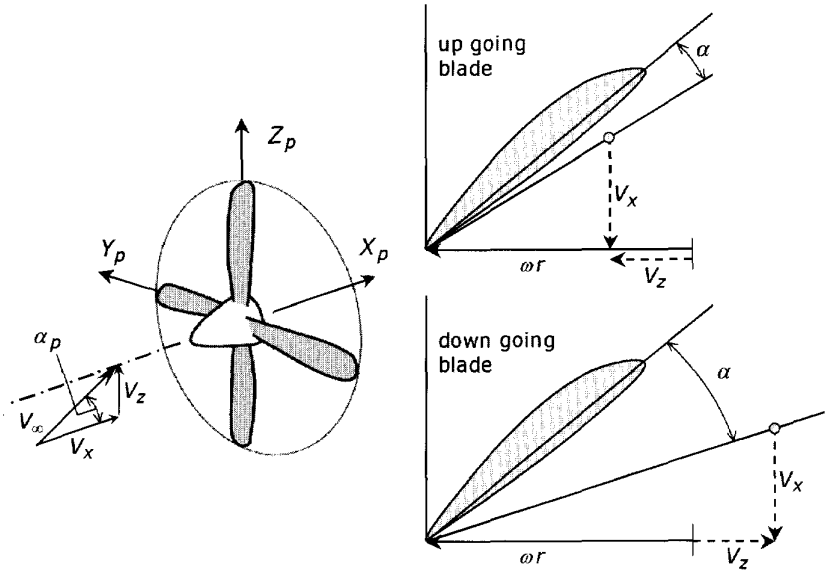

Figure 2.10: Propeller at an angle of attack [9]

The above mentioned sources are types of harmonic noise sources. Harmonic noise appears at a constant rate, periodically. Assuming that the propeller is an ideal one, the harmonic noise component repeats itself at the Blade Passage Frequency (BPF) [18]

$$BPF = B\frac{RPM}{60}, \tag{2.2}$$

where *B* is the number of blades of the propeller and *RPM* is the number of revolutions per minute. Since the signal being generated by the propeller is not a pure sinusoid, multiple harmonics exist which occur at *nBPF* where *n* is an integer larger than zero and *BPF* is the blade passage frequency. The first harmonic is known as the fundamental frequency. Figure 2.12 and 2.11 show an example of what the spectrum and signature of propeller harmonic noise looks like. The spectrum shows peaks at the *BPF* and multiples of the *BPF* while the time domain depicts a signature which repeats after a period of $\frac{1}{BPF}$. The maximum amplitude in the time domain appears constantly after each period. The propeller signal can be approximated by a sum of sinusoids at the harmonic frequencies of the signal. The frequencies of the harmonics can be found by applying a Fourier transform which transforms the signal from the time domain to the frequency domain. Since the signal has a finite time interval a Discrete Fourier transform is used. Figure 2.11 shows an example of the time signal. In general, the Discrete Fourier transform is implemented as the Fast Fourier transform. The result of the Fast Fourier transform is a spectrum of the signal containing the amplitudes at the harmonic frequencies. The Power Spectral Density (Pa^2/Hz) can now be calculated which is a measure of the signal's power versus the frequency. For a chunk of data this can be done using the following expression

$$P(f) = \frac{|X(f)|^2(\Delta t)^2}{T}, \tag{2.3}$$

where $P(f)$ is the power spectral density of the signal, $X(f)$ is the Discrete Fourier transform of the propeller time signal obtained in Matlab, Δt is the time interval and T is the integration time. The Sound Pressure level for each chunk of data can now be calculated for bands with a width Δf using the following

$$SPL(dB) = 10\,log_{10}\left(\frac{P(f)\Delta f}{p_{e0}^2}\right), \tag{2.4}$$

where p_{e0} is the reference effective pressure and is also known as the threshold of hearing at a frequency of 1000 Hz and has a value of $2 \cdot 10^{-5}$ Pa for air.

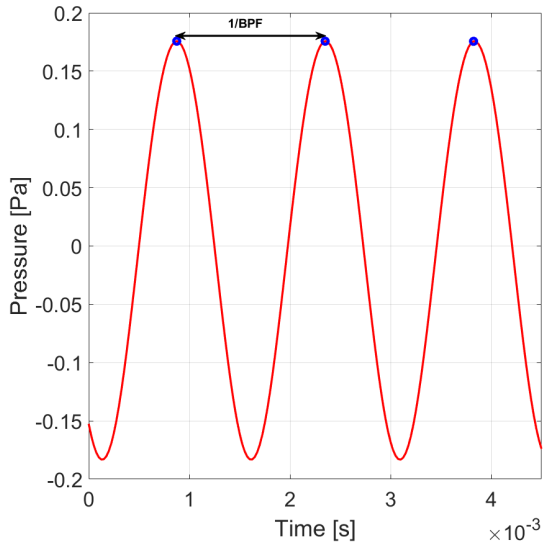

Figure 2.11: Example of a signature of tonal noise in the time domain, $BPF = 675Hz$, Δf=0.1 Hz and p_{e0}=$2 \cdot 10^{-5}$ Pa

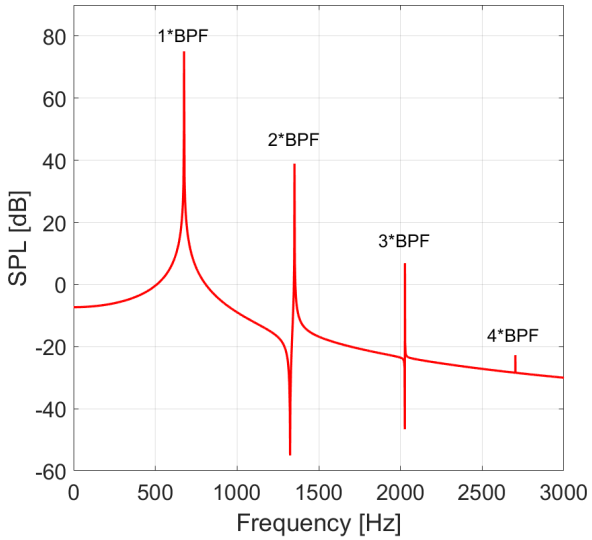

Figure 2.12: SPL versus frequency plot with the blade passage frequency and its harmonics indicated, $BPF = 675Hz$,Δf=0.1 Hz and p_{e0}=$2 \cdot 10^{-5}$ Pa

Broadband Noise
Broadband noise is typically induced by turbulence. The sources that cause broadband noise are random in nature and therefore unsteady. Broadband noise is emitted over a wide range of frequencies as can be seen by the spectrum levels of a typical broadband noise signal in Figure 2.14. The time series from what the spectrum is obtained can be seen in Figure 2.13. When considering a propeller, the contribution of broadband noise is often much smaller compared to the tonal noise components.

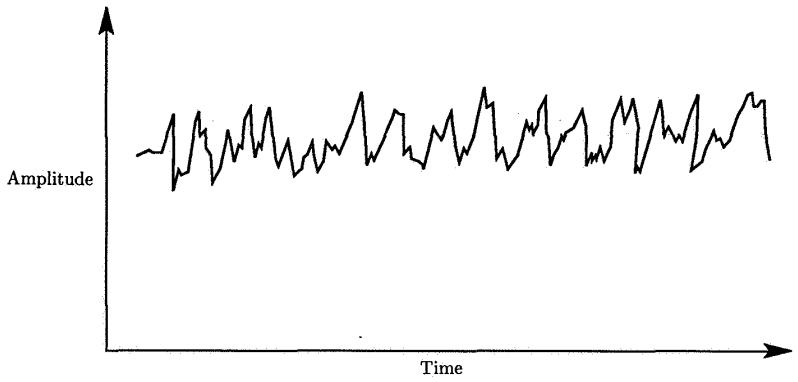

Figure 2.13: Example of broadband noise time series [13]

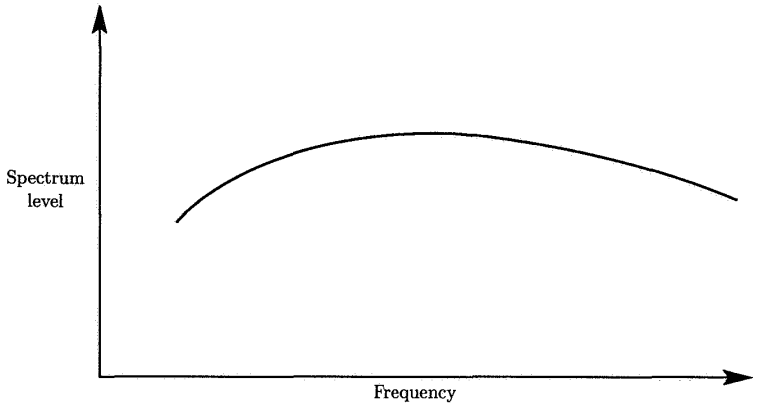

Figure 2.14: Spectrum of broadband noise [13]

Broadband noise is induced by an unsteady pressure field around the blades. This unsteady pressure field occurs when for instance vortices are being shed from the tips and trailling edges of the propeller blades [19]. Note that if the vortex shedding occurs periodically, which is the case with for example for the periodic vortex detachment i.e. Karman vortex sheet, then the vortex shedding will also have a tonal contribution.
Another contributor to broadband noise is the turbulence of the airflow. The interaction of the blades with the turbulent airflow causes an unsteady pressure field. As a result broadband noise arises [20]. If the boundary layer of the blade is turbulent, the generated noise is concentrated on the trailing edge of the blade. An example of a situation in which a propeller has a turbulent inflow is when a propeller/-turboprop driven aircraft is stationary. Stationary propellers suck their own turbulent flow due to the pressure difference in front and after the propeller. Recirculation is present and the noise is significantly increased. This can be counteracted by simply moving the aircraft forward. The recirculation is then disrupted and as a result a less turbulent inflow is present. When a turbulent inflow is absent, turbulence can still be produced in the boundary layer of an airfoil. In the case of the turbulence not being close to an edge, the turbulence generates noise emissions that are typically represented by so-called quadrupoles [13]. In Figure 2.15 the quadrupole source is depicted, consisting of two dipole sources of equal strength but opposite phase. The quadrupole source is in general a weak noise generating

mechanism compared to the dipole source.

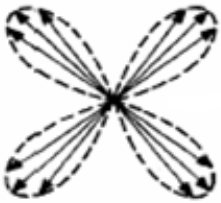

Figure 2.15: Quadrupole source

In practice broadband noise is often predicted with semi-empirical methods. Schlinker and Amiet show an example of estimating the broadband noise component which is based on fitting of airfoil data and approximations regarding the boundary layer [21]. This is not shown here in detail as the contribution of broadband noise is small. For this thesis the focus is not put on broadband noise. Nevertheless, this type of noise should not be omitted when auralization is performed as it makes the noise of a propeller more realistic.

Non-linear sources

The quadrupole source becomes more prominent when the non-linear effects arise. This is when sonic or supersonic speeds are achieved for example. The noise of the shock waves that occur can then be represented by the quadrupole source. Blackburn [22] performed an analysis on the importance of the quadrupole source term. He states that the non-linear effects are significant at high Mach numbers when shocks are formed on the blade. The results of his analysis are depicted in Figure 2.16. In this figure the added noise by the quadrupole term with respect to the relative Mach number can be seen. The results are obtained from a two dimensional aerodynamic model. It can be seen that between the indicated critical Mach number and a Mach number of 1, the added noise due to non-linear effects is the most.

Modern turboprop blades are often swept and consist of thin airfoil sections which reduces the nonlinear effect (the critical Mach number is increased) on the blade [23]. This doesn't mean that the importance of the quadrupole source term can be neglected as it is important when an accurate prediction needs to be obtained at high Mach numbers (near sonic conditions) [22]. This statement is also supported by Hanson and Fink in [24].

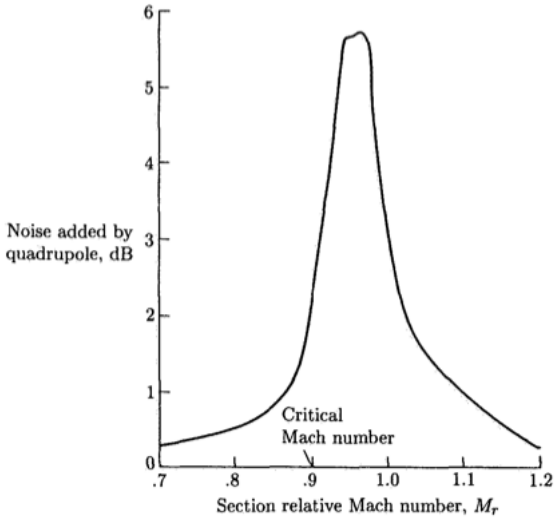

Figure 2.16: Increase in noise by the quadrupole term obtained from data [22]

2.3. Propeller Performance

The contribution to the total thrust generated by a turboprop engine consists of a small portion by the jet and a big portion is generated by the propeller blades. Therefore it is important to estimate the propeller performance. In this section, a brief description about the propeller performance and propeller performance coefficients is given. Propeller performance coefficients are coefficients that are used to indicate the performance of a propeller. These can be used to get a better idea about how thrust is generated and what elements have a role in generating this force.

Propellers are made up of airfoil sections and are designed to produce aerodynamic forces. In addition to aircraft wings, propellers do not only translate but also rotate. Propellers are used to generate thrust to push an airplane through the air. Propeller propulsion may reduce fuel consumption significantly compared to conventional turbofan engines. This depends on the speed the aircraft is designed to fly at. The relative wind or the effective velocity that the propeller sees is the vector sum of the freestream velocity V_∞ and the rotational velocity Ω. In Figure 2.17 a schematic of a velocity diagram of a propeller blade section is depicted. Here the freestream velocity is referred to as W_a, the rotational velocity is referred to as W_t and the effective velocity is referred to as W.

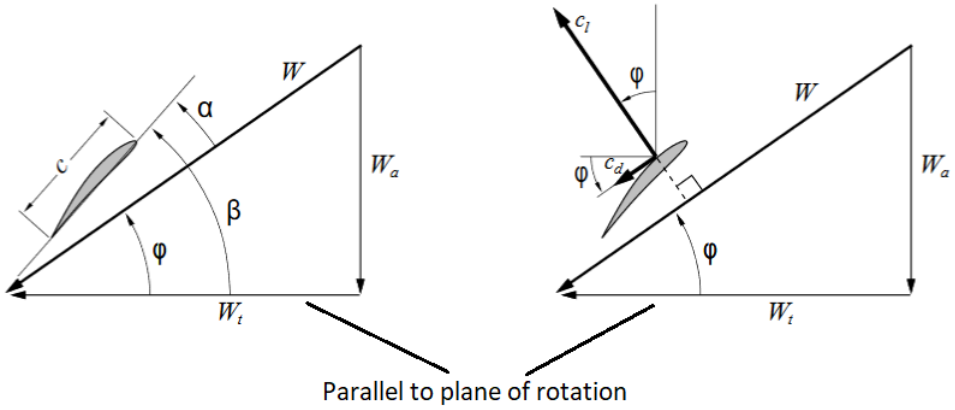

Figure 2.17: Velocity diagram of a propeller blade section

The angle of attack α of a propeller blade section depends on the local velocities and the local pitch angle. The local pitch angle is indicated with the symbol β which is dependent on the blade design. Some propellers have a variable-pitch meaning that the pitch can be changed such that it is suitable for a certain operational condition. The local inflow angle ϕ can be computed using the following expression

$$\phi = \tan^{-1}\left(\frac{Wa}{Wt}\right) \tag{2.5}$$

The local angle of attack α can be calculated using equation 2.6.

$$\alpha = \beta - \phi \tag{2.6}$$

The axial velocity component, i.e. the freestream velocity, is the same along the blade radius. The tangential velocity component however increases when getting closer to the tip. Therefore the highest velocity is obtained at the propeller tip. The vector sum of the tangential velocity at the tip and the freestream velocity divided by the local speed of sound is known as the helical tip Mach number. This is a parameter that is often used in propeller performance.
When considering propeller performance, the following dimensionless coefficients are used.

$$C_T = \frac{T}{\rho n^2 D^4} \tag{2.7}$$

$$C_Q = \frac{Q}{\rho n^2 D^5} \tag{2.8}$$

$$C_P = \frac{P}{\rho n^3 D^5} \tag{2.9}$$

$$J = \frac{V_\infty}{nD} \tag{2.10}$$

$$\eta = J\frac{C_T}{C_p} \tag{2.11}$$

C_T, C_Q, C_P, J and η are the thrust coefficient, torque coefficient, power coefficient, advance ratio and efficiency respectively. Here T is the total thrust, Q is the total torque, P is the total power, D is the diameter of the propeller, n is the number of revolutions per second. The thrust of one blade element be calculated using the following expression

$$dT = dL\cos(\phi_i) - dD\sin(\phi_i) \tag{2.12}$$

where ϕ_i is the local inflow angle, dL is the lift of one blade section and can be calulated with the following expression $\frac{1}{2}\rho c V_{local}^2 C_l dr$. The drag of a small radial element dD can be calculated with $\frac{1}{2}\rho c V_{local}^2 C_d dr$. Here c is the local chord and dr is the size of the blade element in radial direction. The total torque can be calculated using the following

$$dQ = r(dL\sin(\phi_i) + dD\cos(\phi_i)) \tag{2.13}$$

where r is the local radial distance from the root to the blade element. The total thrust and torque can be calculated by summing the thrust and torque obtained from the individual blade elements and multiplying with the number of blades of the propeller.

The power that is needed to drive the propeller can also be calculated using torque coefficient

$$P = 2\pi C_Q \rho n^3 D^5 \tag{2.14}$$

The advance ratio J gives an indication for the loading of the propeller and can be calculated with equation 2.10. In Figure 2.18 a propeller with a low advance ratio (high loading) and propeller with a high advance ratio (low loading) can be seen. The loading of a propeller depends on the lift and drag distribution along the propeller blade radius. The loading is often higher when a larger angle of attack is obtained.

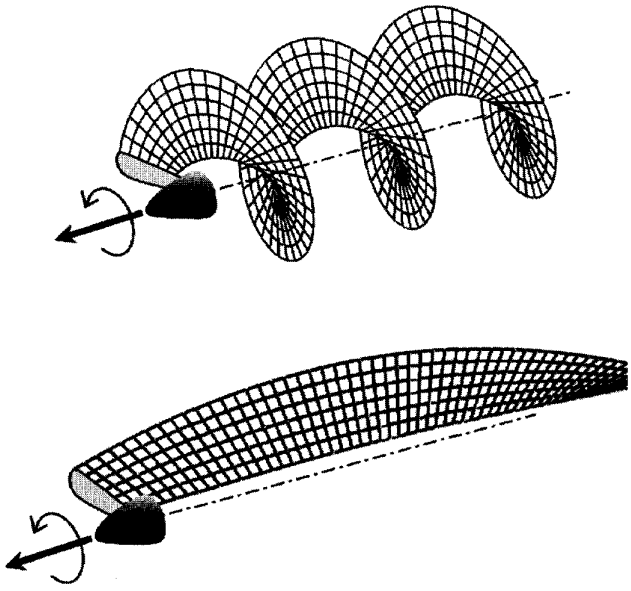

Figure 2.18: Vortical wake of a propeller with high loading (upper) and light loading (lower) [9]

3

Methodology

In this chapter the methodology is discussed. In section 3.1 an overview is given of the methodology used in this thesis. This is done using a flow diagram which shows a more general overview of the different steps involved in the computations that are performed. The aerodynamics of the propeller are an important aspect of this research as they are required to determine the performance of the propeller and are an input for the modelling of propeller noise. In section 3.2 the calculation of the propeller performance is described. This calculation is performed with two external tools, XFoil and XRotor. First a description of these tools is given. A more detailed flow diagram of the calculations performed by the propeller performance tools and how these are implemented in Matlab is given in section 3.2.1. Furthermore, the methodology regarding the implemented noise prediction theory is described in section 3.3. This is the Helicoidal Surface Theory developed by Hanson [25]. The far-field radiation equations from the Helicoidal Surface Theory are also described in this section. Section 3.3.1 presents the flow diagram displaying the chain of computations performed in order to obtain a noise signal and a description is given of its implementation in Matlab. The combination of XFoil, XRotor and the Helicoidal Surface Theory is implemented together and is referred to as the HeliX-tool in the remainder of this report.

3.1. Methodology Overview

The computational methods from the different disciplines involved in the calculation of propeller noise are all implemented in Matlab. In Figure 3.1 a general overview of the process is depicted. The first step is the definition of the propeller geometry and operational conditions as the computations that are performed depend on them. Then the variables are initialised and are ready to be used in the computation of the propeller performance. When the computation of the propeller performance is completed and the solution has converged, the results are used for the computation of the noise. At last these results are plotted and the tool stops running. A more detailed flowchart is shown in the following sections. These describe the calculation of the propeller performance and the final noise signal and show how these are dependent on each other.

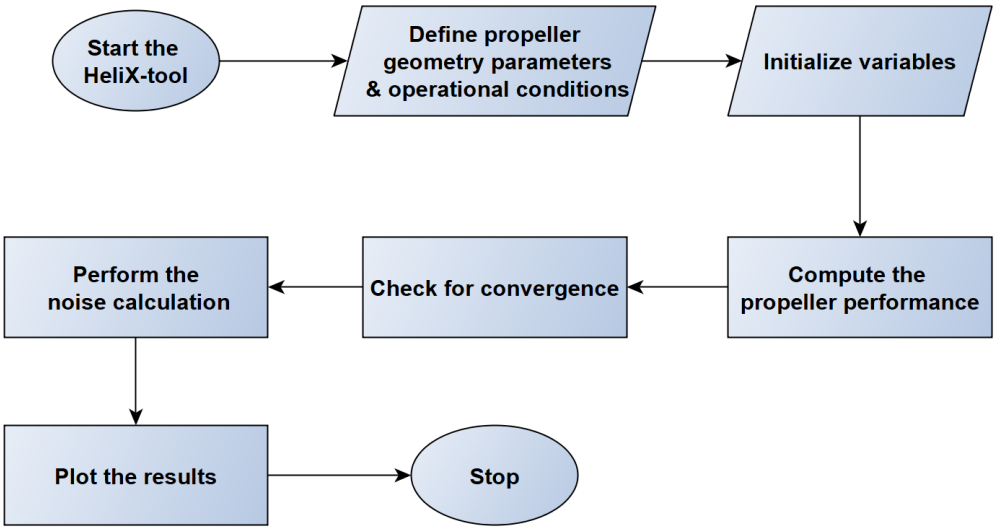

Figure 3.1: Flowchart showing the general overview of the main processes involved in the HeliX-tool

3.2. Propeller Performance Prediction Method

As is adressed in the previous sections, the propeller aerodynamic properties are required in order to perform noise calculations. When choosing a propeller aerodynamics tool, three elements are important: flexibility, run time and accuracy. Since the objective of this thesis is to develop a propeller noise model for multidisciplinary design purposes, it is important that the run time is kept low while still being flexible in changing design parameters of a propeller. One of the most often used propeller aerodynamics tool at the Flight Performance and Propulsion department of TU Delft is XRotor [26]. In XRotor the design and analysis of propellers can be performed. XRotor uses a propeller lifting line theory. This lifting line theory computes the circulation, the induced velocities, the local angles of attack, the lift and drag coefficients in an iterative manner until convergence is achieved. After convergence is achieved, the propeller performance coefficients are given as output together with the loading of the propeller blades.

Three methods exist within XRotor for the calculation of induced velocities and induced losses; the graded-momentum formulation, the potential formulation and the vortex formulation. The graded momentum formulation is a classical theory that uses the Betz-Prandtl tip loss fudge factor. This loss factor is applicable to advance ratios up to $\frac{1}{2}\pi$. Therefore this formulation should not be used for higher advance ratios. A benefit of using the graded momentum formulation is the computational efficiency it offers. A disadvantage however is the limitations it brings in the range of advance ratios for which the propeller performance parameters can be computed.
A more sophisticated approach is the potential formulation. This method solves the helically-symmetric potential flow about a rigid helicoidal wake. It is valid for all blade numbers and can handle a lot of radial load distributions. This method is promising, but comes with an increased computational run time when compared to the graded momentum formulation. However, the potential formulation allows

rotor hubs and nacelle installation to be included. The graded momentum formulation cannot deal with this properly due to the Betz-Prandtl fudge factor for which a low advance ratio is assumed.
At last the vortex formulation is also included in XRotor which makes use of a discrete vortex wake to calculate the induced velocity. The discrete vortices are located on the rigid helicoidal wake surface and trail from the lifting line into the far-field downstream. This approach allows to also analyse propellers with raked tips and swept blades. The computational run time is increased compared to the other two methods but it can be used for a larger variety of propeller geometries.

In a study performed in [27] XRotor is compared to two other propeller analysis tools: JavaProp [28] and Adkins & Liebeck scheme [29]. In this validation study, a propeller of which the performance data is known from an experiment is used. In each tool the propeller is imported and an analysis is performed. The deviations between the computed performance and the performance obtained from the experiment are then compared with each other. From this study it is found that XRotor has the best overall performance. XRotor is therefore chosen to work with for this thesis when computing propeller performance data. For the calculation of the induced velocities the potential formulation is used in the remainder of this thesis. This formulation is chosen as the propeller (a description of this propeller is given in chapter 4) that is used in the analysis has a straight blade and thus does not have sweep. It is therefore not needed to use the vortex formulation as this will slightly increase the computational run time.

The required inputs for XRotor can be seen below:

- α_{0L}, the zero-lift angle of attack
- $\frac{d(Cl)}{d(alpha)}$, the lift slope
- $(\frac{d(Cl)}{d(alpha)})_{stall}$, the lift slope at stall
- $C_{l_{max}}$, the maximum lift coefficient
- $C_{l_{min}}$, the minimum lift coefficient
- ΔCl increment to stall
- C_{d0}, the minimum drag coefficient
- C_{l0}, C_l at minimum C_d
- $\frac{d(Cd)}{d(C_l^2)}$, quadratic coefficient
- Re_{ref}, reference Reynolds number
- f, Reynolds number scaling exponent
- C_m, the pitching moment coefficient
- M_{crit}, the critical Mach number
- Geometry of the propeller

The inputs for XRotor and the aerodynamic properties are determined with XFoil. XFoil is a tool that is used to analyze or design airfoils. It is developed by Mark Drela [30] who is also one of the developers of XRotor. The aerodynamic properties need to be determined for every location that is distributed radially over the propeller blade. More about how this is implemented in Matlab and what settings are used can be found in section 3.2.1.

3.2.1. Implementation of the Propeller Aerodynamics tool

In this section the implementation of XRotor and XFoil are given. Also the settings that are used to generate results for this thesis are discussed.

In order to run XRotor, several input parameters are needed as is shown in the previous section. For a great part these input parameters are determined from the 2D aerodynamic data generated by XFoil. The only input parameters that are known before running XFoil, are the geometry of the propeller, the Reynolds number scaling exponent f and the critical Mach number. The geometry of the propeller is obviously known and is described in the XRotor inputfile. The geometry of the propeller is described by defining the chord-to radius ratio $\frac{c_{local}}{R}$, the local blade pitch angle β for every blade section that is used in the computation. The location of each blade section is referred to with $\frac{r}{R}$ which is the radial position as a fraction of the radius. Finally the radius and the total number of blades should be given as well. In this research, the number of blade sections for the propeller geometry description is set equal to the number of airfoil sections used to compute the aerodynamic properties of the blade.

The Reynolds number scaling exponent f is a parameter that is used in XRotor to scale the drag coefficient as can be seen in the following equation

$$C_d = (C_{d0} + \frac{dC_d}{dC_l^2}(C_{l0} - C_l)^2)(\frac{Re}{Re_{ref}})^f \tag{3.1}$$

where Re is the local Reynolds number and Re_{ref} is the reference Reynold number, i.e. the Reynolds number at which XFoil is run for a blade section. For this work it is chosen to run XFoil and XRotor for one operational condition, meaning that the local reference Reynolds number and the local Reynolds number are equal. Therefore it is chosen to set the Reynolds scaling exponent of the propeller blade section to zero. When it is chosen to run XRotor for multiple operating conditions while running XFoil for just one reference operating condition, the scaling exponent can be set according to the following

- $f = -0.1$ to -0.2 for high Reynolds number, $Re > 2 \cdot 6$
- $f = -0.5$ to -1.5 for low-Reynolds number, Re from $2 \cdot 10^5$ to $8 \cdot 10^5$
- $f = -0.3$ to -0.5 for even lower Reynolds number, $Re < 1 \cdot 10^5$

A definition of the Reynolds number is given by the following equation

$$Re = \frac{\rho V_{local} c_{local}}{\mu} \tag{3.2}$$

where μ is the dynamic viscosity of the flow and c is the local chord length of the blade section.

The critical Mach number is the Mach number of the flow in front of the blade section for which the flow over the blade section reaches a Mach number of 1 locally. The critical Mach number can be estimated using the relation between the pressure coefficient and Mach number. This relation is known as the Prandtl-Glauert relation [31]

$$C_{pr} = \frac{2}{\gamma M_\infty^2}\left[\left(\frac{1 + [(\gamma - 1)/2]M_\infty^2}{1 + \frac{\gamma - 1}{2}}\right)^{\frac{\gamma}{\gamma - 1}} - 1\right] \tag{3.3}$$

where C_{pr} is the pressure coefficient, γ is the specific heat ratio and M_∞ is the free-stream Mach number. Equation 3.3 is used to generate the so-called airfoil independent curve which can be seen in Figure 3.2. In order to determine the critical Mach number an additional relation is used. With equation 3.4 the pressure coefficient is also computed with the following

$$C_{pr} = \frac{C_{pr,0}}{\sqrt{1 - M_\infty^2}}, \tag{3.4}$$

where $C_{pr,0}$ is the minimum incompressible pressure coefficient at the suction side and C_{pr} is the compressible pressure coefficient. Note that the minimum incompressible pressure coefficient is corrected for compressibility effects. The same correction is also applied to correct the lift and drag coefficients for compressibility effects in XRotor.
The pressure distribution of a blade section depends on the local angle of attack. The local angle of attack is not known before running XRotor as it is one of the outputs obtained from XRotor. Furthermore, the airfoil thickness also affects the pressure distribution. For the same angle of attack and Reynolds number, a thicker airfoil has a larger minimum pressure coefficient at the suction side of the airfoil than a thin airfoil. The expansion on the top surface of a thin airfoil is less severe than that of a thick airfoil. Thus resulting in a minimum pressure coefficient with a smaller magnitude for the thin airfoil compared to that of a thick airfoil. As a result the airfoil dependent curve that is generated using equation 3.4 shown in Figure 3.2 shifts to the left for thicker airfoils and to the right for thinner airfoils. The intersection of the two curves shown in Figure 3.2 determines the final critical Mach number. Thus the critical Mach number depends on several parameters like the local angle of attack, Reynolds number and airfoil thickness. As not all the parameters are known beforehand it is decided

to make an assumption for this version of the HeliX-tool regarding the critical Mach number. In the work performed in this thesis the M_{cr} is assumed to be 0.78 for all blade sections of the propeller of interest unless stated otherwise.

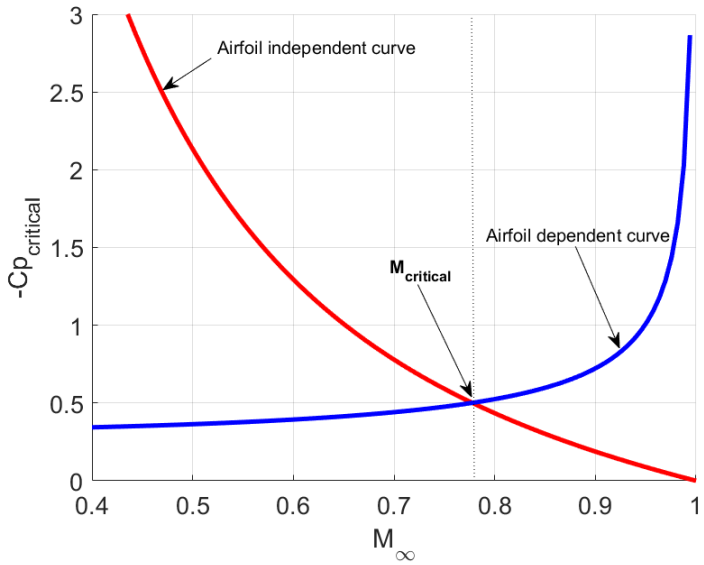

Figure 3.2: Pressure coefficient plotted against the free stream Mach number with two curves showing the airfoil dependent and independent curve respectively

The M_{cr} has an effect on the drag term of the propeller. If a local Mach number higher than the critical Mach number is present, an additional drag term from a simple drag rise model is added in XRotor. This can be seen in the following equation

$$\Delta C_d = K(M_{local} - M_{cr})^n \tag{3.5}$$

where n is an exponent which is set to 3 by default in XRotor and K is a scaling constant.
The rest of the input parameters for XRotor are determined using XFoil. In Figure 3.3 a flowchart is depicted showing how the performance calculations are performed and how this is implemented. After the propeller geometry and operational condition are defined, the variables are initialised. The local Reynolds number should be computed first. The viscosity option is turned on and the Reynolds numbers are given as input. The Mach number is set to zero in XFoil. If a Mach number is given, XFoil performs a compressibility correction using the so-called Prandtl-Glauert rule which is also shown in equation 3.4. XRotor uses the same Prandtl-Glauert correction for the compressibility as in XFoil. In order to avoid this correction being applied twice, the Mach number given in XFoil is set to zero but the correct Reynolds number is given as input in XFoil. Every blade section that is defined is loaded in XFoil and a 2D aerodynamic dataset is created by running the tool. The angles of attack for which every section is run for is from -30 to 30 degrees with increments of 0.25 degrees. When XFoil has trouble finding a converging solution, it is run again and the settings are changed manually. For instance the number of iterations or the increments in angle of attack can be changed such that it is able to find a converging solution. Especially for thin airfoil sections this might be the case as thin airfoils have large panel angles for which XFoil sometimes has trouble finding a solution.
Another setting that is changed in XFoil has to do with the boundary layer around the airfoil which is effected by the level of turbulence that is used. This can be adjusted by using the e^n method. This method is used to simulate the effect of disturbances on the transition point. By changing the $n-value$, the turbulence level is changed and the transition point is shifted. The default value for n used within XFoil is 9 for the e^n method, which represents the situation of an average wind tunnel. A smaller value for n results in more turbulence being present in the freestream flow and vice versa. In [27] a sensitivity analysis is performed on the use of e^n and the effect on the calculated propeller performance data. It is found that for $n = 0.01$ the smallest deviations are obtained between experimentally determined

performance coefficients and the ones computed by XRotor. Therefore the same value for n is chosen in this thesis. After XFoil is run and a 2D aerodynamic data set is created, a fitting is performed. The input for this fitting are the lift, drag and moment coefficients together with the corresponding angles of attack. The output of this fitting are the other input parameters for XRotor that are given in the previous section which are not assumed. All the input variables are written in an inputfile for XRotor with a specified format. In XRotor the settings can be changed as well. As is addressed before the potential formulation is used for the calculation of the induced velocities of propeller blade sections. Furthermore, the number of iterations is set to 150 which is found to be sufficient. Often a convergence is achieved before this amount of iterations is reached. When XRotor is run, all the outputs are written in a specified file. This is then checked for convergence and the performance coefficients and induced velocity components are obtained. The flowchart depicted in Figure 3.1 is continued with the noise calculation which is discussed in the section 3.3.1.

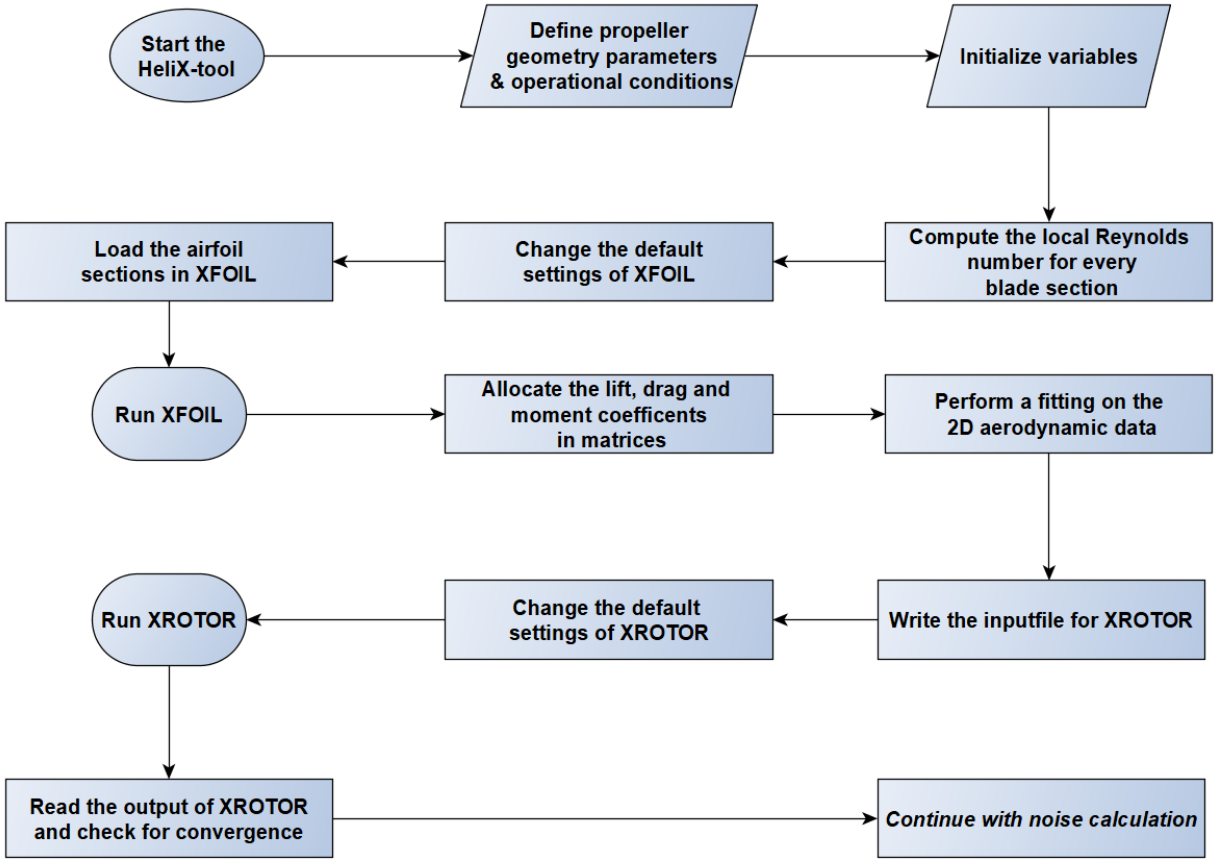

Figure 3.3: Flowchart of the performance calculation and the implementation in the HeliX-tool

3.3. Helicoidal Surface Theory

Hanson developed a frequency domain method to predict the propeller noise characteristics. This method is called the Helicoidal Surface theory [25]. It includes the effect of blade thickness, blade loading, forward flight and blade sweep. The latter being included as a phase lag effect. The forward flight is included by adding a Doppler shift term which changes the frequency heard by the observer depending on the location of the source and observer and the relative velocity between the two. Hanson assumed that the thickness and loading sources act on the advance helix which is the surface swept by a radial line that rotates at a certain angular speed and moves forward with the flight speed. When the angle of attack is determined with respect to the helical surface, the loading of a propeller blade can be determined. From this the harmonic sources can be predicted in the frequency domain using the helicoidal surface theory of Hanson. This method is based on the acoustic analogy of M.E. Goldstein (1976) [32]. This analogy was applied to moving surfaces within a moving medium. Goldstein's analogy contains three integrals and reads

$$c^2\rho'(x,t) = -\int_{-T}^{T}\int_{A(\tau)} \rho_0 V_N \frac{\delta G}{\delta \tau} dA(y)d\tau + \int_{-T}^{T}\int_{A(\tau)} f_i \frac{\delta G}{\delta y_i} dA(y)d\tau + \int_{-T}^{T}\int_{V(\tau)} T_{ij}\frac{\delta^2 G}{\delta y_i \delta y_j} dy d\tau, \quad (3.6)$$

where c is the speed of sound, ρ is the density where the subscript zero denotes the equilibrium value and ρ' denotes the acoustic density disturbance, V_N is the normal velocity of the surface relative to the fluid, T_{ij} is one element of the Lighthills stress tensor, f_i are the vector components of the force per unit area on the surface and G is the Green's function. $A(\tau)$ represents the impermeable surfaces at emission time τ and $V(\tau)$ the source volume. The integration is performed over the range of the source time from $-T$ to T.

The complete derivation for the far-field equations of the helicoidal surface theory can be found in [25]. The governing equations are described below. In the helicoidal surface theory the source strengths are based on the real blade geometry but are assumed to act on the mean surface of the blade. This assumption is based on the thin wing theory which allows the boundary conditions to be satisfied on the mean surface. As a result, a simplified mathematical expression is obtained to describe the steady loading noise and thickness noise. Furthermore, the quadrupole sources are omitted [24]. These sources account for the rise of non-linear effects that occur at high Mach numbers when for instance shock waves are formed. However, for the scope of this thesis Mach numbers above 1 are avoided making the assumption to omit the quadrupole sources a valid one. The focus is put on the steady tonal noise components of the propellers which are also described in section 2.2.3. Furthermore, axial inflow is assumed since the focus is put on steady tonal noise sources. When non-axial inflow is present, unsteady noise sources are present.
In equation 3.7 an expression is given for the acoustic pressure as an infinite sum over harmonics of the blade passage frequency and reads

$$p(t) = \sum_{m=-\infty}^{\infty} P_{mB} exp(-imB\Omega_D t), \quad (3.7)$$

where P_{mB} is the Fourier transform of the pressure at the mth harmonic of the BPF, B is the number of blades and Ω_D is the frequency corresponding to the angular speed with the Doppler effect accounted for. This angular velocity can be calculated with $\Omega_D = \frac{\Omega}{1-M_x cos\theta}$ where Ω is the angular speed, M_x is the axial Mach number and θ is the angle between propeller axis and the observer. In Figure 3.4 the angle θ is depicted. The distance between the source and the observer at emission time is referred to as r and the vertical distance is referred to as y.

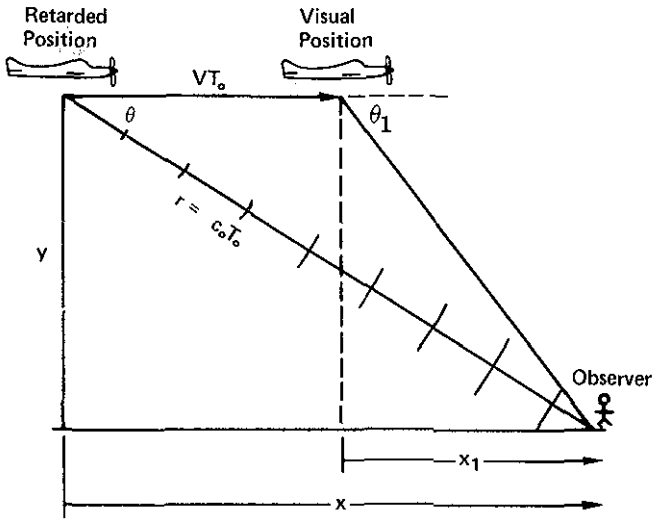

Figure 3.4: Definition of the radiation angle θ and the distances r and y as is used in the radiation equations[13]

The term P_{mB} consists of the following components:

- P_{Vm} volume displacement component
- P_{Dm} drag dipole
- P_{Lm} lift dipole

The term P_{mB} is calculated by adding the above mentioned components, $P_{mB} = P_{Vm} + P_{Dm} + P_{Lm}$. The noise contributors can be calculated using

$$P_{Vm} = -\frac{\rho_0 c_0^2 B \sin\theta \exp\left[imB\left(\frac{\Omega_D r}{c_0} - \frac{\pi}{2}\right)\right]}{8\pi(\frac{y}{D})(1 - M_x \cos\theta)} \times \frac{1}{2}\int_{root}^{tip} M_r^2 e^{i(\phi_0+\phi_s)} J_{mB}\left(\frac{mBzM_t \sin\theta}{1 - M_x \cos\theta}\right) \times 2k_x^2 t_b \psi_V(k_x) dz, \tag{3.8a}$$

$$P_{Dm} = -\frac{\rho_0 c_0^2 B \sin\theta \exp\left[imB\left(\frac{\Omega_D r}{c_0} - \frac{\pi}{2}\right)\right]}{8\pi(\frac{y}{D})(1 - M_x \cos\theta)} \times \frac{1}{2}\int_{root}^{tip} M_r^2 e^{i(\phi_0+\phi_s)} J_{mB}\left(\frac{mBzM_t \sin\theta}{1 - M_x \cos\theta}\right) \times ik_x C_D \psi_D(k_x) dz, \tag{3.8b}$$

$$P_{Lm} = -\frac{\rho_0 c_0^2 B \sin\theta \exp\left[imB\left(\frac{\Omega_D r}{c_0} - \frac{\pi}{2}\right)\right]}{8\pi(\frac{y}{D})(1 - M_x \cos\theta)} \times \frac{1}{2}\int_{root}^{tip} M_r^2 e^{i(\phi_0+\phi_s)} J_{mB}\left(\frac{mBzM_t \sin\theta}{1 - M_x \cos\theta}\right) \times -ik_y C_L \psi_L(k_x) dz, \tag{3.8c}$$

where y is the vertical distance between observer and the propeller axis, r is the distance from origin to observer point, D is the propeller diameter, C_L and C_D are the blade section lift and drag coefficients respectively. i is the imaginary unit defined as $i^2 = -1$ and m is the number of harmonics. t_b is the maximum thickness to chord ratio and is dependent on the geometry of the blade.

The non-dimensional wavenumbers k_x and k_y are defined as

$$k_x = \frac{2mBB_D M_T}{M_r(1 - M_x \cos\theta)}, \tag{3.9}$$

$$k_y = \frac{2mBB_D}{zM_r}\left(\frac{M_r^2 \cos\theta - M_x}{1 - M_x \cos\theta}\right), \tag{3.10}$$

where m is the harmonic of the blade passing frequency, B is the number of blades of the propeller, B_D is the chord to diameter ratio, M_t is the tip rotational Mach number, M_r is the effective Mach number which is dependent on the radial position and can be calculated with $M_r = \sqrt{M_x^2 + z^2 M_T^2}$ where z indicates the radial position of a blade element as a fraction of the radius and M_x is the flight Mach number.

ψ_V, ψ_D and ψ_L are distribution functions which are a dependent on k_x. ψ_V, ψ_D and ψ_L represent the chordwise distribution of the thickness, lift and drag respectively

$$\Psi_V(k_x) = \int_{-0.5}^{0.5} H(x) e^{ik_x x} dx, \tag{3.11}$$

$$\Psi_D(k_x) = \int_{-0.5}^{0.5} f_D(x) e^{ik_x x} dx, \tag{3.12}$$

$$\Psi_L(k_x) = \int_{-0.5}^{0.5} f_L(x) e^{ik_x x} dx \tag{3.13}$$

In equation 3.11 the term $H(x)$ is a normalised thickness distribution of the airfoil section that is considered. A propeller consists of different airfoil shapes and normally gets thinner closer to the tip. Therefore this thickness distribution function is dependent on the radial position of the blade element that is being considered. This is usually given by the propeller geometry. The maximum value of $H(x)$ is 1 and the integration is performed chordwise from -0.5 to 0.5 with -0.5 representing the leading edge of the airfoil and 0.5 the trailing edge of the airfoil. An example of such a function is given in Figure 3.5

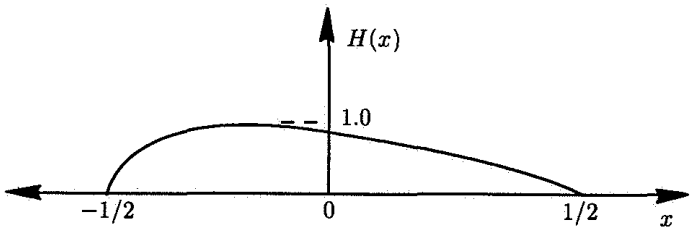

Figure 3.5: Normalised thickness distribution as is used in equation 3.11 [25]

Equations 3.12 and 3.13 also need to be integrated from the leading edge to the trailing edge. These distribution functions should be defined such that its area integrates to unity. The shape of these functions is defined by f_D and f_L and represent the chordwise drag distribution and chordwise lift distribution respectively and is dependent on the chordwise loading of a blade element. The chordwise loading for the drag is assumed to be constant in the calculation of the noise for this thesis. This means there is a chordwise uniform loading as can be seen in Figure 3.7. For the lift a strong peak chordwise lift distribution is assumed as can be seen in Figure 3.6.

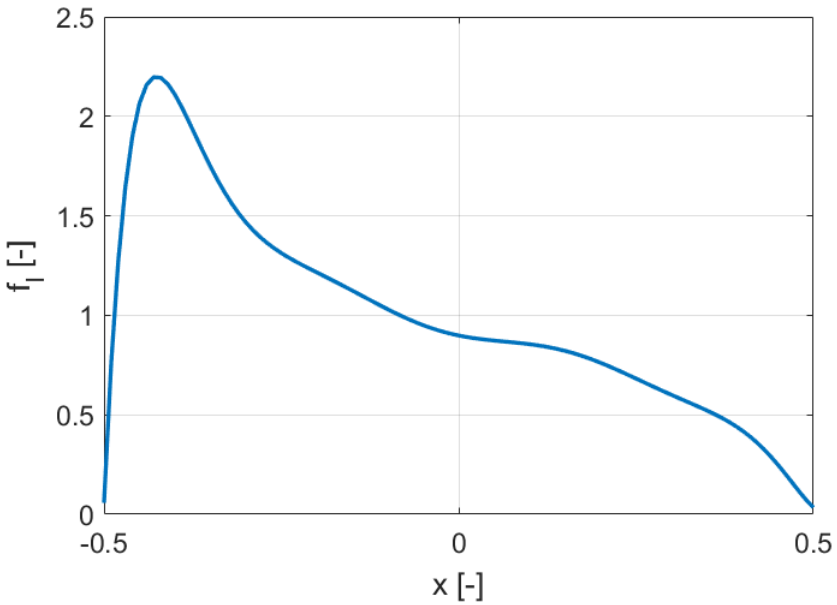

Figure 3.6: Chordwise lift distribution assumed

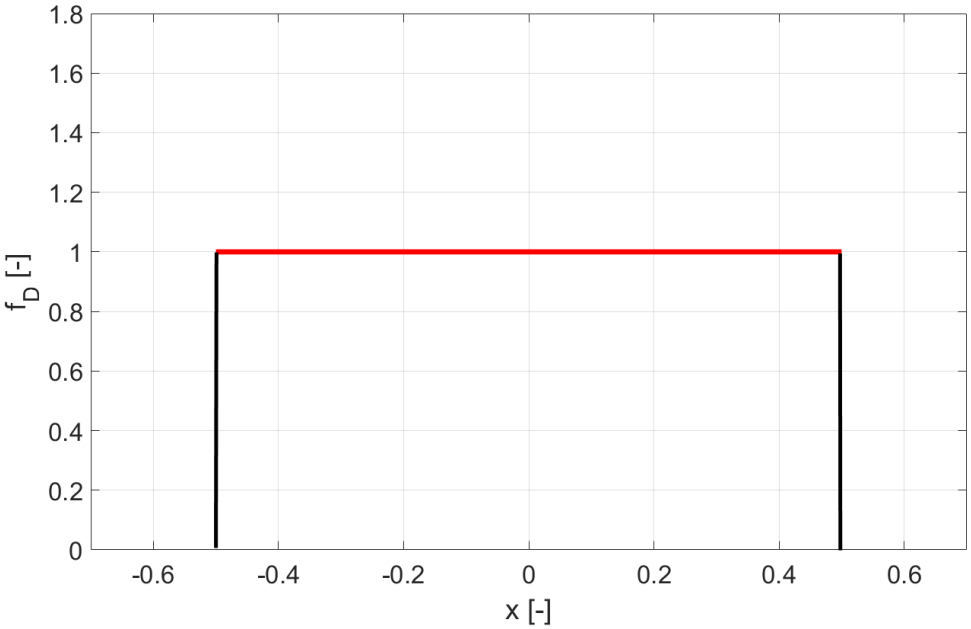

Figure 3.7: Chordwise drag distribution assumed

If sweep is present in the geometry of the propeller then it can be included in equation 3.8 by making use of a phase lag, ϕ_s. In equation 3.14 an expression for this phase lag is given

$$\phi_s = \frac{2mBM_T}{M_r(1 - M_x \cos\theta)} \frac{MCA}{D}, \tag{3.14}$$

where MCA stands for Mid Chord Alignment and is depicted in Figure 3.8a. D is the diameter of the propeller. Next to a phase lag due to sweep it is also possible to include a phase lag due to offset which is indicated with ϕ_0. This term can be calculated using the following expression

$$\phi_0 = \frac{2mB}{zM_r}\left(\frac{M_r^2 \cos\theta - M_x}{1 - M_x \cos\theta}\right)\frac{FA}{D}, \tag{3.15}$$

where FA stands for the Face Alignment and is the distance normal to the blade at the tip. The blade offset and sweep are only used if this is present in the propeller geometry that is treated.

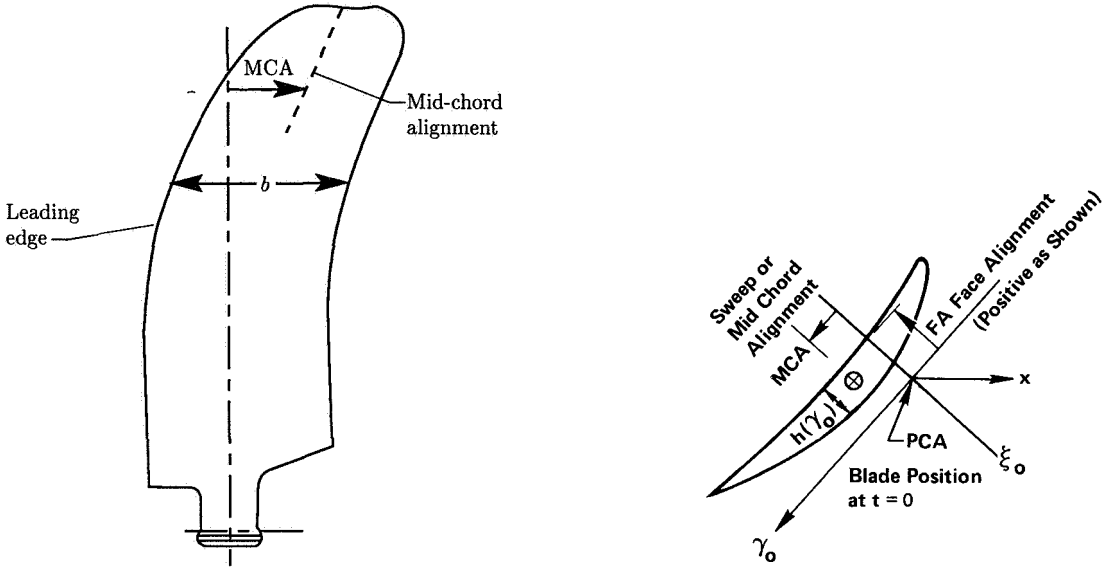

(a) Propeller blade planform and sweep [25]

(b) Face Alignment [25]

Figure 3.8: Propeller geometry definition

In equation 3.8 a Bessel function is used. The Bessel function J_{mB} is one of the first kind and has an order of mB. The argument of the Bessel function in the helicoidal surface theory is $\frac{mBzM_t \sin\theta}{1-M_x \cos\theta}$. The Bessel function is dependent on several parameters like the number of harmonics m and the number of blades B. For each section of the blade the Bessel function needs to be evaluated. This is done using the built-in function of Matlab for the Bessel function of the first kind, 'besselj'. In Figure 3.9 the besselfunction of the first kind is depicted for different orders and argument 'x'. It can be seen that the maximum absolute value of J decreases when the order is increased or when the argument is increased. The Bessel function shows an oscilating pattern with slower oscilations when the order is increased.

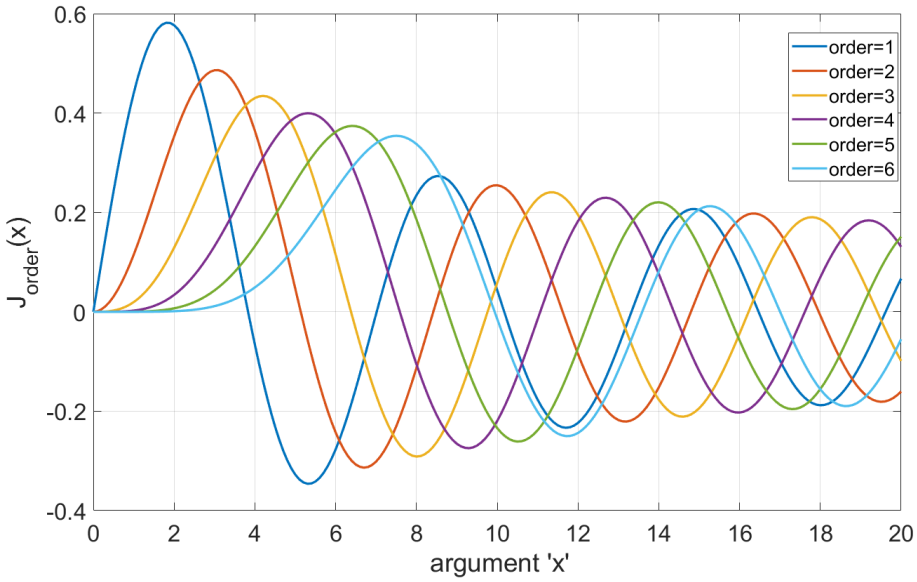

Figure 3.9: Besselfunction for different orders and argument 'x'

Finally, the lift and drag coefficients used in equation 3.8 need to be defined in the advance direction. The coeficients obtained from the propeller performance tool XRotor however are slightly rotated due to the induced effects of the propeller as can be seen in Figure 3.10.

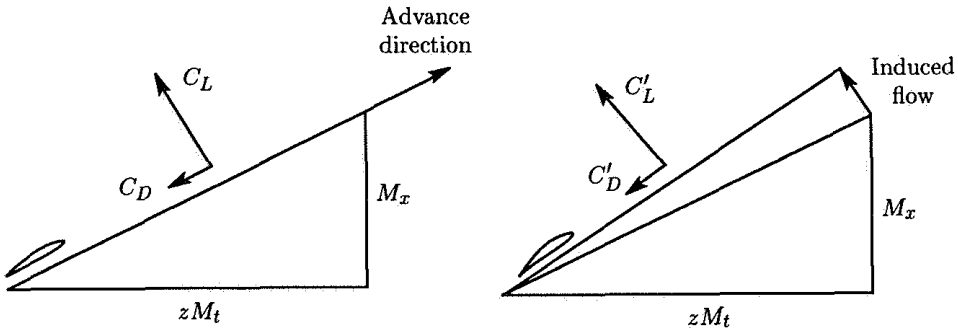

Figure 3.10: Lift and drag axes in advance direction and including induced flow [25]. Note that the term z is also referred to as $\frac{r}{R}$.

A correction needs to be performed before using the coefficients in the calculation of the noise signal. In order to do this a velocity diagram is depicted in Figure 3.11 showing the induced velocities.

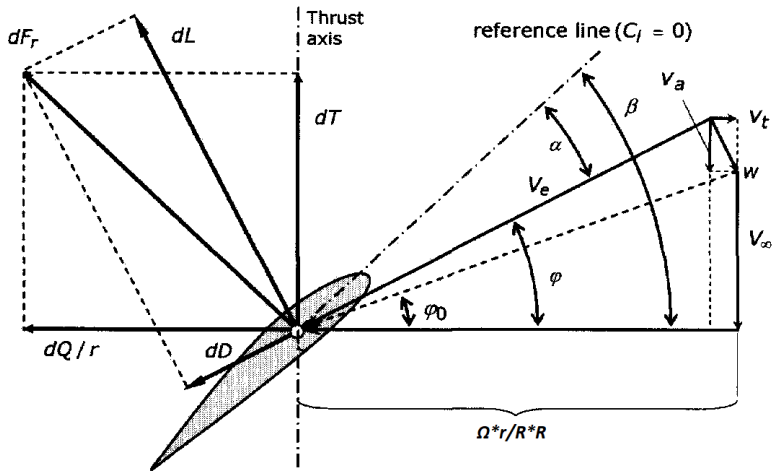

Figure 3.11: Velocity diagram including the induced velocity

The local angle of attack α_i and the local pitch anagle β_i are known from running XRotor and the propeller geometry respectively. The inflow angle including the induced effects, which is depicted in the figure with ϕ_i (here the subscript i denotes that it is a local angle of a blade section) can be calculated using the following relation

$$\phi_i = \beta_i - \alpha_i \tag{3.16}$$

The local inflow angle neglecting the induced effects ϕ_{i0} can be calulated using the following expression

$$\phi_{i0} = \tan^{-1}\left(\frac{V_\infty}{\Omega\frac{r}{R}R}\right), \tag{3.17}$$

where R is the propeller radius and $\frac{r}{R}$ is the radial blade location relative to the radius. The induced angle can now be computed with

$$\phi_{induced} = \phi_i - \phi_{i0} \tag{3.18}$$

The effective velocity seen by a propeller blade section including the induced velocity effects is given by

$$V_e = \sqrt{(V_a + V_\infty)^2 + (\Omega\frac{r}{R}R - V_t)^2}, \tag{3.19}$$

where V_a is the induced velocity component parallel to the axis of rotation and the V_t is the induced velocity component perpendicular to the axis of rotation.
Now the shift correction can be applied using the following expressions given in equation 3.20 and equation 3.21.

$$C_l = \frac{V_e^2}{(V_\infty + \Omega\frac{r}{R}R)^2}\left(C_l^{'}\cos(\phi_{induced}) - C_d^{'}\sin(\phi_{induced})\right) \tag{3.20}$$

$$C_d = \frac{V_e^2}{(V_\infty + \Omega\frac{r}{R}R)^2}\left(C_l^{'}\sin(\phi_{induced} + C_d^{'}\cos(\phi_{induced})\right) \tag{3.21}$$

After all the calculations are performed the acoustic pressure can be obtained as follows. Instead of using 3.7 the following expression can be used [13]

$$p(t) = 2Re\left[\sum_{m=1}^{\infty} P_{mB} exp(-imB\Omega t)\right], \tag{3.22}$$

where $'Re'$ refers to the real part of the Fourier coefficients. Here the summation is performed only for positive harmonic numbers and the factor is used to account for the negative harmonics. After having obtained the acoustic pressure signal in time. The sound pressure level and other relevant parameters can be computed.

3.3.1. Implementation of the Helicoidal Surface theory

In this section the implementation of the Helicoidal Surface theory in the HeliX-tool is described. A distinction is made between the loading noise components and the thickness noise component. The Fourier coefficients of the thickness noise component can be calculated without needing data from XRotor as it is not dependent on the loading of the blade but on the effective Mach number and the airfoil thickness distribution of the blade. In Figure 3.12 the flowchart of the thickness noise calculation is given. For the calculation of the thickness noise component the effective, axial and rotational Mach number need to be computed. These are then used in the calculation of the non-dimensional wavenumbers. These wavenumbers are furthermore also dependent on the radiation angle θ as can be seen in equations 3.9 and 3.10. For the calculation of the thickness noise component, the chordwise thickness distribution is normalized such that a maximum of 1 is obtained as can be seen in equation 3.13. Now the thickness source term Ψ_V can be computed for the several radially defined blade sections. This term is also dependent on the wavenumber k_x as can be seen in equation 3.11. Next, the Besselfunction of the first kind is computed for every blade section and multiple orders. Finally, the complex Fourier coefficients for the thickness source component are computed.

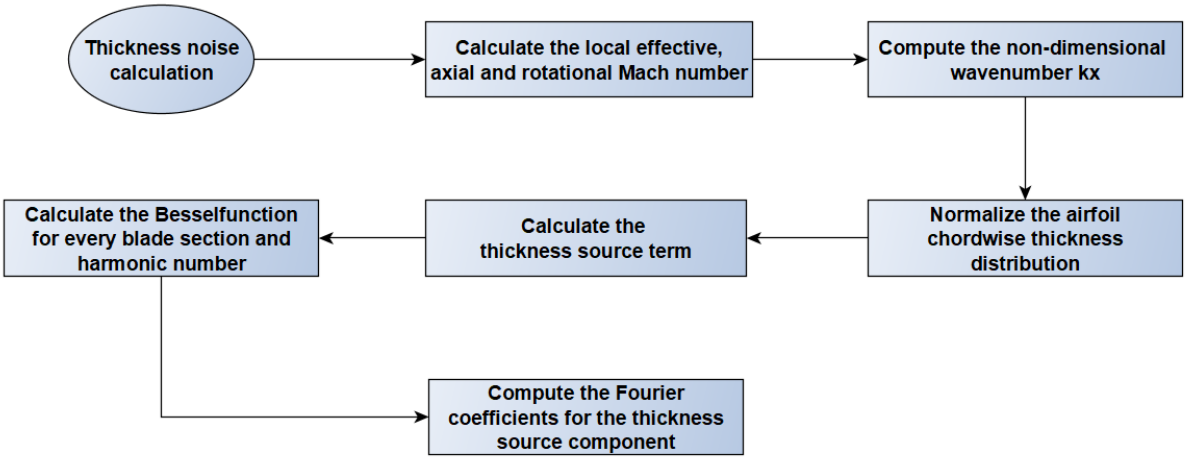

Figure 3.12: Flowchart of the thickness component component and the implementation in the HeliX-tool

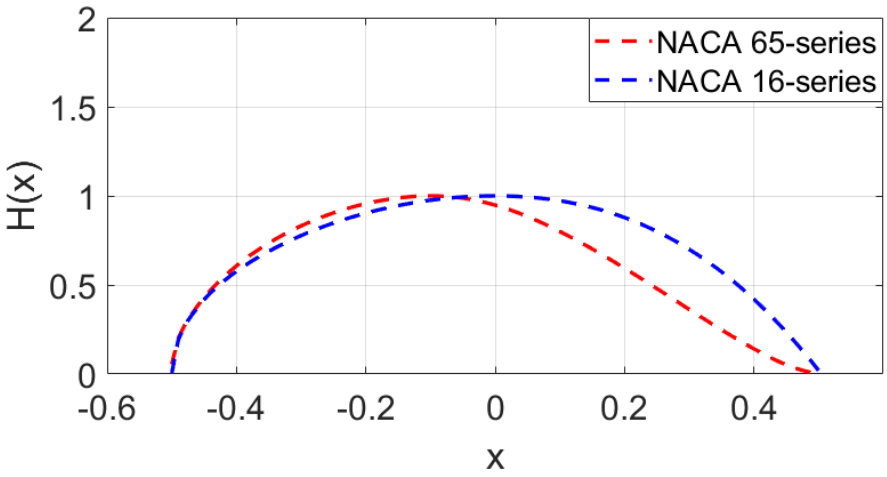

Figure 3.13: Normalized thickness distribution with the leading edge starting at 0.5 and the trailing edge at -0.5

In Figure 3.14 the flowchart of the approach to calculate the loading noise is depicted. Contrary to the thickness noise calculation, the loading noise calculation does require the lift and drag coefficients of the blade sections from XRotor. As is mentioned in section 3.3 a correction needs to be performed due to the induced effects. The coefficients need to be obtained in the advance direction. One of the outputs of XRotor are the induced velocity components together with the local angle of attack. These are used for the correction. The loading noise component requires the two non-dimensional wavenumbers, k_x and k_y. These are computed once and are also used in the thickness noise source calculation (only k_x). As is mentioned before, the chordwise lift and drag distribution are assumed to have a peaky and uniform chordwise distribution respectively for every blade section. These are to compute the loading source term. Again, the Bessel function of the first kind is computed for every blade section and multiple orders are needed. Finally, the complex Fourier coefficients for the loading noise components are computed. Here a distinction is made between the lift and drag component.

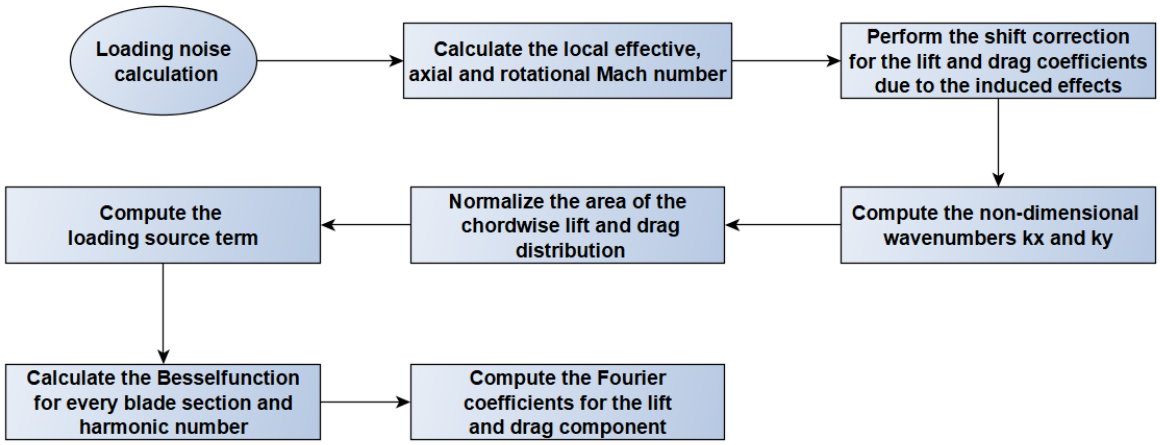

Figure 3.14: Flowchart of the loading noise component and the implementation in the HeliX-tool

After the Fourier coefficients are obtained, the noise is computed. First the Fourier coefficients are added together. Then the propeller noise time signal are computed using the Fourier series. This can be found in equation 3.22. In order to calculate the SPL values for different frequency bands, a DFT is performed for the chunk of data obtained from the propeller noise time signal. Then the power spectral density is calculated of each chunk of data. At last the SPL values are computed as a function of the frequency. Additionally, the OSPL is computed from the time signal. For this the effective pressure is

required from the time signal. When the effective pressure is computed the OSPL is obtained which gives the SPL taking into account all frequencies together.

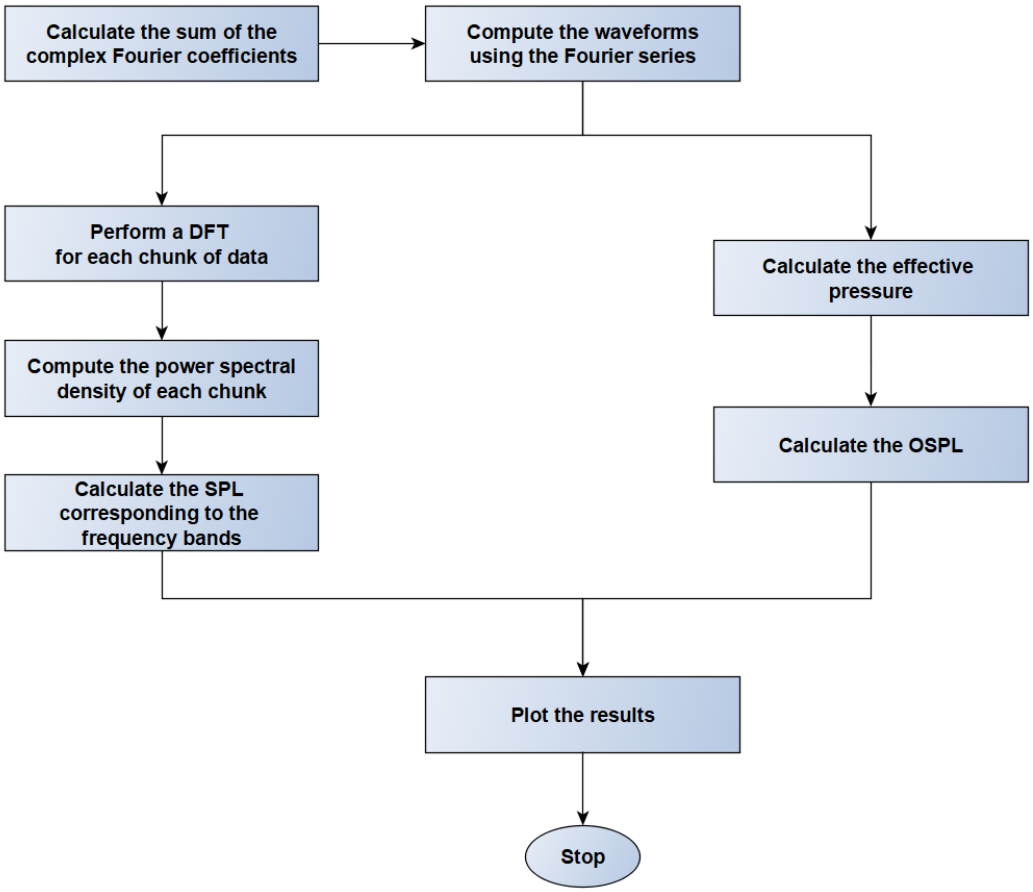

Figure 3.15: Flowchart of the noise calculation and the implementation in the HeliX-tool

4

Validation

As can be seen in the flow diagrams of the HeliX-tool discussed before, a long chain of computations is performed when going form a certain propeller geometry to eventually the noise signals. It is therefore essential to perform a validation study. This chapter describes the validation process of the noise prediction tool that is developed, the HeliX-tool. Publicly available literature data is used for the validation. The NASA SR-2 propeller is selected and utilized for the validation discussed in this chapter. A description of the NASA SR-2 propeller is given in 4.1. Furthermore a comparison is made with an existing propeller noise prediction tool developed at the NLR. This tool is described in section 4.2. Additionally, results obtained from comparisons made between literature data and the NLR-tools with the HeliX-tool are shown in section 4.3. At last, final remarks are given on the validation in section 4.3.3.

4.1. NASA SR-2 propeller

The SR-2 propeller is an 8-bladed propeller with a diameter of 0.622 meters and adjustable pitch developed at NASA. This propeller is extensively studied and documented, hence a lot of data is publicly available. It has a cruise design Mach number of 0.8 and a design advance ratio of 3.06. The propeller consists of 8 blades without sweep as is depicted in Figure 4.1.

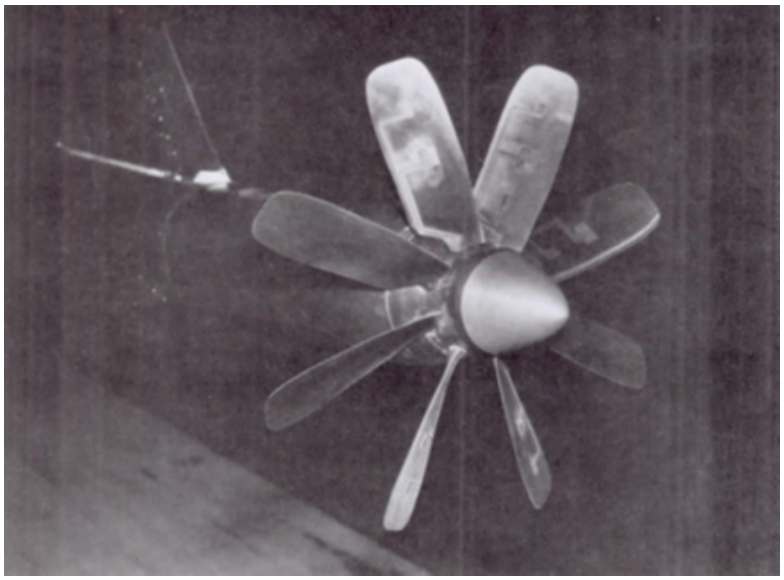

Figure 4.1: Photograph of the SR-2 propeller made in the windtunnel of the NASA Lewis Research Center [33]

The geometrical data of the SR-2 propeller is obtained from Figure 4.2. This figure shows the twist distribution of the blade relative to the twist at 75% of the blade radius indicated with $\Delta\beta$. Furthermore, the thickness distribution from the root to the tip is given indicated with $\frac{t}{c}$. At the hub the thickness-to-chord ratio is 21% while at the tip of the propeller the thickness-to-chord ratio is only 2%. From the root to the tip the propeller blade becomes thinner. Furthermore, the chord-to-diameter ratio is given which is referred to as $\frac{c}{D}$. At last the design lift coefficient, C_{LD}, of the blade sections is given as well.

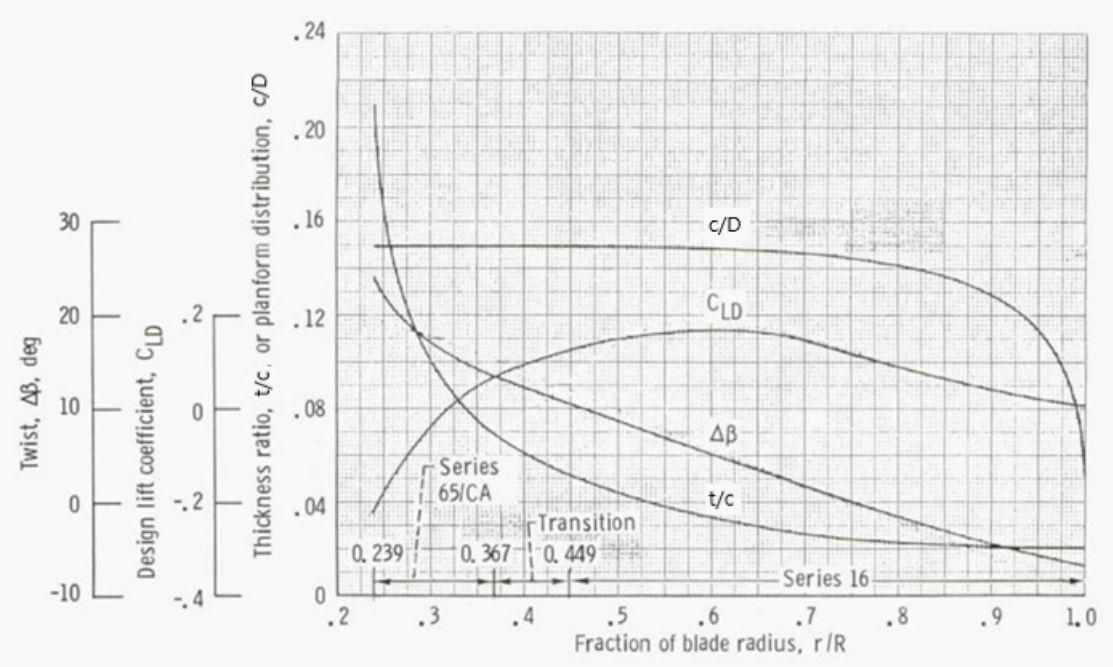

Figure 4.2: SR-2 propeller design parameters. The pitch β, thickness to chord ratio $\frac{t}{c}$, the chord to diameter ratio $\frac{c}{D}$ and the design lift coefficient C_{LD} are plotted as a function of $\frac{r}{R}$[33]

The propeller blade consists of mainly two airfoil types, namely the NACA-65 series with a circular arc camber and the NACA-16 series. From the root to approximately 37% of the radius the SR2-propeller has blade sections made from the NACA-65 series airfoil and from approximately 45% until the tip the blade sections consist of the NACA-16 series airfoil. In Figure 4.3 the two airfoil types are shown. For comparison reasons the two airfoils depicted both have a maximum thickness-to-chord ratio of 10%. Also, both airfoils have a design lift coefficient of 0.2. The design lift coefficient actually differs from the root towards the tip. At the root a negative design lift coefficient is present. When moving closer to the tip the design lift coefficient increases until approximately 62% of the radius after which it decreases again. The design lift coefficient is important for the determining the camber of the different airfoil sections. The airfoils used in this thesis are generated in JavaFoil [34]. This is a program that can be used to design and analyse airfoils. A nice feature of this program is that the airfoil design routine allows to give the design lift coefficient together with the the thickness-to-chord ratio as input. The airfoils are then generated.

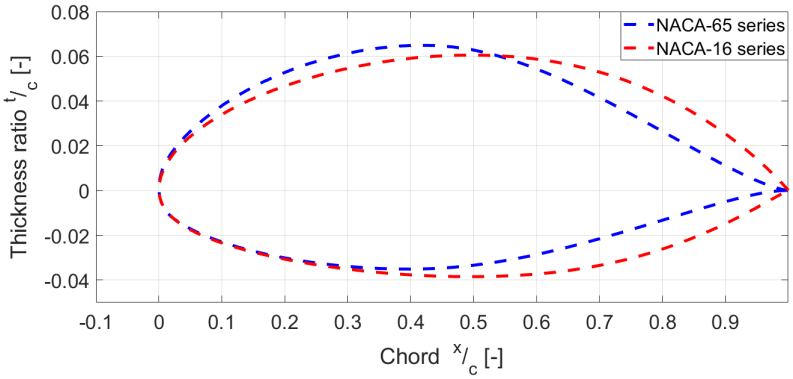

Figure 4.3: NACA-65 series and NACA-16 series airfoils with a maximum thickness-to-chord ratio of 10% and a design lift coefficient of 0.2

Figure 4.2 shows that from approximately 37% to 45% of the radius a transition region is present. In the transition region the airfoil neither consist of a NACA-65 series nor NACA-16 series airfoil. In the transition region the airfoil shape gradually changes from a NACA-65 series to a NACA-16 profile. It is therefore decided to use the capability of XRotor that allows to perform a linear interpolation in the region where no aerodynamic properties are given. This is applied in the transition region.
In total 18 blade sections are defined which can be seen in Table 4.1. Here the maximum thickness-to-chord ratio and the design lift coefficient are shown together with the airfoil type that is used.

Fraction of radius r/R [-]	**Maximum thickness ratio t/c [-]**	**Design lift coefficient C_{LD} [-]**	**Airfoil**
0.24	0.21	-0.216	65-series
0.27	0.129	-0.118	65-series
0.30	0.10	-0.0403	65-series
0.32	0.089	0	65-series
0.34	0.0785	0.0337	65-series
0.37	0.0682	0.0676	65-series
0.45	0.05	0.1254	16-series
0.50	0.044	0.1484	16-series
0.55	0.038	0.1601	16-series
0.60	0.033	0.1662	16-series
0.65	0.0295	0.1648	16-series
0.70	0.0261	0.1473	16-series
0.75	0.0238	0.1169	16-series
0.80	0.0226	0.0896	16-series
0.85	0.0213	0.0637	16-series
0.90	0.02	0.0391	16-series
0.95	0.02	0.0203	16-series
1.00	0.02	0.0072	16-series

Table 4.1: 18 blade sections that are used in the computation of the propeller performance

All the data of the SR-2 propeller is obtained from Figure 4.2 and is imported in Matlab. This is done using a function that allows to load the figure and set the limits of the y-axis and x-axis. It is then possible to click on the graph and generate points that are then saved as matrices. This way the error that could be present when reading data from the graph is minimized.
In Figure 4.4a and Figure 4.4b a 3D view of the SR-2 propeller is depicted. In Figures 4.4c and 4.4d a side view and a top view of the propeller is shown. In the side view it looks like the blade section which is the closest to the root has a smaller chord length than other sections. This is not the case since this effect is created by the rotation and in reality this is the section with the largest chord length. This can clearly be seen in Figure 4.4d that depicts the top view. It can also be seen that a small portion of the SR-2 propeller does not consist of blade sections in Figure 4.4c. This is the transition region as is addressed before. For each of these 18 blade sections the aerodynamic properties are obtained using XFoil. This is needed as input for XRotor as is described before in section 3.2.1.

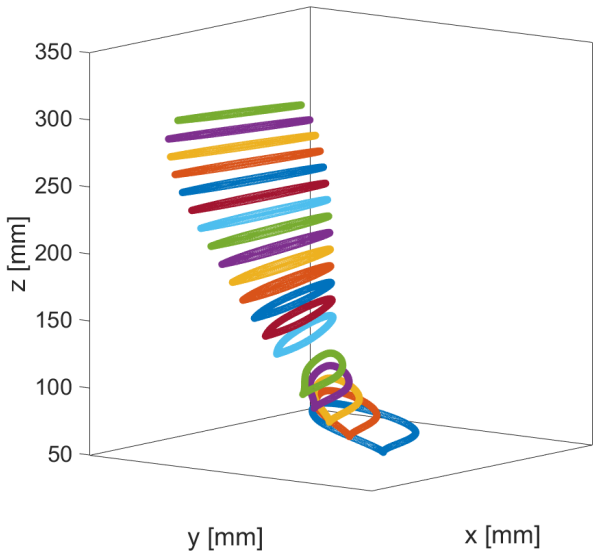

(a) 3D view of the SR-2 propeller blade with a radius of 0.311 meter, 1

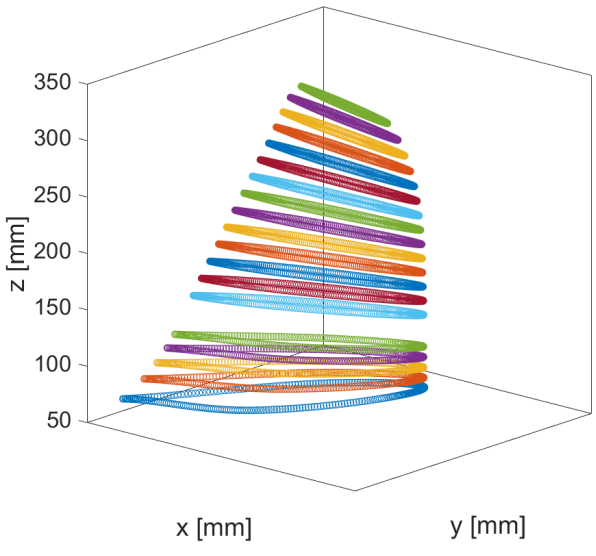

(b) 3D view of the SR-2 propeller blade with a radius of 0.311 meter, 2

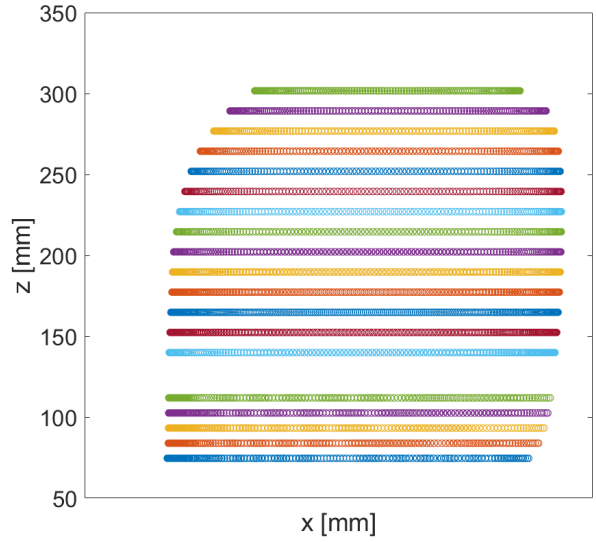

(c) Side view of the SR-2 propeller blade

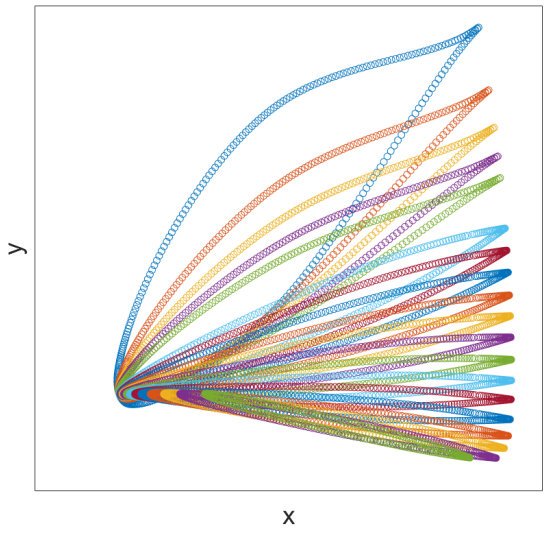

(d) Top view of the different blade sections

Figure 4.4: Plots showing different views of the SR-2 propeller blade

4.2. MAEPROP & ROLLAC

At the NLR, two programs are developed for the prediction of propeller noise, MAEPROP and ROLLAC. MAEPROP is a tool that is used to compute the performance and aerodynamics of propellers. The aerodynamic data generated by the MAEPROP program are subsequently used for the aeroacoustics calculation performed in the ROLLAC program. ROLLAC is a program which is used to perform aeroacoustic computations for propellers. In this section the MAEPROP and ROLLAC programs will be discussed. The principles behind the programs are explained briefly. Furthermore the inputs and outputs of each program are described. In this section the main assumptions that are used are discussed together with the limitations of MAEPROP and ROLLAC. The details of the theory behind MAEPROP and ROLLAC are out of the scope of this report but can be found in [35] [36].

MAEPROP is a program that is developed at the NLR to compute the aerodynamics and performance of conventional, high-aspect ratio propellers. The aerodynamics and performance of propellers is computed using a lifting line method. This lifting line method is based on the techniques of the matched asymptotic expansions method [35]. The matched asymptotic expansion method is not used explicitly but the principles behind it are used in the lifting line program, MAEPROP.
The aerodynamic computations in MAEPROP are divided into two parts that are related to each other. One part is the computation of the 2D flow about the propeller blade sections. The second part is the computation of the induced velocity by making use of a system consisting of bound and free vortex lines. The strength of the vortices can be determined when the loading is known. Thus the 2D flow about a propeller blade section is coupled to the 3D wake.
The main equation that needs to be solved for the aerodynamic part is an integral equation for the distribution of the circulation about the propeller blade sections. This equation is solved using the Galerkin method. The Galerkin method is used to compute approximate solutions of integral equations. Furthermore, the thin-airfoil theory is used to obtain the airfoil characteristics. Usually this is accurate enough for the acoustic computations [37]. By using the thin-airfoil theory, the numerical problem is simplified significantly. The thin-airfoil theory states that an airfoil can be represented by a vortex sheet. The lift generated by this vortex sheet can then be calculated by determining the strength of the vortices that are distributed along the camber-line of the airfoil.

In Figure 4.5 the coordinate system used in MAEPROP and ROLLAC is shown.

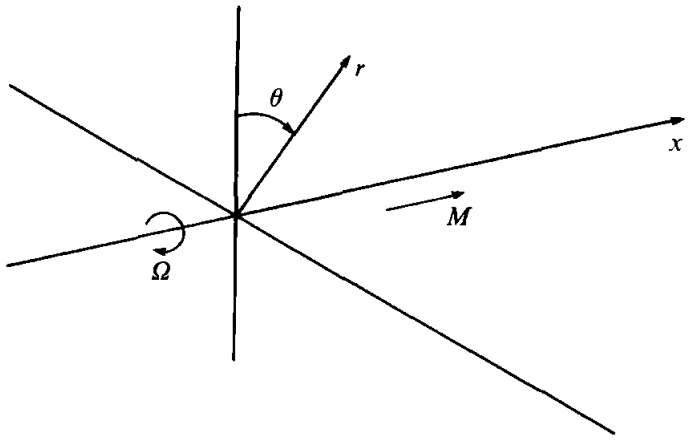

Figure 4.5: Cylindrical coordinate system used in MAEPROP and ROLLAC [36]

In MAEPROP the loading is determined using a relation which is obtained from the thin airfoil theorem:

$$C_l = 2\pi(\alpha - \alpha_0), \tag{4.1}$$

where C_l is the 2D lift coefficient for the airfoil, α is the angle of attack, and α_0 is the zero-lift angle of

attack. The angle of attack α is given by:

$$\alpha = \beta - \phi - \alpha_i, \tag{4.2}$$

where β is the local pitch angle, ϕ is the local inflow angle and α_i is the induced angle of attack. The induced velocity is required to determine the 2D flow about the propeller blade sections and thus the loading of the blade. The lift is furthermore assumed to be perpendicular to the local undisturbed flow. In order to determine the lift, the circulation about each blade section needs to be computed. In MAEPROP the perturbation of the flow is obtained from the vortex strength only [36]. The strength of the vortex is related to the lift by the Kutta-Joukowsky theorem:

$$\Gamma = 0.5\, C_l\, c\, M_r, \tag{4.3}$$

where M_r is the section relative Mach number, Γ is the vortex strength and c is the local blade chord. The aerodynamic problem which is divided into two parts require output data from each other. Therefore iterations are performed in the program until a converged solution is found. Once the circulation is known, the acoustic pressure can be determined using the program ROLLAC. The derivations of the governing equations used in ROLLAC can be found in [36]. This derivation starts with a linearized version of the Euler equations. The convective wave equation is then derived from these Euler equations. By making use of the Green's function and Bessel function an expression is derived for the complex pressure coefficient. Only the result of this derivation will be shown here. The complex pressure coefficient a_{mB} that is computed in ROLLAC reads:

$$\begin{aligned} a_{mB} = \frac{B}{4\pi} \int_0^1 d\rho \int_0^\infty d\gamma \Gamma(\rho) \frac{\gamma J_{mB}(\gamma r) J_{mB}(\gamma \rho)}{\kappa(\gamma, -mB\Omega)} \times \left\{ \frac{u_\theta}{\beta^2} (MmB\Omega + sgn(x)\kappa(\gamma, -mB\Omega)) + \frac{mBu_x}{\rho} \right\} \\ \times exp\left[\frac{-ix}{\beta^2} (MmB\Omega + sgn(x)\kappa(\gamma, -mB\Omega)) \right], \end{aligned} \tag{4.4}$$

where B is the number of blades, γ is the radial wavenumber, ρ is the radial source coordinate (not to be confused with the density), r is the radial coordinate, J_{mB} is a Bessel function of the first kind and of order mB. The variable x is the axial coordinate as is shown in the coordinate system in Figure 4.5, Ω is the angular velocity of the propeller, κ is a function, θ is the angular coordinate, u_x and u_θ are components of the local fluid velocity relative to the blade in axial and angular direction respectively. At last $\Gamma(\rho)$ is the vortex strength as a function of the radial source coordinate and β is a correction factor for the compressibility also known as the Prandtl-Glauert correction factor given by $\sqrt{1 - M^2}$. Just like with the Helicoidal Surface theory, the acoustic pressure can then be obtained with the following expression:

$$p(t) = \sum_{m=-\infty}^{\infty} a_n exp(-imB\Omega t), \tag{4.5}$$

As is mentioned before, MAEPROP is a tool that estimates the performance and aerodynamic characteristics of high aspect ratio propellers. The term 'high aspect ratio' is mentioned explicitly as one of the assumptions made in MAEPROP is that the chord of the propeller blade is much smaller than the radius. Therefore MAEPROP is more suitable to use for high aspect ratio propellers. Furthermore it can only handle helical tip velocities that are in the subsonic region. Further details about MAEPROP regarding the code is beyond the scope of this thesis and is also company confidential information. More important is that MAEPROP and ROLLAC are proven to work properly and are validated by the NLR. Computations are performed for a Fokker 50 propeller by the NLR. These results are compared with measurements and a reasonable agreement in performance data as well as noise data was found [38] [35]. MAEPROP and ROLLAC are therefore considered suitable tools to use for the validation process of the HeliX-tool.

Inputs & Outputs
In order to get an idea of how much data is required to perform the computations described above, the inputs and outputs of MAEPROP and ROLLAC are described below.
The list of inputs needed to run MAEPROP is the following:

- The number of blades
- Radius of the hub
- Circumferential tip Mach number
- Axial Mach number
- Blade angle at 70% of the blade radius
- Power coefficient
- Thrust coefficient
- Number of blade sections (maximum of 20)
- Name of the file containing the blade geometry

In order to run MAEPROP a so-called secfil is needed. This file contains the geometry for the propeller of interest. No detailed description of the airfoil is needed but only a few characteristics. The description of the propeller geometry is given by the following data:

- Radial coordinate of blade section
- Local chord length
- Twist angle, relative to the blade angle at 70% of the blade radius
- The zero-lift angle
- Area of the blade section
- Pitching moment coefficient
- The relative position of the leading edge of each blade section (made dimensionless by dividing by the local chord)

Data that contain information about lengths are made dimensionless by dividing it by the radius unless stated otherwise.

The outputs obtained with MAEPROP are:

- Number of blades
- Number of blade sections
- Radial coordinate of blade section
- Local chord length of blade section
- Rotational tip Mach number
- Flight Mach number
- Hub radius
- Negative of sectional zero lift angle
- Area of blade section

- μ_0 which is a constant determined by the camber line of the blade section
- Relative position of the leading edge
- Sectional lift coefficient
- Induced angle of attack

The above listed outputs of MAEPROP are used as input for the aeroacoustic lifting line program ROLLAC. Note that some of the inputs are also listed as outputs but since they are obtained in the output file of MAEPROP they are also listed as an output. Next to the outputs mentioned above, ROLLAC also requires data describing the 'listener positions'. This has to be provided to ROLLAC in a so-called 'field-in' file:

- Number of points in x-direction (see coordinate system in Figure 4.5
- Array containing the x-coordinates
- Radial coordinate
- Circumferential coordinate
- Harmonic number
- Angle between main flow and propeller axis
- Circumferential position of propeller blade at t=0

One of the inputs that can be seen above is the 'angle between main flow and propeller axis'. MAEPROP and ROLLAC were originally developed to cope with axial inflow for propellers. Later the ability to compute the noise for a propeller with an angle of attack is added. This is added based on linear corrections and is only valid for small inflow angles. For this thesis axial inflow is assumed and therefore this ability will not be used.

4.3. Comparison

A comparison between theoretical results and measurements is made in this section. First a comparison is made regarding the propeller performance. This is done because the acoustic results are for a great part dependent on the performance of the propeller. The thrust coefficient and power coefficients calculated by the NLR-tool MAEPROP and the HeliX-tool (XRotor in particular) are compared to experimentally obtained data. This comparison is given in section 4.3.1. Also acoustic data obtained from the HeliX-tool and NLR-tool are compared with each other as well to the experimental data. Several operating conditions and propeller configurations are used for this. The acoustic results are given in section 4.3.2 Finally, a conclusion and final notes are given regarding the comparisons made in 4.3.3.

4.3.1. Performance results

For the SR-2 propeller model, an extensive set of performance data is available. From [33] aerodynamic data of the 8-bladed SR-2 propeller model is obtained. The measurements are performed in the NASA Lewis 3.05 meters by 3.05 meters (10 foot by 10 foot) Supersonic Wind Tunnel. The propeller was used with different blade angles at different free-stream Mach numbers. The tunnel flow Mach numbers represent takeoff, landing and climb conditions. The test run schedule that is used for the experimental measurements is depicted in Figure 4.6.

Blade angle at 75 percent radius, deg	Mach number			
	0.10	0.20	0.27	0.34
24.9	X	X	–	–
29.6	X	X	–	–
34.4	X	X	X	–
38.0	X	X	X	–
41.7	X	X	X	X
45.8	–	X	X	X
49.8	–	X	X	X
53.8	–	–	X	X
59.7	–	–	X	X

Figure 4.6: Test run schedule of the SR-2 propeller [33]

The performance data that is presented in [33] are also generated with the HeliX-tool and MAEPROP. The operating conditions that are used for this have a flow Mach number ranging from 0.1 to 0.34 as can be seen in the test run schedule depicted in Figure 4.6. For the validation of the HeliX-tool, three tunnel flow Mach numbers are selected. These are 0.1, 0.2 and 0.34. For each tunnel flow Mach number, one blade setting is chosen for comparison.
In Figure 4.7a, the thrust coefficient as a function of the advance ratio is depicted for a tunnel Mach number of 0.1 and $\beta_{0.75} = 38\,\mathrm{deg}$. For the same operating condition the power coefficient as a function of the advance ratio is depicted in Figure 4.7b. Good agreement can be found between the HeliX-tool and the experimentally obtained values. The computed power coefficient data obtained by the HeliX-tool follow the trend better compared to the data obtained from MAEPROP. For the thrust coefficient, the difference is smaller between the HeliX-tool and MAEPROP. Furthermore, a constant overprediction is obtained for the power coefficient for the HeliX-tool

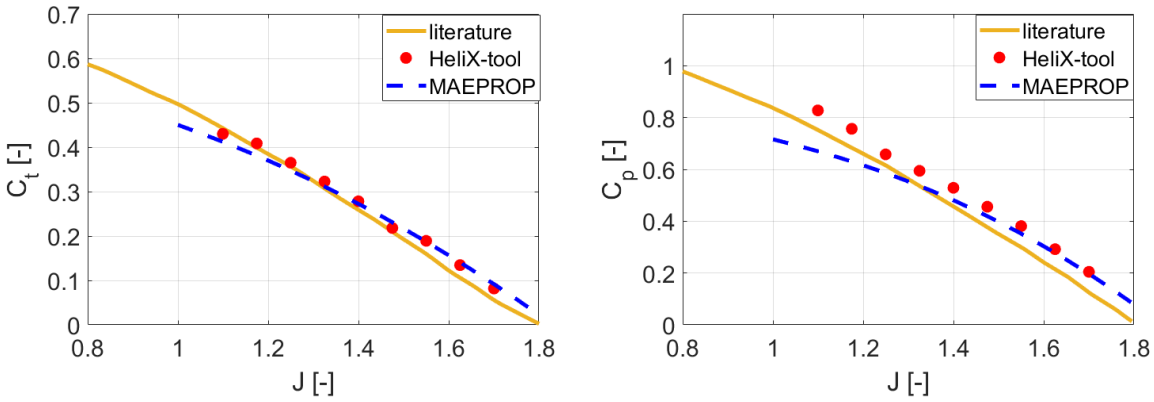

(a) Thrust coefficient as a function of the advance ratio (b) Power coefficient as a function of the advance ratio

Figure 4.7: The thrust and power coefficient axial Mach number of 0.1 and $\beta_{0.75} = 38\,\mathrm{deg}$

In Figure 4.8 the helical tip Mach number is shown as a function of the advance ratio. Figure 4.8 is generated using the relation between the helical tip Mach number and the advance ratio. The helical tip Mach number is computed using the following

$$M_h = \sqrt{M_x^2 + M_T^2}, \tag{4.6}$$

where M_T is the rotational tip Mach number. This is computed using the following relation

$$M_T = \frac{n\,D}{c}, \tag{4.7}$$

where n is the number of revolutions per second and c is the speed of sound. The helical tip Mach number is computed for the same range of J for which data is obtained in Figure 4.7. This is done in order to better understand the relation between the highest Mach number present, which is the helical tip Mach number, and the performance coefficients. For lower advance ratio, the rotational speed is increased and thus the helical tip mach number is increased. For higher speeds the performance results typically show higher thrust and power coefficients.

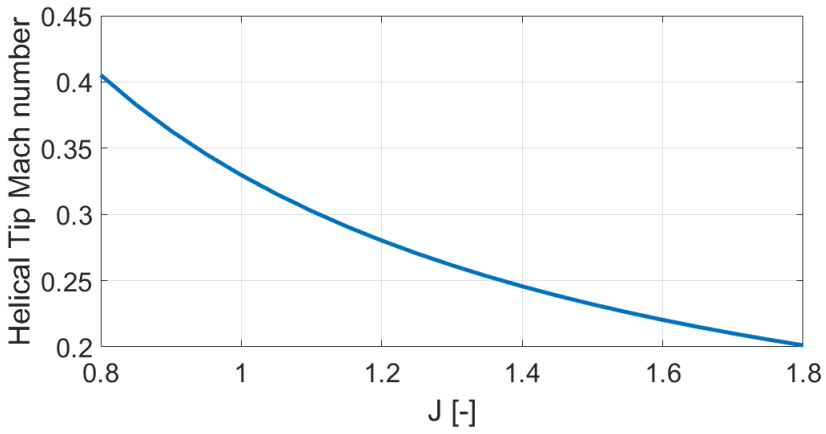

Figure 4.8: Helical tip Mach number as a function of the advance ratio J for $M_x = 0.1$

In Figure 4.9a, the thrust coefficient as a function of the advance ratio is depicted for a tunnel Mach number of 0.2. Now the blade angle is set to $\beta_{0.75} = 45.8\,\mathrm{deg}$. For the same operating condition the power coefficient as a function of the advance ratio is depicted in Figure 4.9b. Again a good agreement can be found between the HeliX-tool and the experimentally obtained values. A constant overprediction of the thrust coefficient is obtained from the predictions of the HeliX-tool. The same holds for the power

coefficient. For the HeliX-tool prediction of the performance, the same range of advance ratio is used as in MAEPROP. It can be seen that the HeliX-tool did not converge for the complete range of advance ratios from the fact that there are no data (red dots) for small values of the advance ratio. This could possibly be due to a large section of the blade being stalled. A lower advance ratio results in larger inflow angles. With the current blade setting this can mean that large angles of attack are present at the blade sections. Considering that the SR-2 propeller consists of blade sections at the outer region with a thickness smaller than 3%, a great portion of the blade is more prone to stall. MAEPROP on the other hand does give results for this region. This has to do with the simple model that MAEPROP is based on. It neglects the occurence of stall. This can lead to an overprediction of the trust coefficient. The HeliX-tool computes the performance using XRotor, which is also based on a lifting line model but is slightly more sophisiticated as it uses a crude stall model to merge the linear and non-linear lift regions.

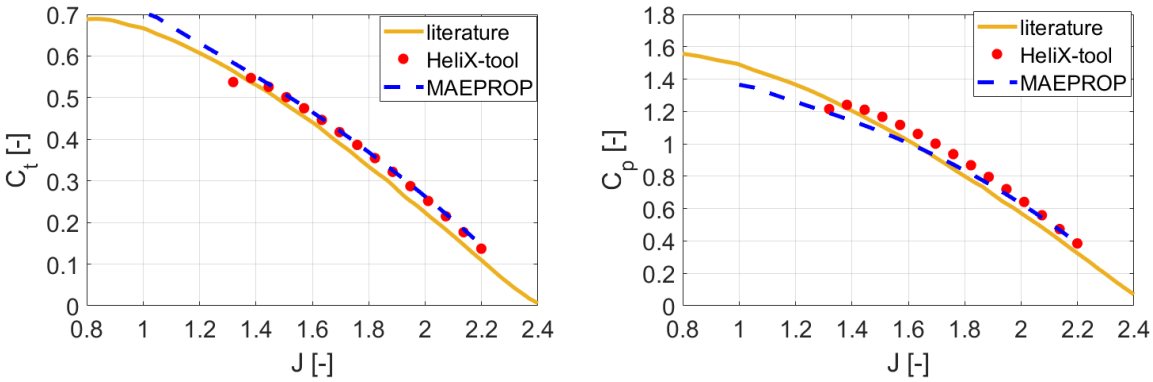

(a) Thrust coefficient as a function of the advance ratio (b) Power coefficient as a function of the advance ratio

Figure 4.9: The thrust and power coefficient axial Mach of 0.2 and $\beta_{0.75} = 45.8\,\mathrm{deg}$

In Figure 4.10 the helical tip Mach number is shown as a function of the advance ratio. This is done for the same range for which data is obtained in Figure 4.9. Again, the rotational speed is increased and thus the helical tip Mach number is increased for lower advance ratios. The helical tip Mach number ranges from approximately 0.32 to 0.8 Mach. These are larger compared to the previous operating condition. It seems that for large helical Tip Mach numbers the deviation increases when comparing performance coefficients.

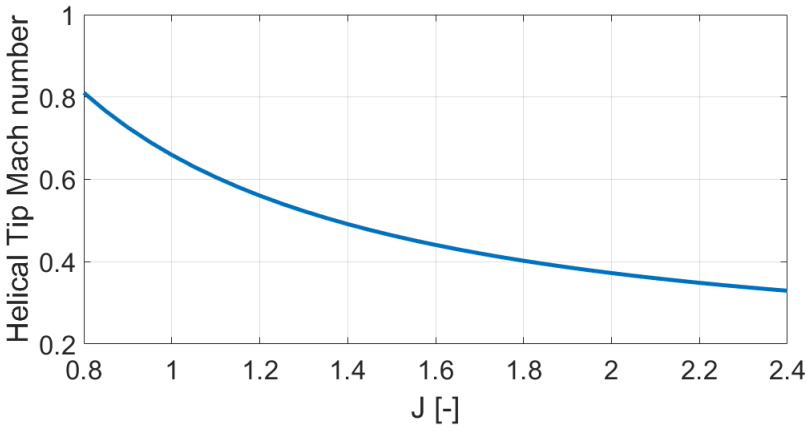

Figure 4.10: Helical tip Mach number as a function of the advance ratio J for $M_x = 0.2$

Finally, in Figure 4.11a and Figure 4.11b the thrust coefficient and power coefficient as a function of the advance ratio are depicted for a tunnel Mach number of 0.34 and $\beta_{0.75} = 53.8\,\mathrm{deg}$. In the linear part of the C_T-graph the results from both the HeliX-tool and MAEPROP show good agreement. For smaller advance ratios the HeliX-tool has trouble finding a converging solution. MAEPROP again shows an

overprediction of the thrust coefficient in this region. The HeliX-tool shows a slightly better agreement with the experimental values compared to MAEPROP for the thrust coefficient. For the power coefficient the HeliX tool shows an overprediction and MAEPROP shows a better agreement.

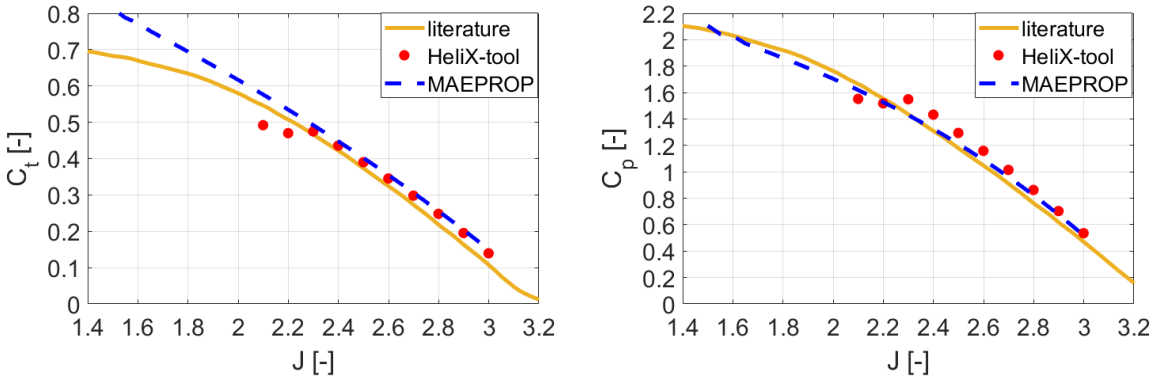

(a) Thrust coefficient as a function of the advance ratio (b) Power coefficient as a function of the advance ratio

Figure 4.11: The thrust and power coefficient for axial Mach number of 0.34 and $\beta_{0.75} = 53.8\,\mathrm{deg}$

In Figure 4.12 the helical tip Mach number is shown as a function of the advance ratio. Here the helical tip Mach number ranges from approximately 0.49 to 0.82 Mach. Just like the previous operating condition, for large helical tip Mach number the deviation increases and the HeliX-tool eventually stops converging.

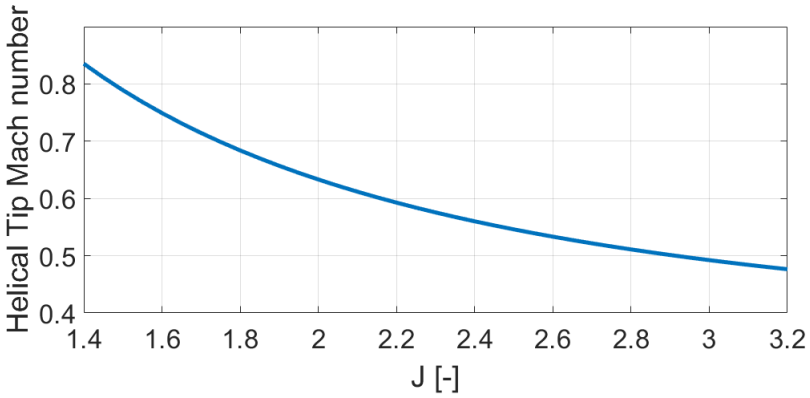

Figure 4.12: Helical tip Mach number as a function of the advance ratio J for $M_x = 0.34$

A further comparison is made between MAEPROP and the HeliX-tool considering the spanwise loading of the propeller blade. It is chosen to generate the spanwise lift distribution for three different tunnel flow Mach numbers and three advance ratios. First the spanwise lift distribution is generated for an axial Mach number of 0.1 and an advance ratio of 1.4. For this operating condition the HeliX-tool computes a thrust coefficient of 0.274 and a power coefficient of 0.517. MAEPROP computes a thrust coefficient of 0.272 and a power coefficient of 0.481. In Figure 4.13 the spanwise lift distribution for this operating condition is depicted. The spanwise lift distribution computed by the HeliX-tool and MAEPROP show good agreement with each other. With an overlapping part in the inner region of the blade where the thicker blade sections are located. At the outer region, more deviations are obtained. This is expected to happen as the blade sections in the outer region consist of very thin airfoils.
For an axial Mach number of 0.2 and an advance ratio of 1.7 the same pattern as the previous condition is obtained as is shown in Figure 4.14. Here the thrust coefficient and the power coefficient computed by the HeliX-tool are 0.417 and 1.00 respectively. Using MAEPROP a thrust coefficient of 0.419 and a power coefficient of 0.925 is computed. Just like the previous operating condition, the thrust coefficients lays close to each other and the spanwise lift distribution shows good agreement.

For the last operating condition, M_x=0.34 and J=2.2, the deviation of both spanwise lift distributions is large. For this condition the thrust and power coefficient are 0.461 and 1.49 for the HeliX-tool. MAEPROP computes a thrust and power coefficient of 0.539 and 1.559 respectively. The deviation between the thrust coefficient is now larger which can be explained by the spanwise lift distribution, recalling that the thrust coefficient is dependent on the lift and drag of the blade. The lift distribution has a big effect on the final thrust coefficient and thus on the performance of the propeller. In the outer region of the blade, the lift computed by the HeliX-tool is lower than that of MAEPROP. As is discussed before, this may be caused by stall. Since MAEPROP does not take this into account, no reduction in lift is observed for this region. As a result the thrust coefficient obtained from the HeliX-tool is smaller than the one obtained from MAEPROP.

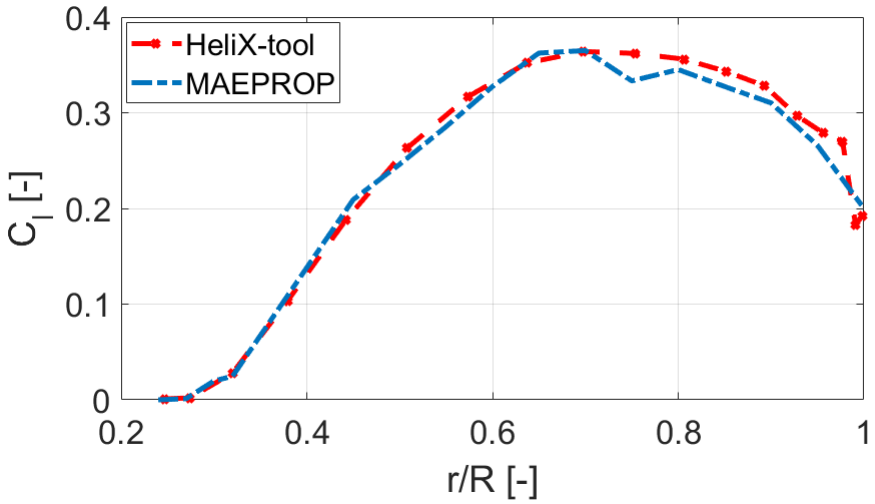

Figure 4.13: Spanwise lift distribution with M_x=0.1, $J = 1.4$ and $\beta_{0.75} = 38\,\mathrm{deg}$

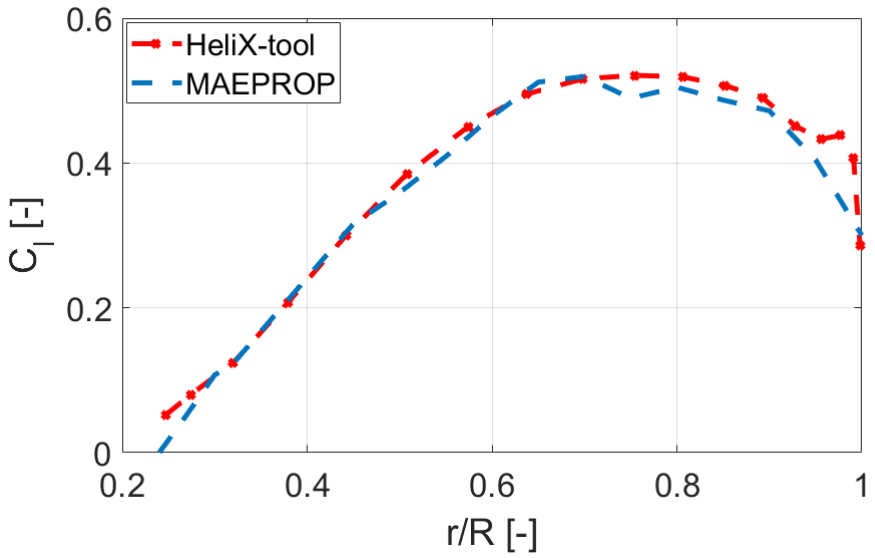

Figure 4.14: Spanwise lift distribution with M_x=0.2, $J = 1.7$ and $\beta_{0.75} = 45.8\,\mathrm{deg}$

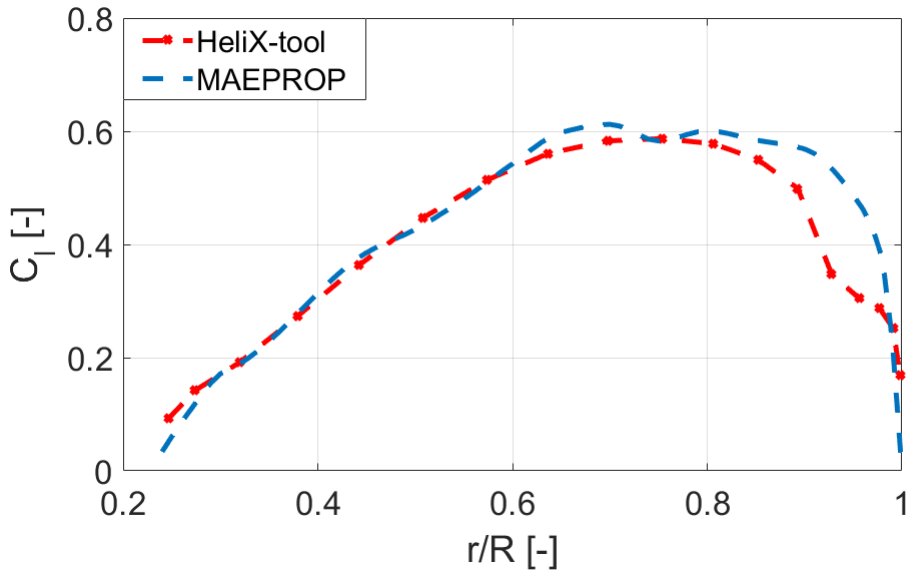

Figure 4.15: Spanwise lift distribution with M_x=0.34, $J = 2.2$ and $\beta_{0.75} = 53.8\,\mathrm{deg}$

Overall, the comparison of the performance results indicates good agreement between the HeliX-tool and MAEPROP except for some regions. MAEPROP computes the performance of the SR-2 propeller using a less detailed description of the geometry of the propeller and does not require to generate 2D aerodynamic data in advance. In total 15 sections are defined in the MAEPROP geometry file which contain the radial position, non-dimensional chord, twist, negative of the zero lift angle, a coefficient for the determination of the moment coefficient, the area of the blade section and x-coordinate of the leading edge. The HeliX-tool uses XRotor to compute the performance of the propeller. For this, 18 blade sections are defined. For these 18 blade sections, XFoil is run for a range of angles of attack in order to be able to run XRotor. The performance results that are obtained from the HeliX-tool show consistency with the experimental values, especially in the linear region of the operating points.

4.3.2. Acoustic results

Now that we have established that the computation of the performance part of the HeliX-tool is showing a good agreement with a different tool and with experimentally obtained performance data, a comparison of the acoustics can be performed. The acoustic results of the HeliX-tool will be compared with literature data and the Rollac-tool. The literature data consists of in-flight measurements and wind tunnel measurements data of the SR-2 propeller. For these the HeliX-tool and the NLR tools are run to see how well they agree. Additionally more comparisons are made between the HeliX-tool and the NLR tools for operating conditions and propeller configurations of interest.

Comparison with in-flight measurements

In [39], in-flight acoustic test measurements are performed and reported. This is done for an 8-bladed SR-2 propeller model with a diameter of 0.622 meters. The measurements are performed at an alititude of 30000 feet or 9144 meters and a temperature of 237 Kelvin. The speed of sound for this condition is 308.6 m/s and the density is equal to $0.4671 kg/m^3$. Only the acoustic results are obtained from these measurements and no performance or aerodynamic data is available.
The SR-2 propeller is mounted on a pylon on top of the fuselage of a Jetstar executive jet. Eight flush microphones are placed on the top of the fuselage in a line directly underneath the propeller axis as can be seen in Figure 4.16. The vertical distance to the closest microphone is 0.812 meters or 2.61R (2.61 times the radius). The array of microphones measures the acoustics for a range of directivity angles of $60\,\mathrm{deg}$ to approximately $130\,\mathrm{deg}$. Since the measurements are performed using 8 microphones, data is available for 8 different angles.

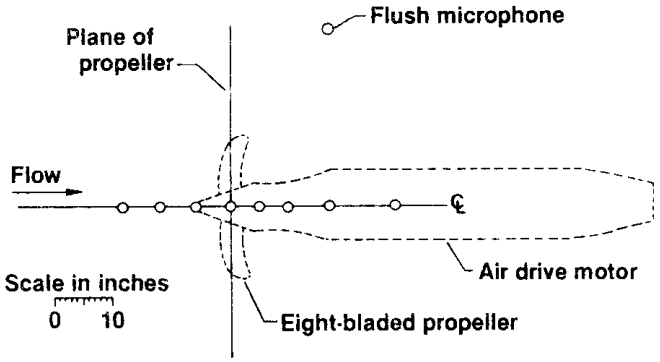

Figure 4.16: Microphone array used in the in-flight measurements [39]

The measurements are taken at several flow mach numbers. The conditions are chosen such that a helical tip Mach number above 1 is avoided. An axial Mach number of 0.71 Mach is used to obtain data for the SR-2 propeller. The operating conditions are than an advance ratio of 3.52, 3.73 and 3.94. These in combination with an axial Mach number of 0.71 results in a helical tip Mach number of 0.95, 0.92 and 0.90 Mach respectively. The blade angles during the test are set between $57\,\mathrm{deg}$ and $60\,\mathrm{deg}$. The data from the measurements are corrected for the presence of a reflected path by adding 6 dB to the computed values which is reported in [40].

No blade aerodynamic data is available for these measurements and therefore it is chosen to compare the propeller performance computed by the HeliX-tool with the values computed by the NLR-tool MAEPROP. These are summarized in table 4.2.

Parameters	HeliX-tool	MAEPROP
Diameter	0.622	0.622
M_x	0.71	0.71
J	3.52	3.52
$\beta_{0.75}$	57	57
number of blades B	8	8
RPM	6005	5997
BPF	800.7	799.5
speed of sound c	308.63	308.63
C_T	-0.1878	0.1267
C_P	1.4031	0.5621

Table 4.2: In-flight measurements performance prediction by the HeliX-tool and MAEPROP

The performance coefficients for the above given operating condition show a large deviation when comparing the HeliX-tool and MAEPROP. The HeliX-tool even gives a negative thrust coefficient. Referring to equation 4.8 and equation 2.7, it can be seen that when the drag increases, the resulting thrust decreases. This is because unlike the NLR-tool, the HeliX-tool computes the spanwise drag of the propeller including a simple drag rise model. The drag rise model increases the drag when the critical Mach number is exceeded. With the current operating conditions high Mach numbers are achieved. The spanwise distribution of the effective Mach number can be seen in Figure 4.17. Recalling that the critical Mach number is assumed to be 0.78 Mach for every blade section of the propeller it is clear that for a great part of the propeller blade the critical Mach number is exceeded. Therefore the drag is increased significantly and even a negative thrust coefficient is obtained. As for the power coefficient, an increase in drag results in an increase of the power coefficient as can be obtained from equation 2.13 and equation 2.14. This means that more power is needed from the engine to rotate the propeller. MAEPROP uses an empirical relation for the estimation of the drag coefficients and these values are much smaller compared to the ones obtained with MAEPROP for the current choice of the critical Mach number.

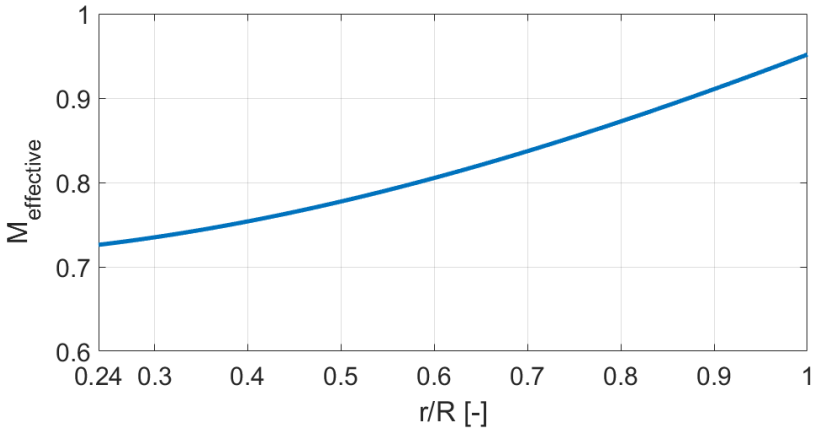

Figure 4.17: Spanwise effective Mach number distribution for M_x=0.71 and J=3.52

In Figure 4.18, the sound pressure level with respect to the angle is computed for an advance ratio of 3.52 and a flow Mach number of 0.71. This is done using Rollac and the HeliX-tool.

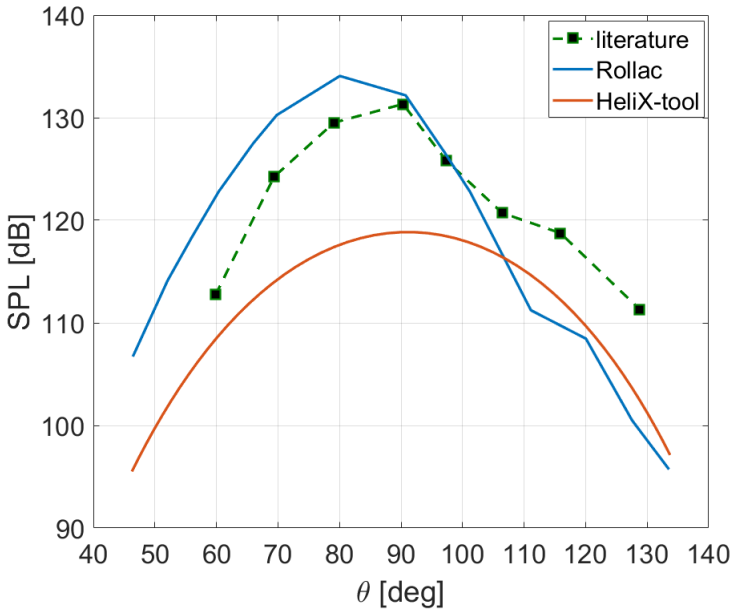

Figure 4.18: SPL with respect to θ, M_x=0.71, J = 3.52, $\beta_{0.75}$= 57 deg, p_{ref} = $2 \cdot 10^{-5}$ Pa

Large deviations are obtained between the predicted SPL values and the SPL values obtained from the in-flight measurements. The directivity pattern obtained with Rollac shows a similar directivity pattern with the experimental results. Higher SPL values are observed in front and at the plane of rotation compared to the SPL values behind the plane of rotation. The results obtained from the HeliX-tool show a more symmetric directivity pattern. With this operating condition, the drag is significant and dominates the lift component of the noise as can be seen in Figure 4.19. As a result the directivity that is obtained shows a symmetric pattern.
The maximum observed SPL determined by the HeliX-tool is at an angle of 90 degrees and is 119 dB. The maximum measured SPL is also at an angle of 90 degrees but has a value of 131.3 dB. The maximum value determined by Rollac is at an angle of 80 degrees and is equal to 134.1 dB. The biggest deviations are observed for the results obtained by the HeliX-tool. These deviations happen due to several reasons. First, the Mach numbers that are observed at the blade section are quite high. These range from 0.72 to 0.95 Mach which is in the transonic region. The HeliX-tool and MAEPROP both use the Prandtl-Glauert compressibility correction, which is valid up to approximately 0.7 Mach. It is a purely subsonic theory and gives odd results at Mach numbers above 0.7. It is based on a linear theory and tends to underpredict the performance for high Mach numbers. A more dedicated correction or high speed wind tunnel tests should be used when these range of flow Mach numbers are present. It is believed that this underprediction is compensated in the MAEPROP tool for this operating condition since it also tends to overpredict the loading as no stall model and no dedicated drag model is taken into account.
Next to an underprediction of the performance, transonic flow also gives rise to non-linear effects. In Figure 2.16 an example of the increase of noise by adding the quadrupole source is given. The non-linear effects can be caused by for example a shock wave being formed on the blade. These can be taken into account by using quadrupole sources. In the current version of the HeliX-tool, this is not implemented and therefore the computed noise spectrum is expected to show an underprediction for operating conditions that result in Mach numbers above 0.7. Note that the NLR-tools also don't take non-linear effects into account.

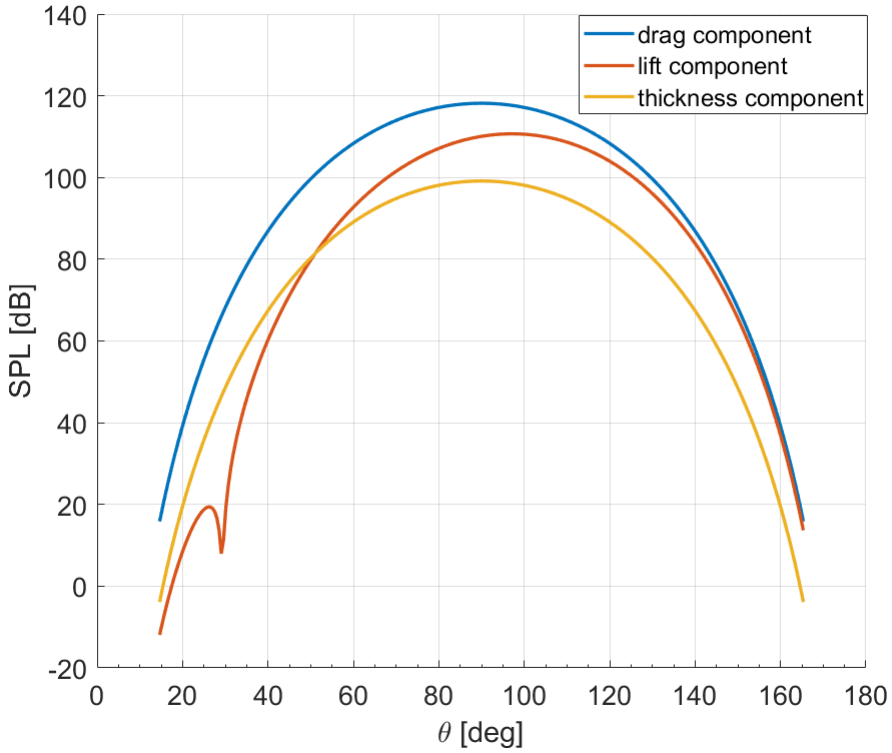

Figure 4.19: Noise components obtained from the HeliX-tool M_x=0.71, J=3.52 and M_{cr}=0.78

In order to better understand the effect of changing the critical Mach number, several noise spectra are generated using different critical Mach number. Also the performance coefficients for these different values of the critical Mach numbers are shown. In table 4.3 the performance coefficients with the corresponding critical Mach number setting is given.

M_{cr}	**0.78**	**0.78**	**0.85**	**0.99**
C_T	-0.1878	-0.4967	0.1093	0.1331
C_P	1.4031	3.4566	0.5755	0.5384
$\beta_{0.75}$	57 deg	60 deg	57 deg	57 deg

Table 4.3: Performance coefficients obtained using HeliX for different set of M_{cr}

The performance coefficients that are obtained show large deviations for different values for the critical Mach number. As is explained before, a negative thrust coefficient can be present when the drag force increases. In reality such a propeller would never be designed as a propeller's main function is to deliver thrust to the aircraft which moves the aircraft forward. It is possible that the computation of the performance by the HeliX-tool is wrong for this condition. However, this can only be known when the performance data for this conditions is known. Furthermore, it can be seen that when the critical Mach number is set to 0.99, the performance coefficients are similar to the ones obtained from MAEPROP. For this condition the maximum Mach number is the helical tip Mach number of approximately 0.95. When the critical Mach number is set to 0.99, the drag rise model is postponed until a Mach number of 0.99 is reached.

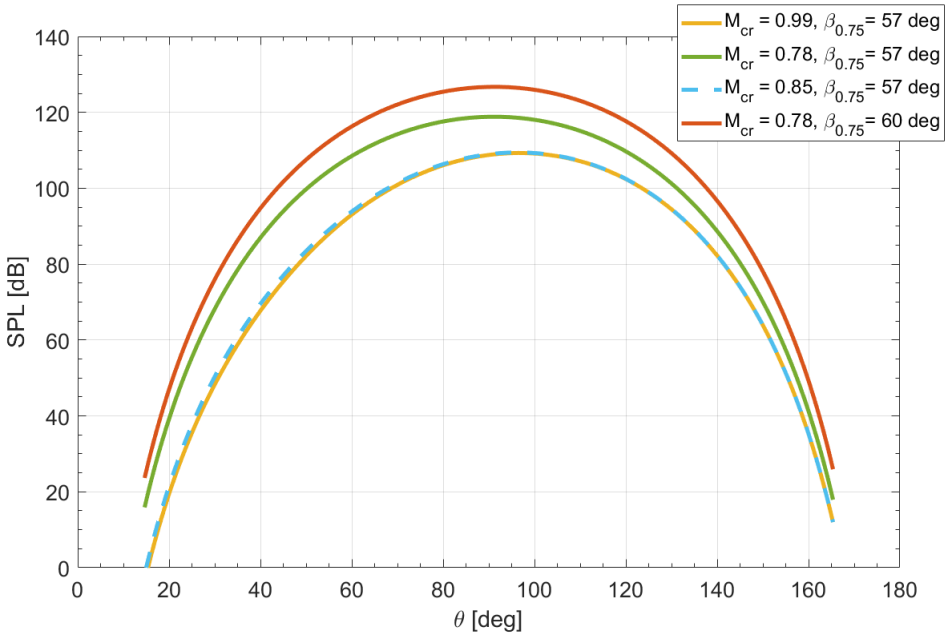

Figure 4.20: Total noise spectrum for different critical Mach number settings and blade angle

In Figure 4.20 the noise obtained for different values of critical Mach numbers is depicted. Additionally a blade angle of 60 degrees is included too. This is done since the in-flight measurements blade angles ranged between 57 degrees and 60 degrees. The condition with a blade angle of 60 degrees and a critical Mach number of 0.78 results in smallest deviation compared to the SPL values of the in-flight measurements as can be seen in Figure 4.20.

At last, the in-flight measurements were performed at a distance of 0.812 meters or 2.61 $\frac{r}{R}$ from the propeller rotational axis. The HeliX-tool is based on a far-field theory. Rollac on the other hand is a near-field theory and can be applied up to approximately $10R$ (10 times the radius). In the far-field the sound pressure is inversely proportional to the distance. In the near-field, the sound pressure varies in a more complex manner with the distance. It is therefore important to check whether the far-field theory is valid for the distance used in the measurements. In [41], it is stated that the far-field theory that is used in the HeliX-tool gives sufficient results up to 0.8D (0.8 times the diameter) tip clearance. This is a distance of 2.60R from the propeller rotational axis. The results that are obtained for the in-flight measurements are right on the border of this. Furthermore, a rule of thumb is often used to see whether one is in the near-field or far-field. An often used definition is that the far-field starts a distance of two wavelengths away from the acoustics source. This wavelength is the wavelength corresponding to the lowest frequency, i.e. the first harmonic or the fundamental frequency. For the current operating condition this is approximately 800 Hz. With the speed of sound for this condition being approximately 308 m/s, the wavelength is then computed to be 0.3855 meters. Using the thumb rule, the far-field starts at a distance of 0.7710 meters away from the center of the propeller at the rotational axis. Hence according to the thumb rule, the far-field starts at approximately 2.33R away from the propeller axis of rotation. Therefore the HeliX-tool should be able to predict the SPL value with a sufficient agreement at this distance. Nevertheless, with such high Mach numbers being present the current version of the HeliX-tool operates in a region where it is not able to incorporate all the noise sources (non-linear effects or other noise sources of the aircraft). In addition, the propeller is not operating in an isolated configuration. Therefore installation effects also play a role in the noise spectra being observed. It is thus chosen to only perform the computation for one operating condition and not to run for the other two operating conditions as a similar result is expected.

Comparison with wind-tunnel data

Acoustic measurements in combination with aerodynamic tests are conducted in the NASA 8-by 6-foot wind tunnel [42]. Noise data are obtained using 6 microphones which are mounted on the wall of the wind tunnel. Figure 4.21 depicts a schematic of the wind tunnel.

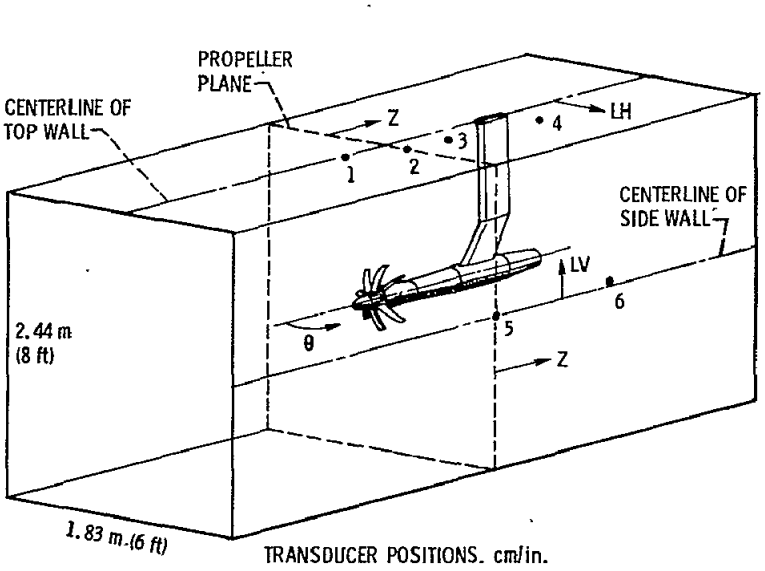

Figure 4.21: Schematic of the NASA 8-by 6-foot wind tunnel [42]

The wind tunnel that is used during the measurements has no acoustic damping or lining and is therefore not ideal. The data is affected by the reflections at the walls of the tunnel. However, when observing the data of the four top wall mounted microphones a directivity of the blade passage tone in the axial direction is obtained. This means that there is a significant difference between the SPL level obtained at for example the first microphone and the third confirming that the effect of the wall reflection is not as severe as initially thought according to the author. Also, the distance effect is observed. Meaning that the microphones at a larger distance to the source result in lower SPL levels compared to the microphones placed closer to the source. Therefore the data is still found to be useful according to the author [42]. The measurements are performed for tunnel flow Mach number ranging from 0.6 to 0.85. Furthermore, different blade settings and advance ratios are used during the measurements. For the performance only the power coefficient is given. No results for the thrust coefficients are given. The operating condition chosen is described in Table 4.4.

M_x	0.6
J	3.06
rpm	6491
M_H	0.863
Number of blades	8
C_P (from measurements)	1.81
$\beta_{0.75}$	60 deg

Table 4.4: First operating condition used from [42]

For the performance only the power coefficient is given which is equal to 1.81 for this operating condition. Using the above given operating condition as input for the HeliX-tool and MAEPROP results in the performance coefficients shown in table 4.7.

Parameters	HeliX-tool	MAEPROP
C_T	0.4348	0.5571
C_P	2.4442	2.1792

Table 4.5: Computed performance coefficients obtained from the HeliX-tool and MAEPROP using data from [42]

The power coefficient is overestimated by both tools when comparing it to the measured power coefficient of 1.81. The agreement with the value obtained using the HeliX-tool is worse than using MAEPROP for this operating condition. The helical tip Mach number is in the transonic region. In this region the linear theory is no longer valid and non-linearity becomes more prominent. The Prandtl-Glauert compressibility correction shows a singularity for Mach numbers close to 1 and is therefore no longer valid. The local lift in MAEPROP is determined using equation 4.1 which is also corrected for compressibility using the Prandt-Glauert rule as is explained before. This shows that both the HeliX-tool and MAEPROP are prone to errors when they are used for operating conditions resulting in high local Mach numbers. Even though the computed performance of the propeller deviates from the measured one, it is still chosen to compute the noise spectrum for this operating condition.

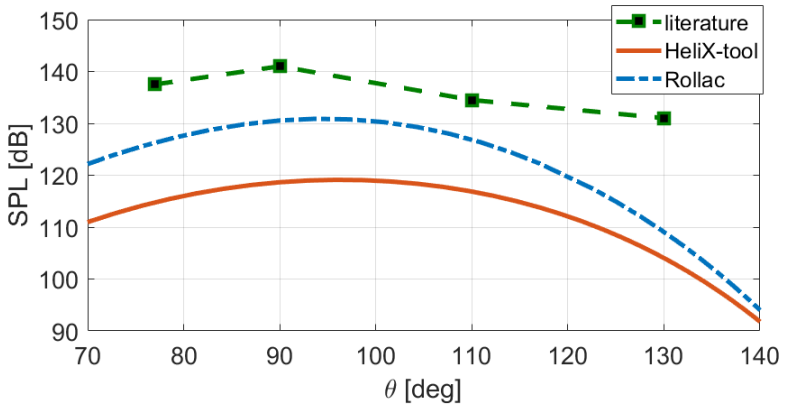

Figure 4.22: The SPL values of the first harmonic as a function of θ with $M_x = 0.6$, $J = 3.06$, $BPF = 865Hz$ and $r = 3.92R$

In Figure 4.22 the sound pressure level is depicted with respect to θ. The measurements are performed at a distance of 3.92R from the propeller axis to the plane where the topwall microphones are located. The values obtained from the literature are the measured data. This measured data is corrected by adding 6 dB due to a miscalibration which is reported in a later publication [40]. The agreement between the computed and measured SPL values is poor. Large discrepancies between the data computed using the HeliX-tool and the data form the literature can be found. At the plane of rotation a deviation of 20 dB is found. The results obtained using the HeliX-tool show large discrepancies for all angles. The maximum SPL value obtained from the HeliX-tool is 119 dB at an angle of 96 degrees. The directivity pattern is similar to the directivity pattern obtained using Rollac. The results obtained using Rollac show better agreement with the measured values but the discrepancies are still considered to be large. At the plane of rotation the computed SPL value is 131 dB approximately. The corrected measured SPL value at the plane of rotation is equal to 141 dB which results in a discrepancy of 10 dB at the plane of rotation.

From the same paper another operating condition is also used. This operating condition is given in Table 4.6.

M_x	0.6
J	2.71
rpm	7295
M_H	0.920
Number of blades	8
C_P (from measurements)	2.33
$\beta_{0.75}$	60 deg

Table 4.6: Second operating condition used from [42]

The power coefficient obtained from the measurements is equal to 2.33 for this operating condition. Using the above given operating condition as input for the HeliX-tool and MAEPROP result in the following performance coefficients.

Parameters	**HeliX-tool**	**MAEPROP**
C_T	0.3817	0.6932
C_P	3.0199	2.601

Table 4.7: Computed performance coefficients obtained from the HeliX-tool and MAEPROP using data from [42]

Again the power coefficient is overestimated by both tools. The agreement with the value obtained using the HeliX-tool is worse than using MAEPROP for this operating condition. The helical tip Mach number for this condition is higher than the previous one. The diference between the computed power coefficient and power coefficient obtained from measurements is approximately 30% for the HeliX-tool and 12% for MAEPROP. The difference can be explained by the drag contribution. The performance coefficient is significanly larger for the HeliX-tool due to the fact that the drag contribution is larger. The drag for the HeliX-tool is determined using a drag model. This drag model takes the critical Mach number into account as is discussed before. With Mach numbers exceeding the critical Mach number a significant increase is obtained. The drag in MAEPROP is determined using a simple empirical relation and is dependent on the lift coefficient only. The obtained drag is significantly smaller compared to the drag obtained using the HeliX-tool. Hence the discrepancy in propeller performance coefficient between the two tools can be significant especially for operating conditions that results in high local Mach numbers.

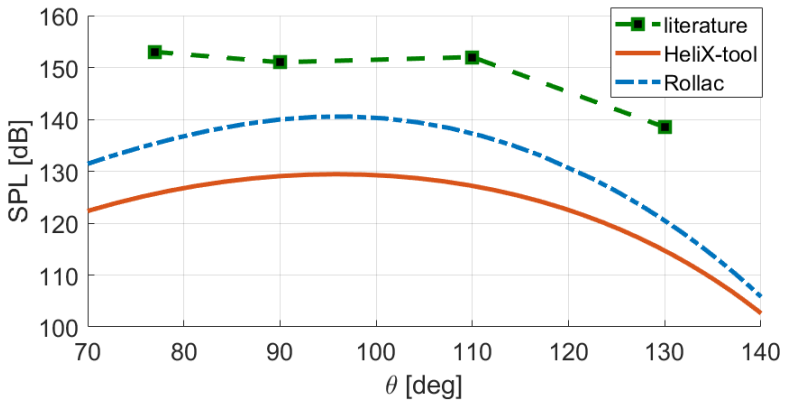

Figure 4.23: The SPL values of the first harmonic as a function of θ with $M_x = 0.6$, $J = 2.71$, $BPF = 977Hz$ and $r = 3.92R$

In Figure 4.23 the SPL is depicted as a function of θ. Again significant difference is obtained between the measured values and the computed values. The difference is found to be larger for this operating condition. Even though the power loading is overpredicted, the SPL values are still lower than the measured values from literature. An overprediction of the propeller performance means a higher loading of

propeller blades. A higher loading results in more noise being emitted. It is therefore suspected that the differences are caused by the fact that the measurements are performed in a wind tunnel which is not treated acoustically. Furthermore, for Mach numbers in the transonic region non-linear sources arise as is explained before. The discrepancy is large and the difference between the measured and computed values is expected to be smaller when including the quadrupole sources for this operating condition.

The difference between the HeliX-tool and Rollac might be explained by Figure 4.24. Here the SPL is depicted as a function of the blade passing harmonic. For the first harmonic the difference between a near-field theory and far-field theory is the most noticeable. After the third harmonic the difference is no longer noticeable. Unfortunately it is unclear for what Mach numbers this plot is generated as no operating condition is given. Nevertheless, the same difference is obtained when comparing the HeliX-tool with Rollac. Rollac is based on a near-field theory while the HeliX-tool is based on a far-field theory as is stated before. Therefore a difference is expected between the two when the noise is computed close to the source (or in the near-field). The plots that are generated in the Figure 4.22 and 4.23 both represent the first harmonic of the noise. Hence the difference is noticeable between the two tools.

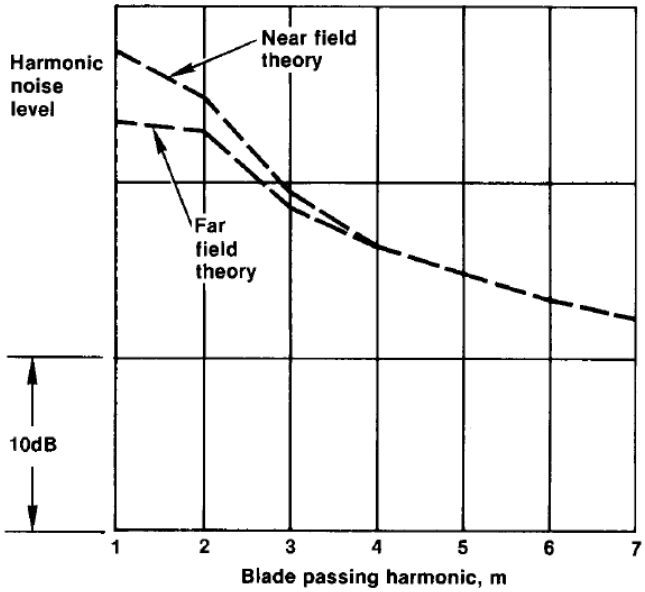

Figure 4.24: Comparison made between a near-field and far-field theory with r=2.6R [43]

In [44] an experimental study is performed on the SR-2 propeller and propeller noise is measured. The measurements are conducted in the NASA Langley 4- by 7- meter tunnel. The tunnel is acoustically treated to reduce the noise of other sources in the wind tunnel. The microphones that are used for the measurements were positioned at a constant vertical distance of 0.889 meters below the propeller centre. In total 11 microphones are positioned on a microphone carriage which is able to move parallel with the propeller centre-line. After each measurement, the carriage is moved to a new position while maintaining the constant vertical distance, hence capturing the propeller noise for a wide range of angles. The test setting is illustrated in Figure 4.25.

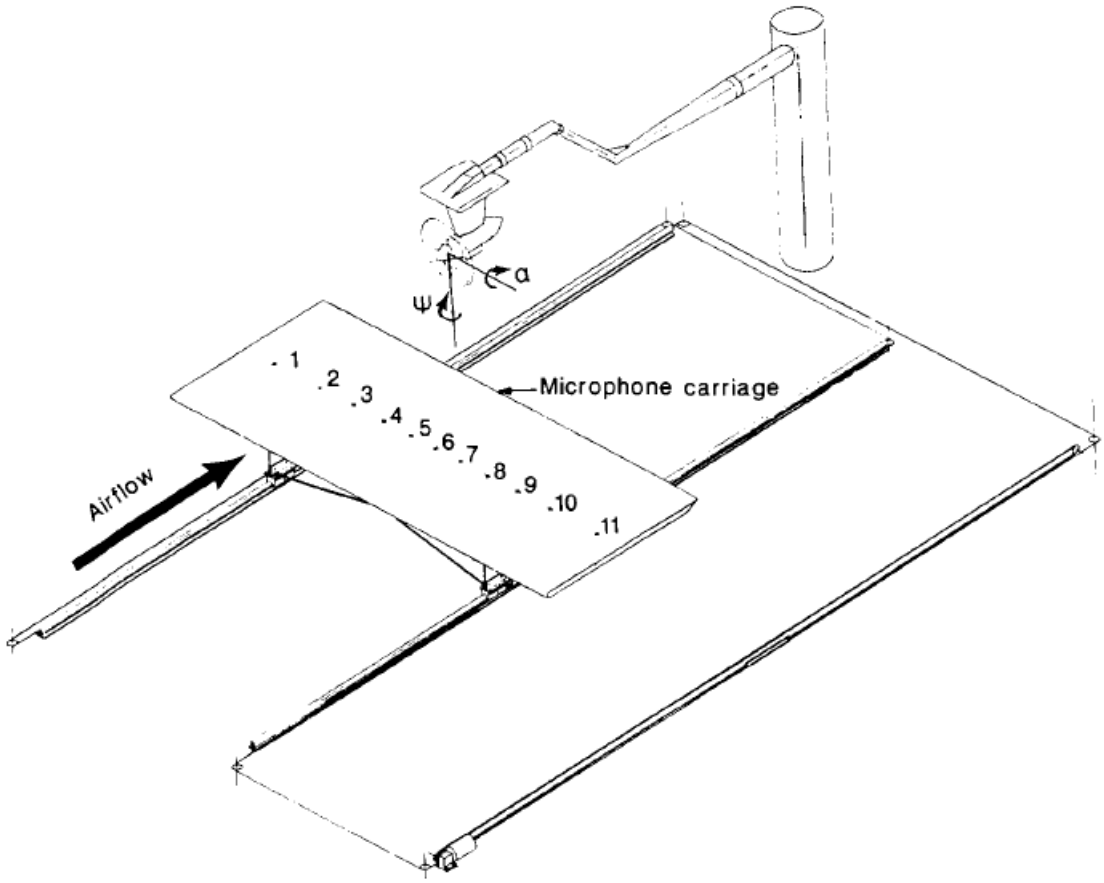

Figure 4.25: Microphone carriage and propeller as is used during the measurements [44]

The measured sound pressure levels are later corrected for free field level conditions by simply subtracting 6 dB. This is done to account for the reflection caused by the hard surface. Therefore making it even more convenient to compare the experimental data with the calculated data from the HeliX-tool and the NRL-tool. Furthermore, the free field levels are normalised for a constant radius of 0.889 meters using the ratio of the distances from the centre of propeller disk.
In this experimental study, a variety of propeller installations are tested. For this comparison study, the propeller with a 4-bladed configuration and a diameter of 0.429 meters is chosen. This is a sting-mounted single rotation propeller. By using data obtained from a sting-mounted propeller, we get as close as possible to a free flying propeller since there are no frames and pylons. A schematic of this sting-mounted propeller can be seen in Figure 4.26.

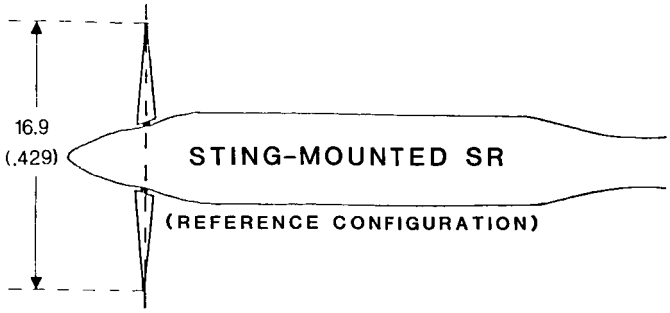

Figure 4.26: Sting mounted single rotation propeller with a diameter of 0.429 meters [44]

The first data set to which a comparison is made has the following test conditions: helical tip Mach number of 0.49, an advance ratio of 0.59 and an axial Mach number of 0.09. The number of revolutions per minute is equal to 7200. The thrust coefficient measured is equal to 0.19 and the blade is set at an angle of $20.6\,\mathrm{deg}$ at 0.75 $\frac{r}{R}$. Two theoretical predictions are performed. One is done using the NLR tools and the other one is done using the HeliX-tool. In Figure 4.27 the OSPL with respect to θ is depicted.

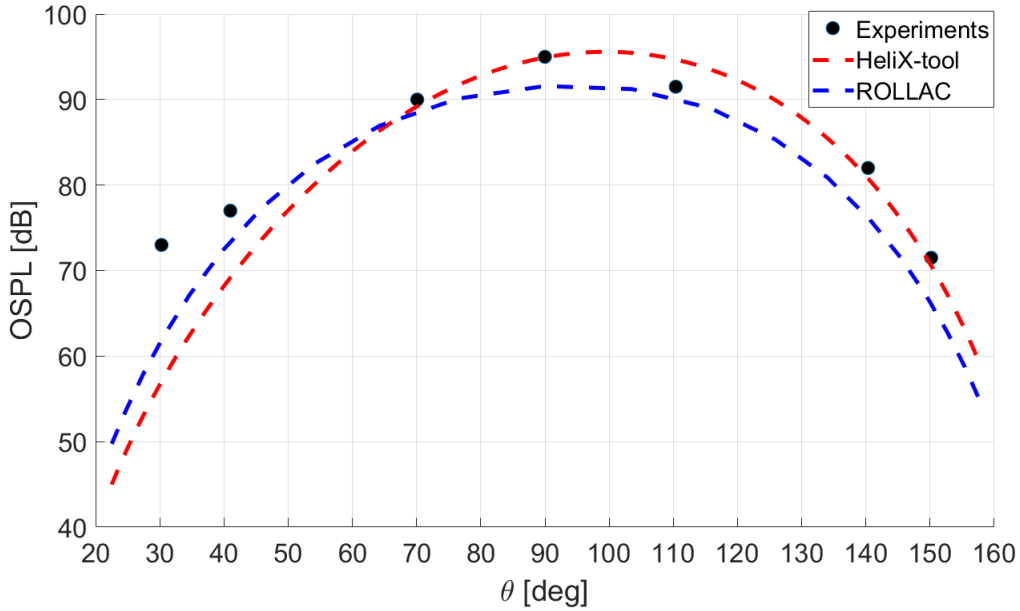

Figure 4.27: Overall Sound pressure level in dB as a function of θ, $p_{ref} = 2 \cdot 10^{-5}$ Pa, J=0.592, Mx=0.09, r=0.889 meter, $\beta_{0.75} = 20.6\,\mathrm{deg}$

The thrust coefficient C_T which is measured during the experiments is 0.19. The thrust coefficient is also calculated by MAEPROP and is equal to 0.1222. This is quite a large discrepancy. The thrust coefficient that is determined by the HeliX-tool is equal to 0.163 which is more close to the value measured during the experiments. The agreement of the acoustic results calculated with the HeliX-tool and the experimental data for angles ranging from $70\,\mathrm{deg}$-$150\,\mathrm{deg}$ is good. Compared to the results obtained using the NLR-tool, the HeliX-tool shows better results. However, for small observer angles the NLR-tool shows smaller deviations with the experimental data compared to the HeliX-tool. From the experimental data it can be seen that the maximum OSPL-value is obtained at the plane of rotation (θ=$90\,\mathrm{deg}$). In the plane of rotation, the predicted OSPL-value by the HeliX-tool shows almost no deviation and is equal to 94.9dB compared to an OSPL-value of 95dB obtained from the experimental data. The OSPL-value in the plane of rotation by Rollac is 91.5dB which is a deviation of 3.5dB. The smaller OSPL-value may be due to the fact that the performance (loading) is underpredicted. The acoustic

results obtained by Rollac show a maximum OSPL-value at the plane of rotation while the HeliX-tool shows a maximum OSPL-value aft the plane of rotation at a directivity angle of approximately $100\,\mathrm{deg}$. The reason for this can be explained by Figure 4.28.

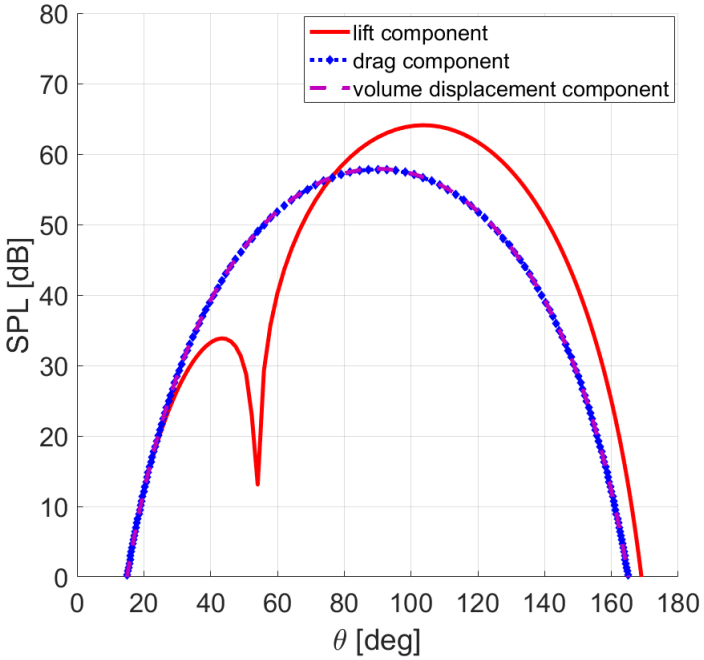

Figure 4.28: Sound pressure level in dB as a function θ for the several noise components calculated with the HeliX-tool, $p_{ref} = 2 \cdot 10^{-5}$ Pa, J=0.592, Mx=0.09, r = 0.889 meter, 1xBPF.

In Figure 4.28, the SPL for different angles is shown. The SPL-values depicted are the maximum obtained SPL values for the first harmonic which has a BPF of approximately 482 Hz. When looking at the drag component of the loading noise and the volume displacement component little difference in SPL-values is obtained when comparing them with each other. Furthermore, it can be noted that at a directivity angle of $90\,\mathrm{deg}$ the drag and volume displacement component appear to have a maximum which is as expected. For the lift component of the loading noise a different radiation pattern is obtained. There appears to be a node at approximately $54\,\mathrm{deg}$. The lift component is a dipole and therefore should have a two-lobe directivity pattern. In equation 3.10, the non-dimensional wavenumber is given which is only used for the lift dipole. The numerator of this equation is $M_r^2 cos\theta$-M_x where M_r is the section Mach number and M_x is the axial Mach number. For a blade element the node is located at an angle given by $M_r^2 cos\theta$-M_x=0. Therefore, the angle at which the node is present only depends on the rotational speed and axial speed. Thus when the lift component of the noise is the dominant one (like in this case), the maximum obtained SPL value depends on the operating condition which defines the rotational speed and the axial speed.

From the same experiments another operating condition is chosen for which acoustic data is generated. The test conditions are as follows: helical tip Mach number of 0.67, an advance ratio of 0.42 and an axial Mach number of 0.09. The number of revolutions per minute is equal to 10,080. The thrust coefficient measured is equal to 0.06 and the blade is set at an angle of $12.7\,\mathrm{deg}$ at 0.75 $\frac{r}{R}$. In Figure 4.29 the SPL with respect to θ is depicted for the first harmonic. The reason for choosing the first harmonic is that it is the fundamental frequency and thus contains the highest values for SPL.

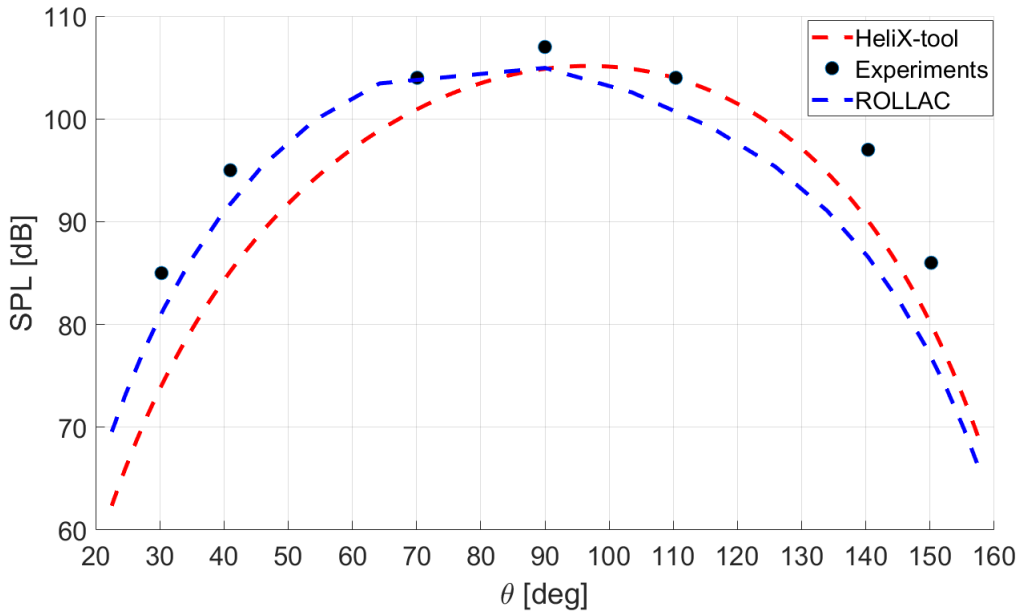

Figure 4.29: Sound pressure level in dB as a function of θ, p_{ref} = 2e-5, J=0.423, Mx=0.09, harmonic number = 1 (1xBPF), r = 0.889 meter.

The thrust coefficient determined by the HeliX-tool is 0.062. The NLR-tool calculated a thrust coefficient of 0.055 which is a slightly smaller value than the experimentally determined thrust coefficient of 0.06. The acoustic results of the NLR-tool are close to the results of the HeliX-tool in terms of the maximum SPL value achieved. The SPL value in the plane of rotation is almost the same with 104.9 dB for the HeliX-tool and 104.8 dB for the NLR-tool. The value for the SPL in the plane of rotation obtained from experiments is equal to 107 dB. This is a deviation of approximately 2 dB. For the deviations that are obtained at larger or smaller angles, an explanation is given by [44]. According to [44], unsteady loading which is caused by the tunnel free-stream turbulence and unsteadiness due to variations in blade setting and spacing may cause additional noise sources. In the HeliX-tool the unsteady loading has not been taken into account. Therefore, an under prediction of the SPL can occur. The HeliX-tool shows a slightly better agreement with the data for larger angles. However Rollac has smaller deviations between the computed and experimentally determined SPL-values for the smaller angles at this condition.
Figure 4.30 shows the three noise components as predicted by the HeliX-tool.

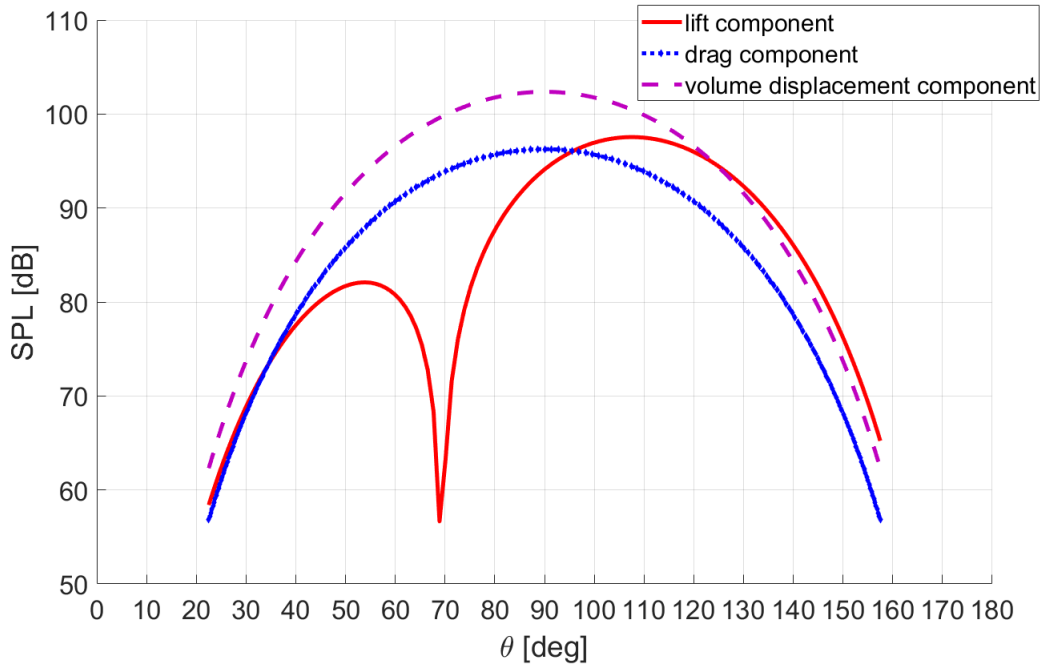

Figure 4.30: Sound pressure level in dB as a function of θ, p_{ref} = 2e-5, J=0.423, M_x=0.09, harmonic number = 1 (1xBPF), r = 0.889 meter as is predicted by the HeliX-tool

Again a two-lobe directivity pattern is obtained for the lift component of the loading noise. Now the node is at an angle of approximately $69\,\mathrm{deg}$. This test condition has a larger rotational speed compared to the previous test condition as the advance ratio is smaller. An increase in rotational speed results in an increase in the noise generated by the volume displacement component. This results in the volume displacement component to be the dominant component in this condition. The volume displacement component of the noise is not directly dependent on the performance prediction of the propeller as it does not require variables like the C_l and C_d. Overall the agreement between Rollac and the HeliX-tool is good and consistent in the sense that the HeliX-tool shows larger values for SPL aft the plane of rotation and shows smaller values for the SPL in front of the plane of rotation. When comparing the computed acoustic result with the measured ones from the experiments, again the data points obtained near the plane of rotation show a better agreement.

In another study wind tunnel measurements in the Acoustic Research Tunnel at the United Technologies Research Center (UTRC) are performed and reported in [45] and [46]. In this study several NASA propeller models are compared to each other. One of the propeller models is the SR2 propeller. Near-field and far-field measurements are present for different operating conditions. The tests performed at the UTRC consist of high speeds for which Mach 1 is exceeded at the blade tip that simulate the cruise condition of this particular propeller and lower speeds which simulate take-off and landing conditions. For both conditions, the near and far-field SPL are measured. The far-field microphones cover the angles ranging from $60\,\mathrm{deg}$ to $120\,\mathrm{deg}$.

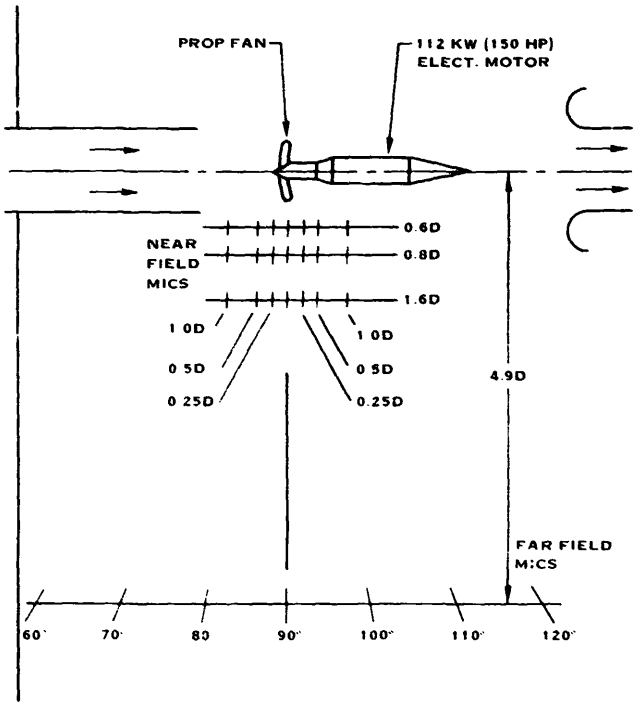

Figure 4.31: Microphone locations of the measurements performed by Brooks [45]

The power required to rotate the eight blades of the SR2 propeller is 354 kW for the 0.622 meters diameter model. For the test it is determined that 22 to 45 kW per blade is required to simulate the operating conditions of interest. An electric motor is used to deliver the power for the rotation of the blades. However this has an available power input of 112 kW. Hence a two-bladed and a four-bladed SR2 model with a diameter of 0.622 meters are used for the different operating conditions and measurements. These are then used to simulate eight-bladed propeller operation. This is done by measuring the 8P harmonic levels. This is the blade passage tone of a symmetrical eight-bladed propeller or prop-fan as it has a frequency of 8 per revolution. Essentially this means that the 4th harmonic of a two-bladed propeller is used which has the same frequency as the first harmonic of an eight bladed propeller. Furthermore, a correction for the number of blades is applied using the ratio of the number of blades. The two-bladed or four-bladed propeller are also set in such a way that they represent the loading that would occur at one blade when having an eight-bladed propeller. The only difference left is the number of blades. For this a correction can be applied. In terms of SPL this means adding 12 dB to the 8P harmonic from the two-bladed propeller and multiples of this harmonic. This is determined from the ratio of the number of blades. The ratio of the number of blades is 4 when comparing a two-bladed propeller and an eight-bladed propeller. When taking 20 times the logarithm to the base 10 of the ratio of the number of blades, the correction for the SPL is obtained to account for the difference of blade number which is 12 dB. The same method is applied when data of a four-bladed propeller is computed but with a different ratio of the number of blades. This principle is known as linear superposition and can be used when comparing propellers with different number of blades but with similar helical tip Mach number and loading [45].

Besides the power being a limiting factor, the windtunnel can also only achieve a maximum flow Mach number of 0.32. Cruise condition blade loading is achieved by overspeeding the propellers. The windtunnel used during the measurements reported in [45] is an open-jet wind tunnel in an anechoic chamber. The open-jet wind tunnel consists of a nozzle which is set into the wall of the anechoic chamber. A jet is than formed between the nozzle and the collector which is located downstream of the propeller. No flow is present outside the jet. This gives rise to a shear layer between the jet flow and the quiescent air surrounding the jet flow. Since the microphones that measure the sound are located outside of the jet, a correction is applied to account for the shear layer. Due to the shear layer the sound is refracted and also the amplitude is adjusted. The data that is used from the literature is the corrected data. The effect of the shear layer is not taken into account in the predictions made with the HeliX-tool and Rollac. However, the corrected microphone positions are used during the predicitons which is depicted in Figure 4.32. Finally the SR-2 propeller was located completely in the jet potential core and therefore no interaction is present between the propeller and the shear layer [46].

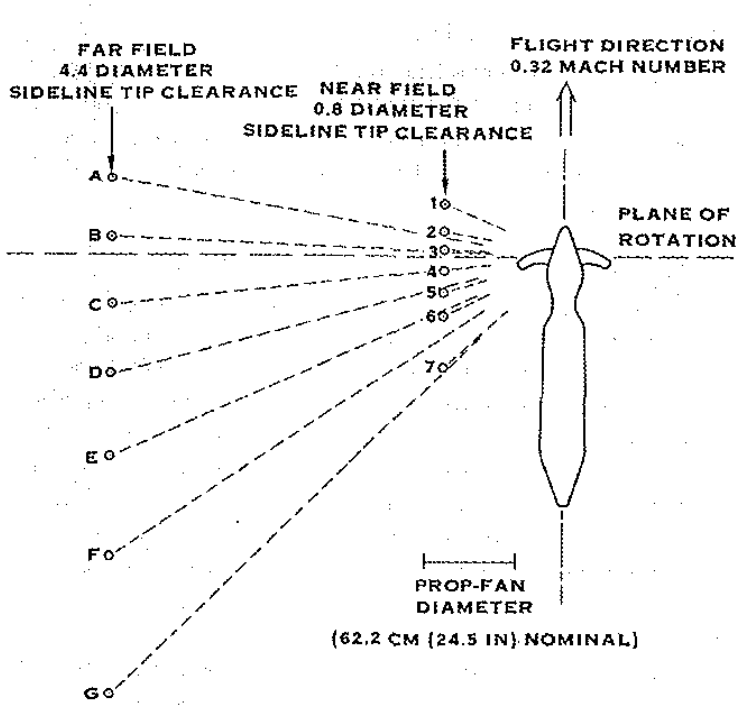

Figure 4.32: Corrected microphone positions for the near-field and far-field [45]

The data presented in [45] consists of the number of blades used, helical tip Mach number, rpm, the tunnel flow Mach number and the power loading per blade. No data regarding the blade pitch angles is given. Therefore the blade pitch angle that yielded the given power loading per blade is used as input for the performance computation. The HeliX-tool which uses XRotor for the computation of propeller performance allows to give the power needed as input and computes the resulting blade pitch angle using this input. This option is used to determine the blade pitch angle. The determined blade pitch angle is than also used as input for MAEPROP to compute the performance of the propeller. In this way a fair comparison can be made between the results of the NLR-tool and the HeliX-tool.

The operating condtions of the first dataset used for comparison are depicted in Table 4.8

M_x	0.203
rpm	6420
M_H	0.664
Number of blades	2
Power per blade	12.9 kW

Table 4.8: Operating condition of the first dataset chosen from [45]

As is stated before, the power per blade can be used as input in the HeliX-tool. This is done in order to obtain the performance data. Using the above parameters as input in the HeliX-tool the following performance data is obtained from the HeliX-tool.

C_P	0.185
C_T	0.118
$\beta_{0.75}$	32.8 deg
J	1.05

Table 4.9: Performance coefficients and blade angle obtained from the HeliX-tool

The blade angle that is obtained from the HeliX-tool is used as input in the NLR tool MAEPROP. The performance data that are then obtained are shown in Table 4.13.

C_P	0.164
C_T	0.126

Table 4.10: Performance coefficients obtained from MAEPROP

A deviation between the performance coefficients is found using the HeliX-tool and MAEPROP. This is rather small in terms of performance coefficients but when checking the spanwise lift distribution the difference is quite large as is depicted in Figure 4.33. The spanwise loading distribution or the performance coefficients are both not given in the literature and it is therefore difficult to state which one is closer to the real spanwise loading. Note that the spanwise lift distribution is not identical for this operating condition but when comparing both distributions with each other it can be seen that the integrated spanwise lift coefficient is quite similar.

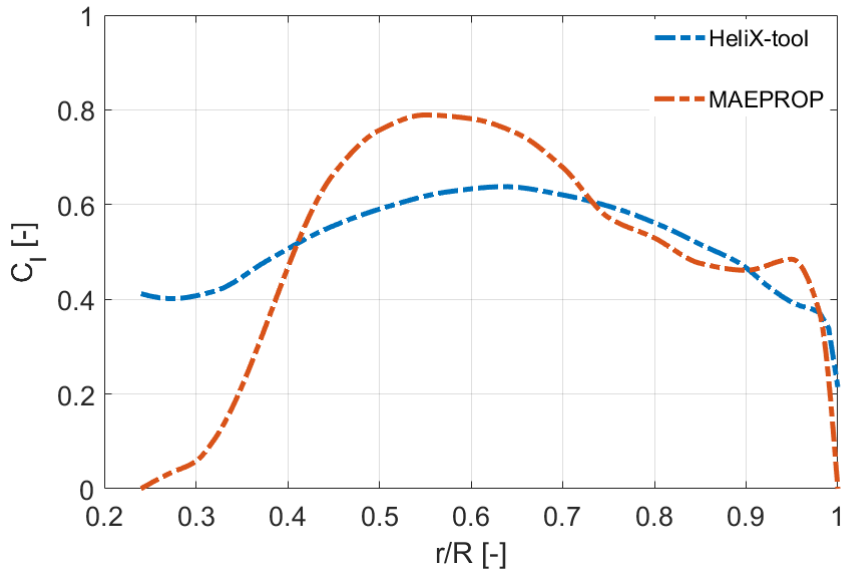

Figure 4.33: Spanwise lift distribution for M_x=0.203, $\beta_{0.75}$=32.8 deg and J=1.05

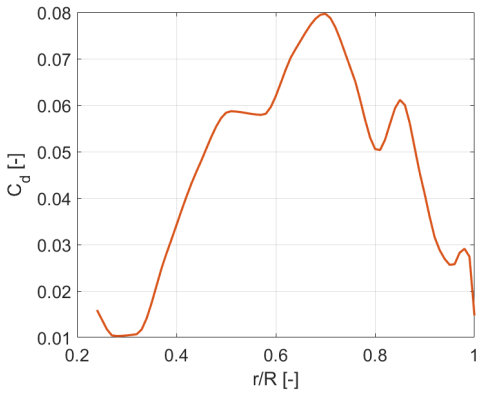

(a) Spanwise drag distribution obtained from the HeliX-tool

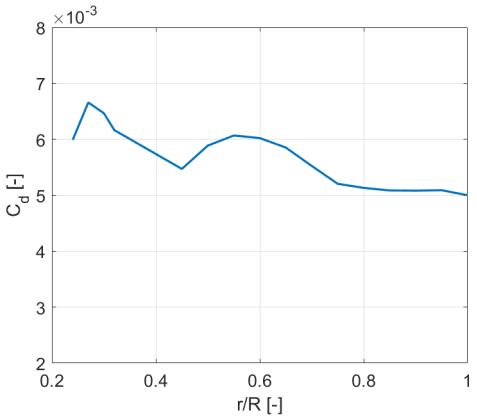

(b) Spanwise drag distribution form MAEPROP

Figure 4.34: Spanwise drag distribution for M_x=0.203, $\beta_{0.75}$=32.8 deg and J=1.05

Besides lift, drag also has a contribution in determining the performance coefficients. The spanwise drag distribution is shown in Figure 4.34. The drag coefficients that are obtained from the HeliX-tool are larger than the ones obtained from MAEPROP. As a result the power coefficient that is obtained using the HeliX-tool is larger than that of MAEPROP since more power is needed to rotate the propeller. Also, the netto thrust is smaller due to this additional drag which results in a lower thrust coefficient being obtained using the HeliX-tool for this operating condition. This can be explained by the fact that drag is estimated using a simple empirical relation in MAEPROP which depends on the local lift coefficient. In the HeliX-tool the drag coefficient is computed as a function of the effective Mach number, Reynolds number and the local angle of attack.

Even though there are some deviations between the performance of the propeller obtained from the HeliX-tool and MAEPROP, it is chosen to perform the noise computations with the current values obtained for the performance. The noise data that is obtained from [45] is measured in the near field at 0.8D (0.8 times the diameter) measured from the tip. This is the same as 2.6R (2.6 times the radius) from the propeller axis of rotation. From the literature it is known that this is in the near-field. In Figure 4.35 the SPL is depicted as a function of θ.

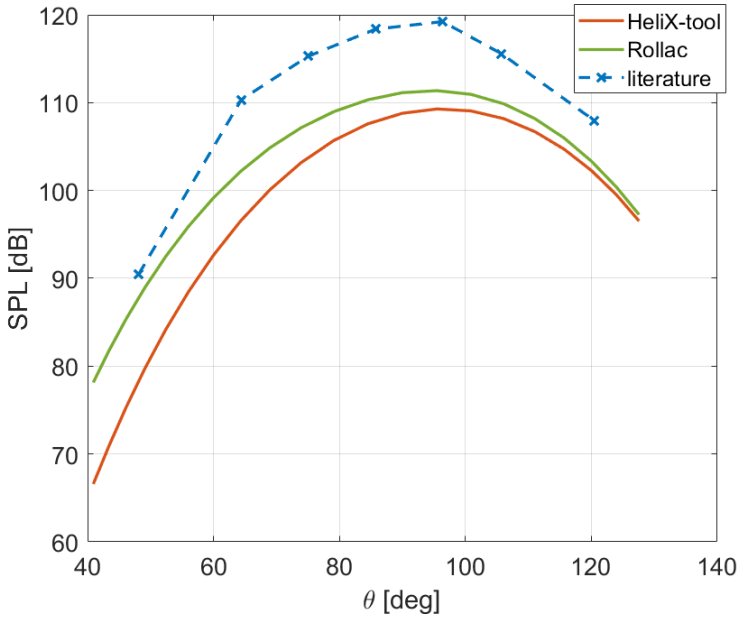

Figure 4.35: SPL in dB as a function of θ, p_{ref} = 2e-5, M_x=0.203, $\beta_{0.75}$=32.8 deg, J=1.05, BPF = 213 Hz and r=2.6R

It can be seen that the directivitty pattern obtained from the HeliX-tool and Rollac show good agreement with the directivity of the measurement data. Overall, a large underprediction of the SPL is obtained when comparing the predicted values of Rollac and the HeliX-tool with the literature data. No explanation for this is found. It could be due to a misunderstanding of the data. It is difficult to state what the reason for this deviation is as no blade pitch angle is given and performance data is lacking. The agreement between Rollac and the HeliX-tool on the other side is quite good. It also shows that even though the HeliX-tool is based on a far-field theory, sufficient agreement can be found in the near-field when comparing it to Rollac for this operating condition.

Another comparison is performed in the near-field but for a different operating condition. The operating condition is given in Table 4.11.

M_x	0.32
rpm	7059
M_H	0.741
Number of blades	2
Power per blade	23.1 kW

Table 4.11: Operating condition of the second dataset chosen from [45]

The same method is used as with the previous operating condition and the blade pitch angle is obtained from the HeliX-tool. The performance coefficients and the blade pitch angle that yields in the given power loading are given in Table 4.12.

C_P	0.247
C_T	0.119
$\beta_{0.75}$	40.3 deg
J	1.50

Table 4.12: Performance coefficients and blade angle obtained from the HeliX-tool for the second operating condition

By using the blade pitch angle obtained from the HeliX-tool as input for MAEPROP, the following performance coefficients are obtained:

C_P	0.222
C_T	0.123

Table 4.13: Performance coefficients obtained from MAEPROP for the second operating condition

Again, there is a small deviation between the performance coefficients obtained from MAEPROP and the HeliX-tool. The power coefficient obtained using MAEPROP is smaller than that the one obtained from the HeliX-tool. Vice versa, the thrust coefficient obtained from MAEPROP is larger than the one obtained from the HeliX-tool. This seems to be a recurring pattern and is also observed when running for other operating conditions. The spanwise lift distribution obtained from both tools are now closer to each other than the previous operating condition as is depicted in Figure 4.36.

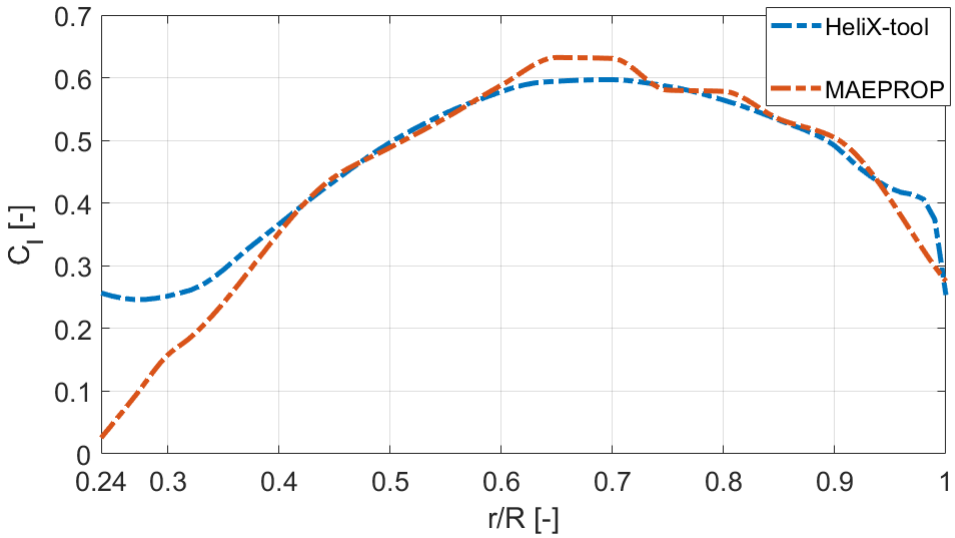

Figure 4.36: Spanwise lift distribution for M_x=0.32, $\beta_{0.75}$=40.3 deg and J=1.50

For this operating condition noise data is available in the far-field. The SPL values are computed using the HeliX-tool and Rollac. The results of this are depicted in Figure 4.37.

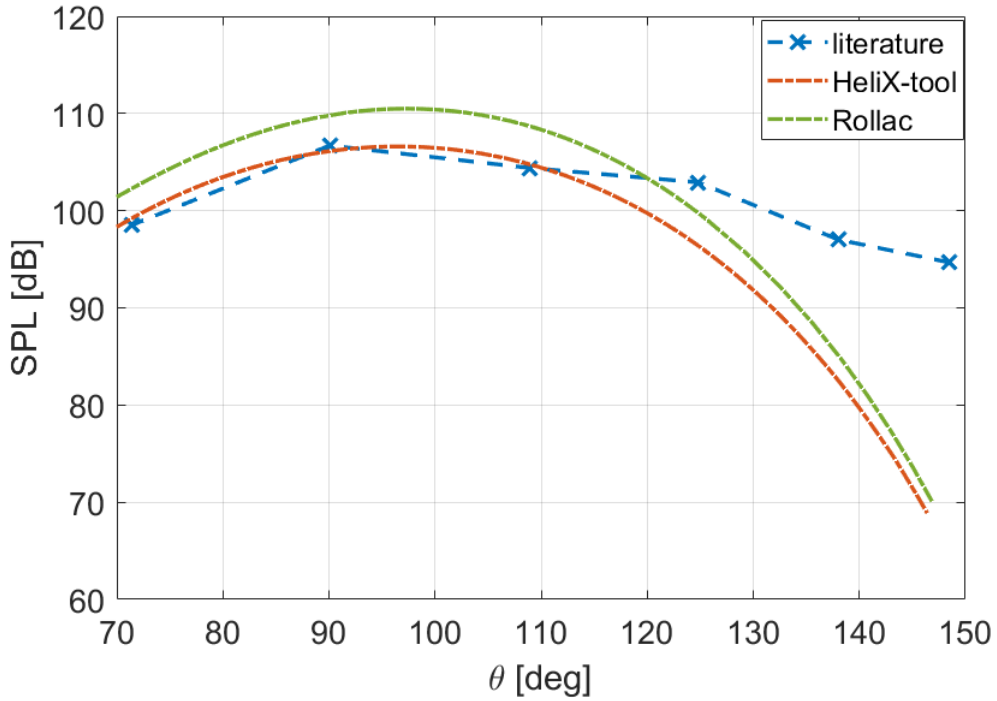

Figure 4.37: SPL in dB as a function of θ, p_{ref} = 2e-5, M_x=0.32, $\beta_{0.75}$=40.3 deg, J=1.50, BPF = 235 Hz and r=9.8R

For this operating condition Rollac seems to overpredict the SPL values near the plane of rotation compared to the values obtained from literature. A better agreement near the plane of rotation is found using the HeliX-tool. Here the differences are smaller between the measured values and the values obtained using the HeliX-tool. Overall the differences between Rollac and the HeliX-tool are around 4-5 dB at most in terms of SPL. At the plane of rotation the SPL value is measured to be approximately 106.7 dB. The HeliX-tool computes a value of 106.1 dB resulting in a deviation of 0.6

dB. The value computed using Rollac is 110 dB and therefore a overprediction of 3.3 dB is present at this directivity angle. For large directivity angles the deviation between the measured values and the computed values increases for both the HeliX-tool as well as for Rollac. Initially it was thought that the presence of background noise could explain this. However, the levels of the background noise are low compared to the measured values as can be seen in Figure 4.38. The measurement of the background noise is performed using a hub with no blades and setting the rpm at 12000. This is a rpm setting different than the current operating condition. However, a lower rpm setting would result in less background noise. Therefore the data presented in Figure 4.38 is useful. No explanation has been found for the differences obtained at large directivity angles.

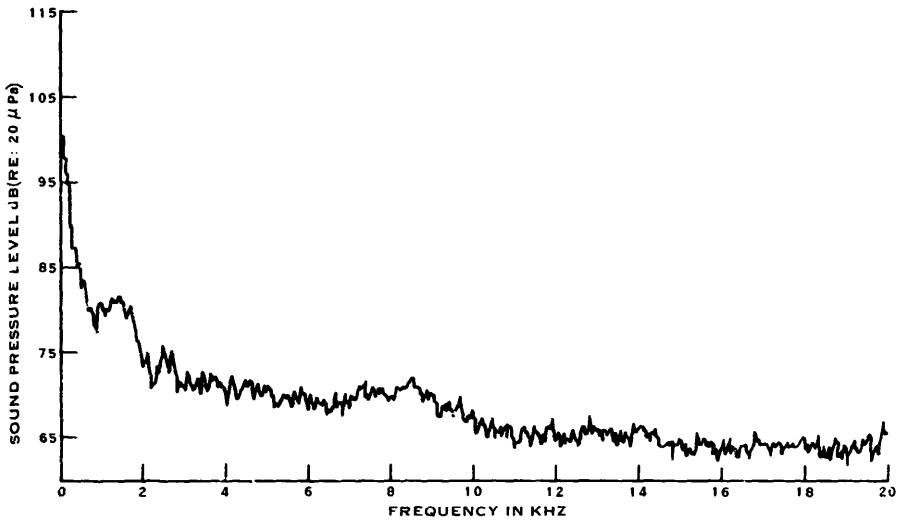

Figure 4.38: Background noise measured in the far-field at a flow Mach number 0.32

Additional comparison made with the NLR tools

In this section additional comparisons are made for operating conditions and design parameters different than is discussed so far. The operating condition is chosen such that non-linear sources are kept to a minimum. Hence, the helical tip Mach number is kept below a Mach number of 0.7.

The first design parameter that is evaluated in this section is the number of blades. The operating condition considered for this is as follows

M_x	0.5
J	3.3
M_H	0.69
$\beta_{0.75}$	59 deg

Table 4.14: Operating condition used in the additional comparison between the HeliX-tool and the NLR-tools

Changing the number of blades for a given thrust requirement can be beneficial in reducing the loading noise. For a constant thrust setting, the increase in the number of blades results in a lower loading per blade hence reducing the loading noise. However, an increase in the number of blades also means that a larger total blade volume is present and thus an increase in thickness noise is expected. Furthermore, a larger number of blades also result in higher blade passage frequencies being observed. In order to see what the effect of changing the number of blades is, it is chosen to perform an analysis and comparison using the SR-2 propeller with a two-bladed and four-bladed configuration. These are used in the NLR tools and the HeliX-tool and a comparison is made.

First the performances of both propeller configurations are computed using MAEPROP and the HeliX-tool. The thrust value that is obtained from the two-bladed configuration is used as the thrust requirement. It is therefore necessary to change the blade pitch angle of the four-bladed configuration in order to maintain the same value for the thrust. In Table 4.15 the performance coefficients are given which are obtained using the operating condition described in Table 4.14. Also the blade pitch angles are given that result in the assumed thrust setting.

	HeliX		**MAEPROP**	
number of blades B	2	4	2	4
C_T [-]	0.1236	0.1236	0.1236	0.1236
C_P [-]	0.5111	0.4688	0.4700	0.4631
$\mathrm{B}_{0.75}$ [deg]	59	56.62	59	56.66
BPF	167	334	167	334

Table 4.15: Performance coefficients and blade angle of the two different propeller configurations

Overall a good agreement is found between the two tools for the performance coefficients of the different propeller configurations. An interesting finding is that the power coefficient is slightly decreased when going from a two-bladed configuration to a four-bladed configuration. This is caused by the reduction of the loading of the blades and possibly also the adjustment of blade angle.
In Figure 4.39 the spanwise lift distribution obtained from MAEPROP and HeliX is depicted for both propeller configurations. It can be seen that the local lift coefficients are reduced for the four-bladed SR-2 propeller with respect to the two-bladed configuration. This is as expected and indicates that the blade loading is significantly reduced. The difference in spanwise lift distribution between the two tools is most prominent at the root of the propeller. Near the tip the agreement between both tools becomes better. Of course the blade loading does not only depend on the lift but also on the drag. However, the lift is significantly larger than the drag and therefore it is sufficient to only depict the propeller lift distribution. Furthermore, the operating condition that is used avoids additional drag sources due to exceeding the critical Mach number. The helical tip Mach number is 0.69 so no additional drag is expected for this condition.

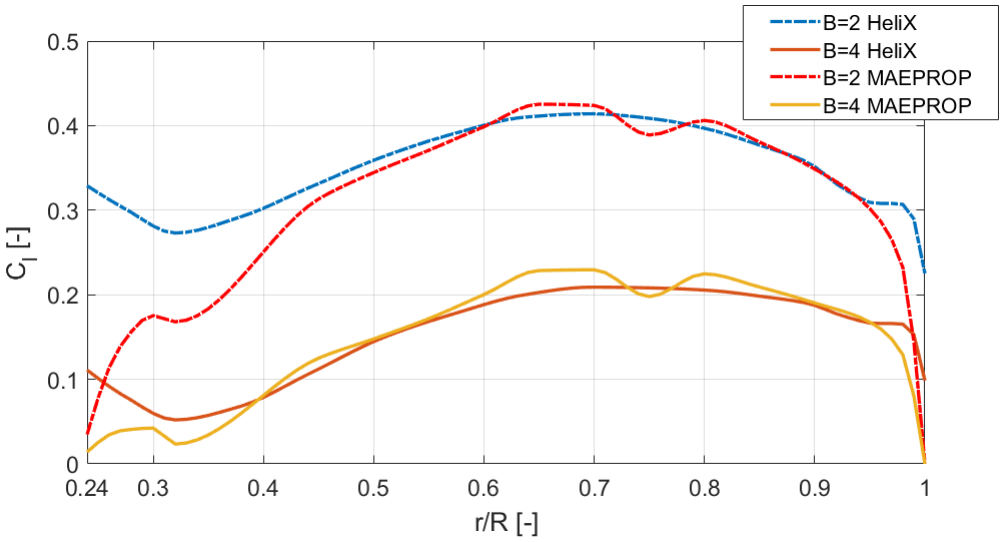

Figure 4.39: Spanwise lift distribution for the two propeller with different number of blades as is computed using HeliX and MAEPROP

In Figure 4.40 a polar plot is depicted showing the SPL as a function of the directivity angle θ. A good agreement can be found between both tools. It can also be seen that the noise is significantly reduced when increasing the number of blades from two to four for this operating condition. As is explained before, this is due to a reduction of the loading per blade and hence the loading noise. On the other side the noise could be increased as an increase in the number of blades can raise thickness noise. The net effect in this case however is that the overall noise is reduced.

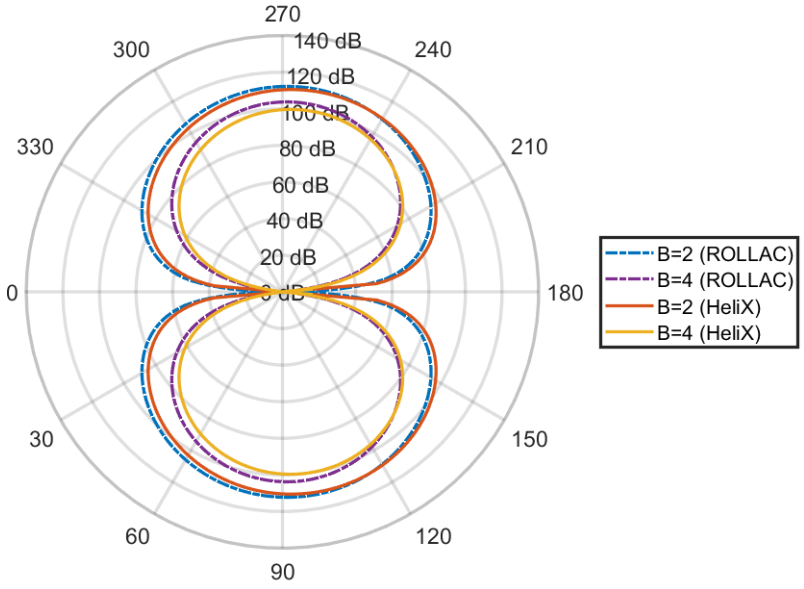

Figure 4.40: Polar plot of SPL as a function of the directivity angle at a distance of 8R from the propeller for different number of blades.

In order to better understand the reduction of the overall noise the thickness noise and the loading noise are looked into. In Figure 4.41 the different noise components in the HeliX tool are shown for both two-bladed and four-bladed configuration. The SPL values from the lift component of the loading show a significant decrease in noise when increasing the number of blades. The maximum perceived SPL value is reduced from 110.5 dB to 105.5 dB for the lift component of the loading and is obtained at a slightly different angle. The angle at which the maximum SPL is obtained for the lift component of

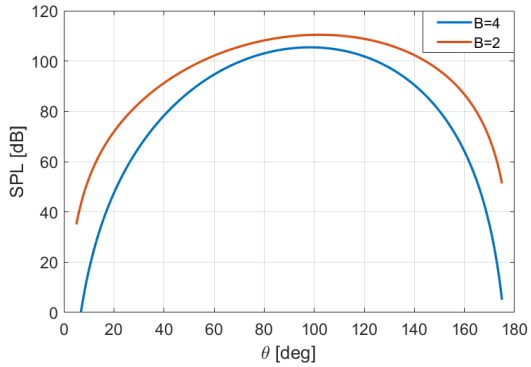

(a) SPL values obtained from the lift component of the loading using HeliX

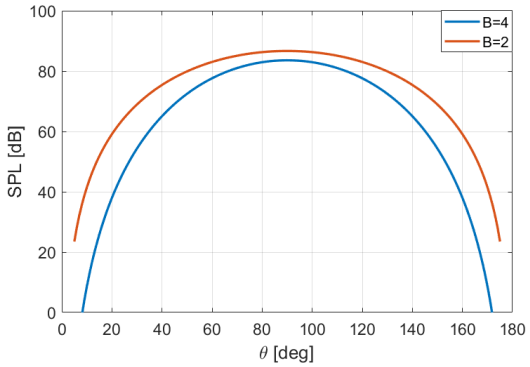

(b) SPL values obtained from the drag component of the loading using HeliX

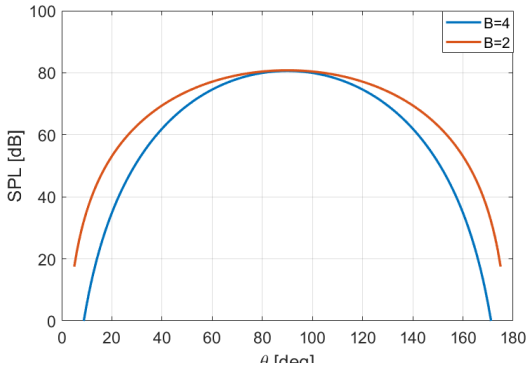

(c) SPL values of the thickness component obtained using HeliX

Figure 4.41: SPL as a function of the directivity angle θ obtained using HeliX for different number of blades at a distance of 8R.

the noise is shifted from 102 degrees to 99 degrees. For the drag the maximum SPL is obtained at an angle of 90 degrees and no shift is seen when increasing the number of blades. Again the maximum SPL value is decreased from 86.7 dB to 83.6 dB. Hence the loading noise is decreased. Now for the thickness noise an increase in noise was expected. However the difference in maximum SPL value that is obtained with two blades or four blades is small. This might be explained by the radiation efficiency. In the helicoidal surface theory an indicator of the radiation efficiency J_{mB}, also known as the Bessel function, is present. An increase in the number of blades means different arguments and order for which the Bessel function of the first kind is computed. This leads to another radiation pattern as can be seen in Figure 4.41. For the two-bladed configuration the besselfunction has an order of 2 and for the four-bladed configuration the order is equal to 4 for the first harmonic. The argument of the Bessel function in the helicoidal surface theory is equal to $mBzM_t \sin\theta$. Hence changing the number of blades also affects the value for the Bessel function. In Figure 4.42 the value of the besselfunction is depicted for the first harmonic of the two-bladed and four-bladed SR-2 propeller. It can be seen that the values for the Bessel function are lower for the four-bladed configuration compared to the two-bladed configuration. This can explain why the thickness noise is not increased significantly when increasing the number of blades.

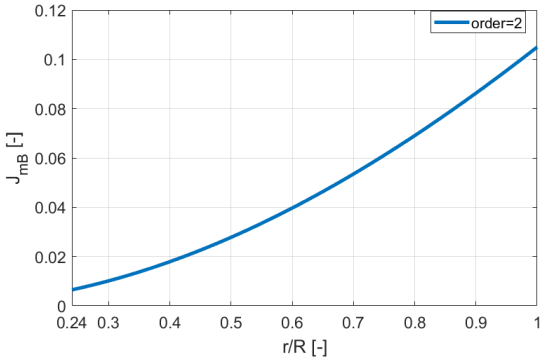

(a) Bessel function as a function of $\frac{r}{R}$ for order 2

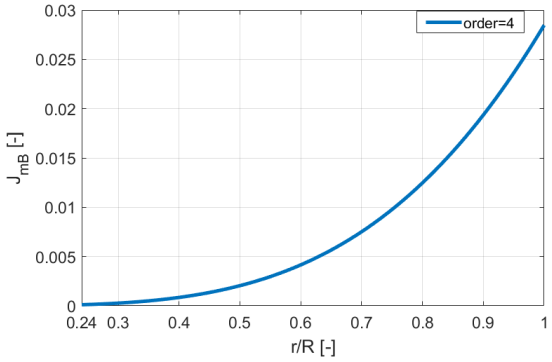

(b) Bessel function as a function of $\frac{r}{R}$ for order 4

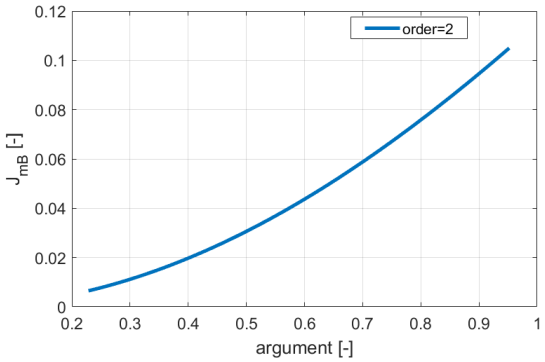

(c) Bessel function with on the x-axis the argument $mBzM_t \sin\theta$ for order 2

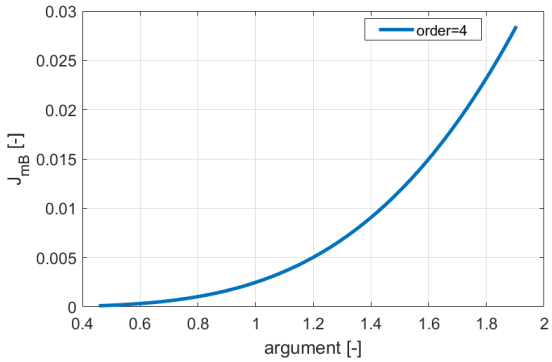

(d) Bessel function with on the x-axis the argument $mBzM_t \sin\theta$ for order 4

Figure 4.42: Bessel function of the first kind for different number of blades and order for $\theta = 90$.

The second design parameter that is evaluated is the propeller diameter. Increasing the propeller diameter reduces the blade load. The area of the blade is increased and the load per unit area is decreased. In order to make a fair comparison, again two blade configurations are chosen. Both with the same number of blades but with different diameter. For this comparison another operating condition is chosen which resembles take-off conditions. The operating condition is shown in Table 4.16.

M_x	0.2
J	1.1
M_H	0.605
Thrust setting [N]	467
number of blades B	4

Table 4.16: Operating condition used in the additional comparison between the HeliX-tool and the NLR-tools

In Table 4.17 the performance coefficients, blade angle, BPF, rpm and diameter of the two propeller configurations are shown. All propellers are set to generate a thrust value of 467 N. Therefore it is required to adjust the blade angle in order to have the same thrust value and compare the propellers fairly. The thrust can be computed from the thrust coefficient using equation 2.7 or 2.12. Thus the thrust is dependent on the thrust coefficient, diameter, number of revolutions per second and density.

$$Thrust = C_T \rho n^2 D^4 \tag{4.8}$$

	HeliX		MAEPROP	
Diameter [m]	0.622	0.7775	0.622	0.7775
C_T [-]	0.2506	0.1601	0.2506	0.1601
C_P [-]	0.4180	0.2343	0.3684	0.2178
$\beta_{0.75}$ [deg]	36	31.7	35.8	31.7
BPF [Hz]	401	321	401	321
rpm [-]	6016	4813	6016	4813
efficiency η [-]	0.66	0.75	0.75	0.81

Table 4.17: Performance coefficients and blade angle for the four-bladed SR-2 propeller with different diameter obtained from the HeliX-tool and MAEPROP

Two diameters are used in the computation of the performance and noise for this comparison. It is decided to use the original 0.622 meters diameter and increase this with 25% for the comparison which results in 0.7775 meters diameter. The chord length is increased as well in order to maintain the chord to diameter ratio of the SR-2 propeller. The blade loading is reduced when the diameter is increased. For a thrust requirement of 467 N the propeller with a larger diameter requires less power to generate the thrust as is obtained from the power coefficients in Table 4.17. Comparing the performance coefficients obtained from MAEPROP with HeliX shows that the efficiency obtained from MAEPROP is higher. This is due to the power coefficient being lower than the power coefficient computed using the HeliX-tool. while having the same thrust coefficient. The blade angles don't differ much from each other and show good agreement. Also an increase in efficiency is obtained when increasing the diameter. This is obtained from MAEPROP as well as the HeliX-tool. In Figure 4.43 the spanwise lift distribution can be seen for the two different diameter dimensions. The spanwise lift distribution shows a reduction in lift when increasing the diameter. Hence, the blade loading is reduced.

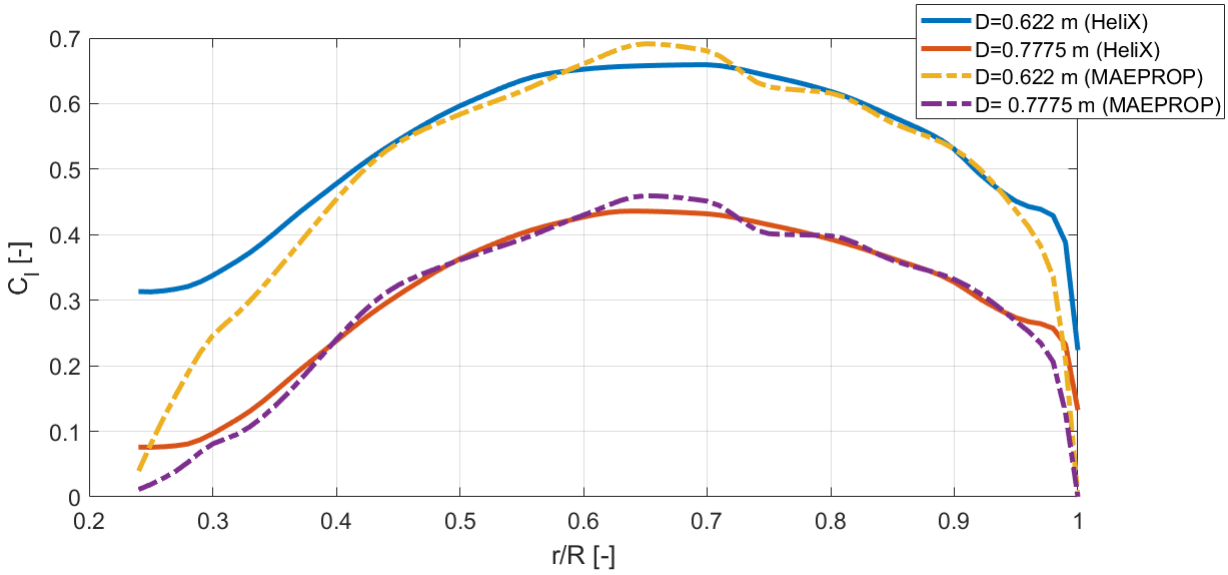

Figure 4.43: Spanwise lift distribution for the two propeller with different diameter as is computed using HeliX and MAEPROP

Increasing the diameter leads to a higher efficiency at the chosen operating speed and is beneficial during take-off. Next to the benefits obtained for the performance, it also helps to reduce the noise which will be shown next. In Figure 4.44 a polar plot is depicted showing the first harmonic for both propeller diameters. The reduction in noise is noticeable from both tools. A maximum reduction of approximately 5 dB is achieved when increasing the diameter with a factor of 1.25 for this operating condition and thrust setting. A more zoomed in view can be found in Figure 4.45.

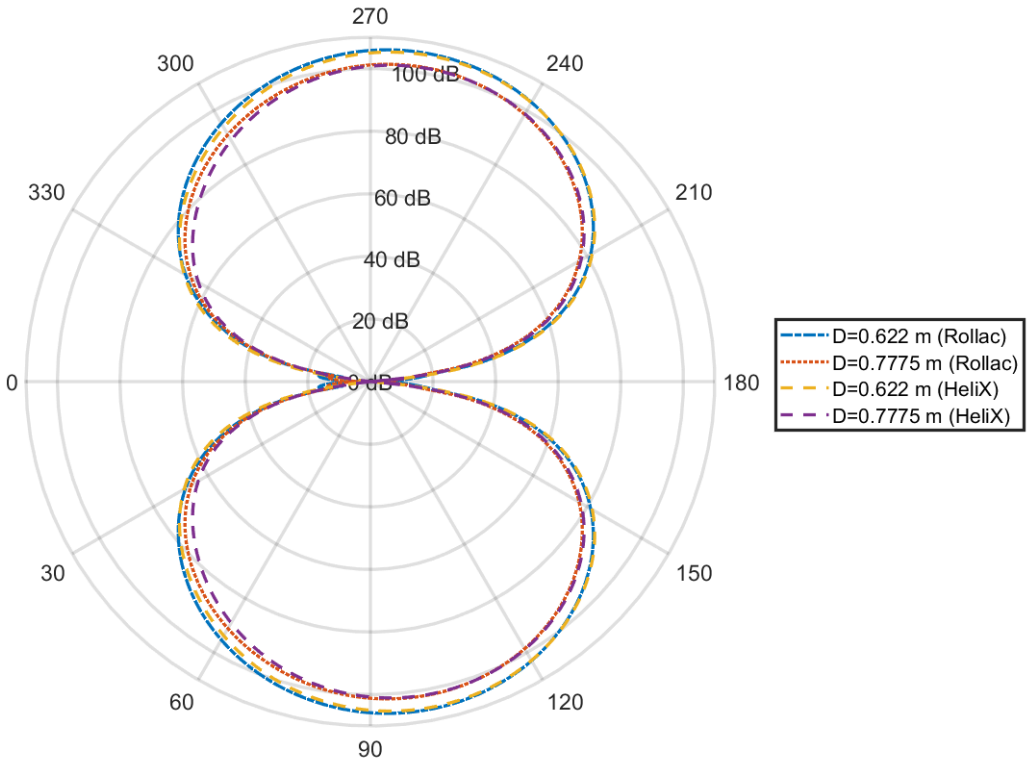

Figure 4.44: Polar plot of SPL as a function of the directivity angle at a distance of 8R from the propeller axis of rotation for two diameters dimensions

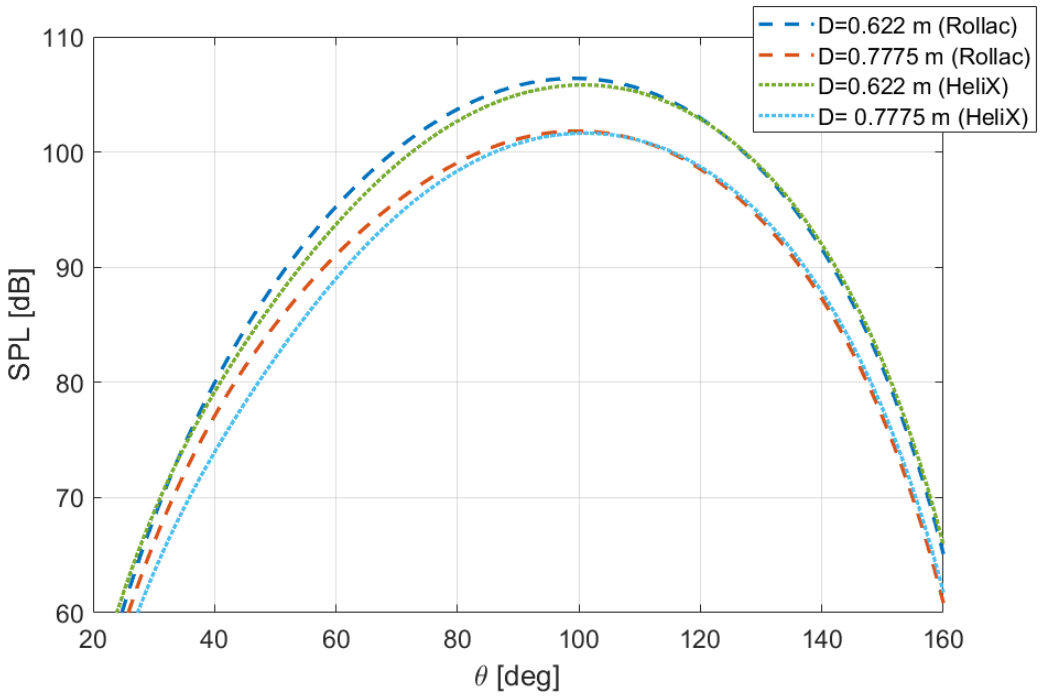

Figure 4.45: SPL as a function of the directivity angle θ for different diameter dimensions at a distance 8R from the propeller axis of rotation

This confirms that indeed the noise can be reduced by increasing the diameter. Furthermore, the

efficiency can also be improved with this which is beneficial during take-off condition at which a high thrust setting is required.

So far, mainly the first harmonic is used in the comparisons. Therefore the last section of this comparison is dedicated to the higher harmonic numbers. Before discussing the comparison a comment must be made on the acoustic noncompactness and the computation of the noise for the higher harmonics. A blade element can be considered acoustically compact when the differences in path length to a field point are negligible compared to the wavelength. If this is the case the computations are simplified. If the blade element isn't acoustically compact, the details of the source must be acounted for. In the helicoidal surface theory the acoustic noncompactness is taken into account. The noise cancellation due to acoustic noncompactness is shown for the loading noise in Figure 4.50. The chordwise wavenumber k_x is a measure of chordwise noncompactness. When the chordwise wavenumber is small the chordwise interference vanishes. Increasing the chordwise wavenumber results in significant chordwise interference and hence noise cancellation. The chordwise wavenumber increases for higher harmonic numbers (higher frequencies) or number of blades.

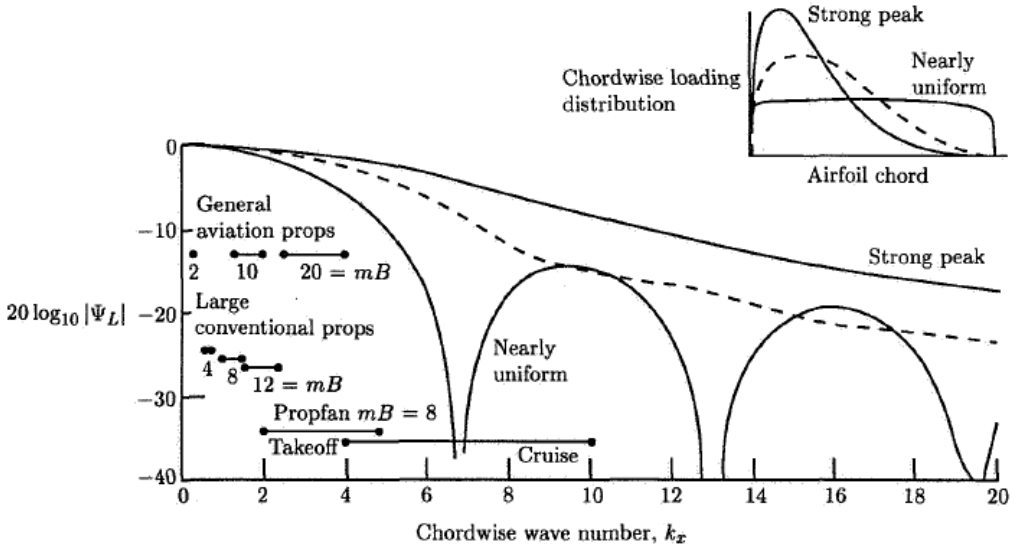

Figure 4.46: Effect of chordwise loading distribution for a blade element due to chordwise noncompactness [13]

The initial assumption made for the chordwise loading is that is has an uniform loading for drag and a strong peaked chordwise distribution for the lift. Since the drag normally has a small contribution to the overall noise, the focus is put on the chordwise lift distribution. Two chordwise lift distributions are compared. One with a uniform distribution and one with a strong peak as can be seen in Figure 4.47. When an integration is performed with the lower limit being the trailing edge (x=-0.5) and the upper limit the leading edge (x=0.5) for both distributions an area of 1 is obtained. This is a requirement in the helicoidal surface theory [13]. Judging from Figure 4.50 the difference between the two loading distributions is more prominent for high chordwise wavenumbers. Hence an eight-bladed configuration of the SR-2 propeller is chosen which results in high values for the chordwise wavenumber. The operating condition chosen for this is M_x=0.32 and J=1.52. This operating condition results in high values for chordwise wavenumber and thus a higher possibility to obtain the effect of acoustic noncompactness. The corresponding chordwise wavenumbers are depicted in Figure 4.48.

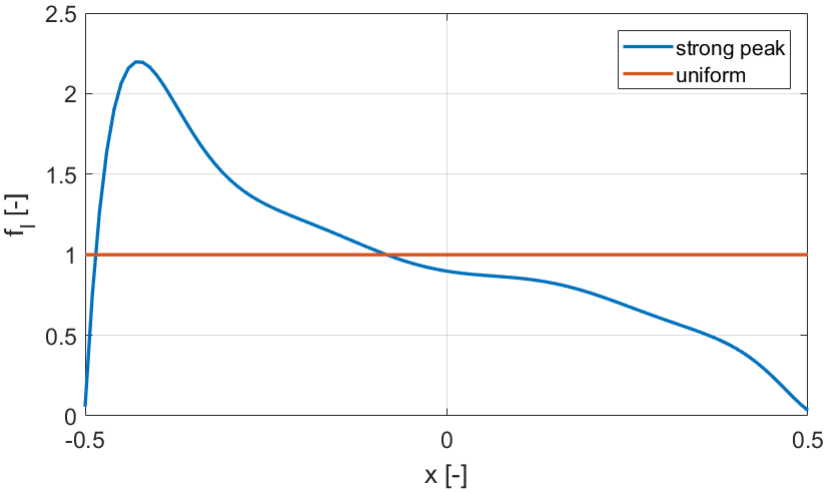

Figure 4.47: Chordwise lift distribution with a uniform distribution and with a strong peak.

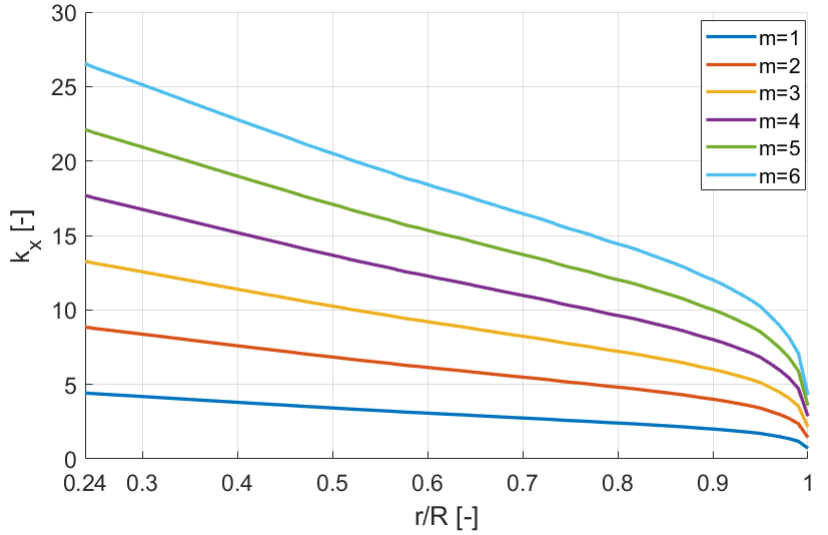

Figure 4.48: Chordwise wavenumber k_x as a function of $\frac{r}{R}$ with B=8, M_x = 0.32 and J=1.52 and $\beta_{0.75}$=57 deg

In Figure 4.49 six harmonics are depicted as a function of the directivity angle. The difference between the two chordwise lift distributions can clearly be seen at the higher harmonics. For the first two harmonics the difference is negligible. For higher harmonic numbers the deviation increases. It is therefore important to take into account the chordwise load distribution correctly when high harmonic numbers are required for the analysis. Especially when the number of blades is large, the acoustic noncompactness effect is more prominent.

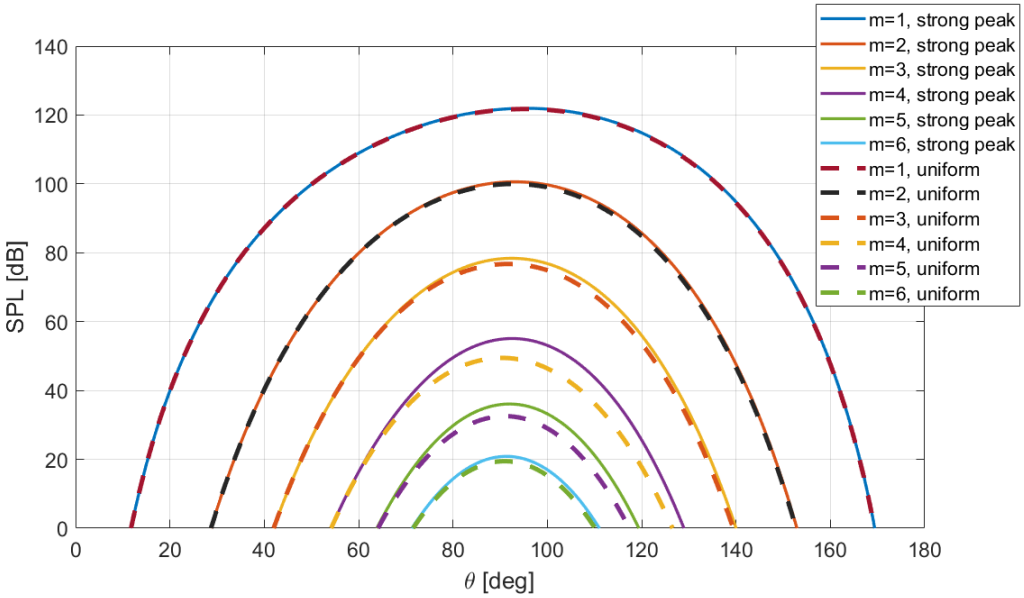

Figure 4.49: Multiple harmonics obtained from the HeliX-tool using an uniform chordwise lift distribution and a strong peak chordwise distribution with B=8 at a distance of 4R from the propeller axis of rotation M_x = 0.32, J=1.52, BPF = 929 Hz and $\beta_{0.75}$=57 deg.

Both Rollac and the HeliX-tool have the capability to compute higher harmonics. For this comparison the operating condition shown in Table 4.16 is used since the performance is already validated for this condition. The configuration used for this comparison is the four-bladed propeller with a diameter of 0.622 meters. The distance from the source is chosen to be 4R from the propeller axis of rotation. In Figure 4.50 6 harmonics are depicted with the corresponding SPL values. A decay is obtained when the harmonic number is increased. This is as expected. The agreement between the harmonics obtained from Rollac and the HeliX-tool is good for the first two harmonics. Overall the direcitivity pattern does agree well with the ones obtained from Rollac. For higher harmonics the deviations increase between the SPL values obtained from the HeliX-tool and Rollac. This may be due to the acoustic noncompactness as is explained before. In Figure 4.51 the chordwise wavenumber is depicted as a function of the spanwise radial position. It can be seen that near the tip the chordwise wavenumber decreases. This is due to the fact that the local Mach number increases from the root to the tip. Recalling equation 3.9 shows that the local Mach number is in the denominator and thus a decrease in chordwise wavenumber should be obtained when this increases. Finally, the Bessel function also contributes to the decay that is observed for the higher harmonics. As is explained before the Bessel function decreases when the order is increased which happens for higher harmoncs.

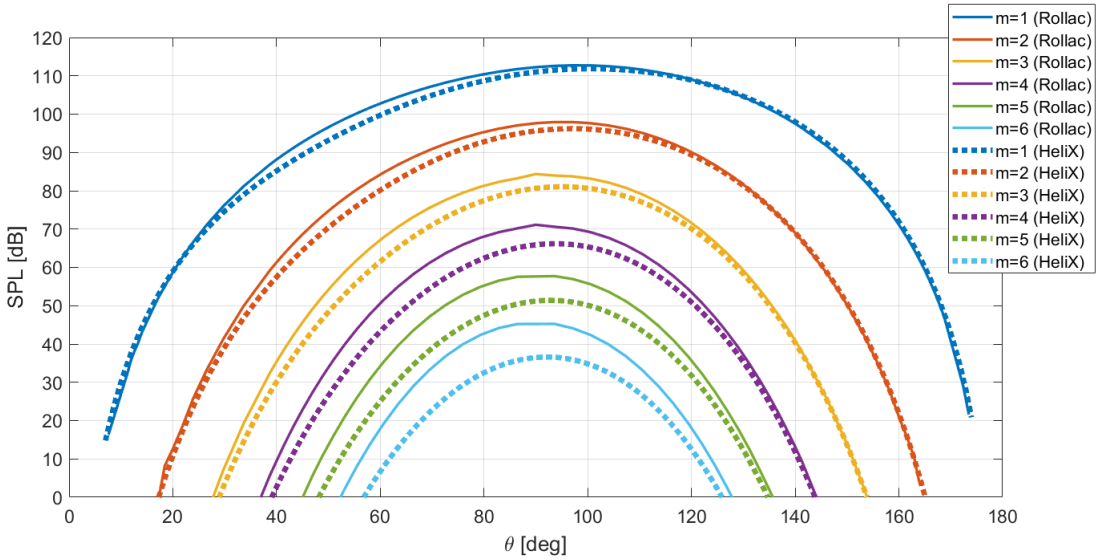

Figure 4.50: Multiple harmonics obtained from the HeliX-tool and Rollac showing the SPL as a function of θ for m=1-6 at distance 4R from the propeller axis of rotation

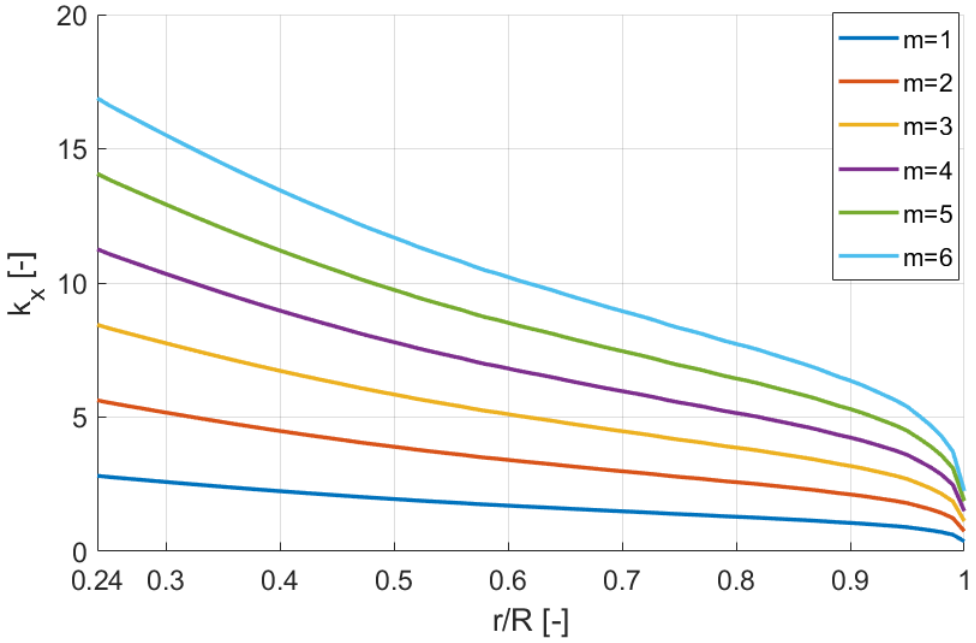

Figure 4.51: Chordwise wavenumber k_x as a function of $\frac{r}{R}$ with B=4, M_x = 0.2 and J=1.1

Overall the agreement for higher harmonics obtained from the HeliX-tool with the harmonics obtained from Rollac show good agreement for the first few harmonics. For higher harmonics the deviation increases. Fortunately the most dominant harmonic always is the first harmonic. Therefore this doesn't have a big effect on the maximum overall SPL that is observed. However it is recommended to perform more validation for the higher harmonics with data obtained from experiments. Higher harmonics can be important when for instance an auralization of the predicted noise needs to be performed. Finally a more detailed chordwise loading distribution might be taken into account. This can be done by using the local angle of attack. This can then be used to perform an iteration step and to run XFoil again for this current angle in order to be able to obtain the correct chordwise lift distribution. This is not implemented yet in the current version of the HeliX-tool.

4.3.3. Final remarks on the validation

In this section some remarks based on the foregoing comparisons are given.

The aerodynamic part of the computation is validated using both literature data and MAEPROP. In general a good agreement is found for subsonic operating conditions. For the power coefficient a recurring deviation is obtained when comparing the HeliX-tool and MAEPROP. It seems that the power coefficient obtained from the HeliX-tool consistently is larger than the one obtained from MAEPROP. This has to do with the way the drag is computed by both tools. For the HeliX-tool a drag model is used which also takes into account drag rise when exceeding the critical Mach number for example. In the HeliX-tool the drag has a quadratic dependence on the lift and additionally uses a separated drag model for regions outside the linear lift range (stall). In MAEPROP a simple empirical relation is used to compute the drag. For this only the local lift coefficient is needed. The drag computed by the HeliX-tool often is larger than the one computed using MAEPROP resulting in a higher power coefficient. The lift in MAEPROP is determined using the local angle. The lift curve is a linear one as no stall is taken into account in MAEPROP. In the HeliX-tool this is taken into account and blade elements can be stalled. Nevertheless the agreement of the spanwise lift coefficient in general is good.

Both tools share that the aerodynamics of the propeller is computed using a lifting line method. This means that the results that are obtained from the aerodynamic part don't include a chordwise pressure distribution or loading distribution. For the HeliX-tool this is required for the computation of the noise. Therefore some assumptions are made for the chordwise loading distribution. For the lift a strong peak chordwise distribution is used. For the drag an uniform chordwise distribution is assumed. Instead of using the assumed distribution it is also possible to use the computed local angle of attack of the blade elements and run XFoil again for the corresponding blade section and angle. This results in a chordwise loading distribution which corresponds more with the reality. This becomes more important for higher harmonics where the effect of acoustic noncompactness becomes more prominent. Nevertheless, it is found that the assumed chordwise loading distribution results in satisfactory data.
Another common thing for both tools is the Prandtl-Glauert compressibility correction. As is explained before the use of this correction should be done with care. The correction can be considered valid until a Mach number of 0.7. For higher Mach number more dedicated compressibility corrections should be used. When high Mach numbers are present large deviations can be expected. This is partly due to the deviations obtained for the aerodynamics part. Also non-linear effects arise at high Mach numbers which are not taken into account in the current version of the HeliX-tool. These do require more sophisticated aerodynamic input data since quadrupole sources need to be modelled for this.

Several comparisons are made for the noise. All results that are obtained in this chapter exclude the effect of the Doppler factor. This is because in all cases the source and observer are not moving with respect to each other. Therefore no correction is needed to be applied for the Doppler shift. The comparisons consisted of data that is obtained from in-flight measurements and wind-tunnel data. It is important to fully understand the setting in which the measurements are taken before trying to recreate the results using the HeliX-tool. Measured data is often affected by factors that are not taken into account in the HeliX-tool. For the in-flight measurements these factors can be inflow distortion, angle-of-attack effects and other noise sources [13]. Angle-of-attack effects lead to unsteady loading of the blade and thus to unsteady sources. The HeliX-tool only includes the steady sources. Other noise sources that can occur during in flight measurements are for instance airframe noise or noise from other parts of the engine. Also for the measurements that are performed in the wind-tunnels attention must be paid. Not all wind-tunnels are acoustically treated. This can lead to noise being reflected which affects the measured data. Another aspect that needs special attention is when microphones are placed outside of the jet. This leads to the waves being refracted as the waves travel through the shear layer.

Several observations are made when comparing both tools with literature data. Rollac is a near-field tool and the HeliX-tool is based on a far-field theory. Hence Rollac performs better when data is measured in the proximity of the propeller. It is important to check whether the data is measured in the near-field or in the far-field. This can make a difference in the SPL values that are obtained. Furthermore, for transonic Mach numbers the deviations in noise increase. This is possibly due to other

sources being more prominent and also the fact that nonlinear effects arise. The HeliX-tool is found to perform better when local Mach numbers are lower than 0.7. The agreement at these Mach numbers is good with Rollac. This is tested for several distances from the propeller axis of rotation and for different propeller configurations.
Final observations made regarding Rollac is that it can be applied up to a distance of approximately 10R from the propeller. In addition, when the wavelength becomes equal to the chord length the theory of the lifting line is no longer valid. Hence high harmonic numbers can't be obtained as the wavelength decreases for higher frequencies. The highest harmonic number that is achieved using Rollac is 6.

5

Auralization

Auralization is the process of transforming a source noise prediction into an audible result. In this chapter the application of the HeliX-tool is shown by using it to simulate a fly-over of a propeller by means of an auralization. This process involves several steps which are briefly described. In the following sections the auralization process is outlined starting with a source noise signal which is described in section 5.1. In section 5.2 the propagation steps are treated that are taken into account for the auralization. These are taken into account as signal processing steps which use a so called Gain, Time delay and Filter (GTF). Finally the result of an audible simulation of a propeller is presented.

5.1. Source Noise

The source noise of the propeller is computed using the HeliX-tool. The HeliX-tool computes the harmonic or tonal contribution of the noise of a propeller. The source noise is defined as a hemisphere that contains the spectral content of the noise at a constant distance r away from the noise source as is depicted in Figure 5.1. In the HeliX-tool the range of angles for which the spectral content is computed can be chosen. During a fly-over the source moves relative to the observer and hence the emission angle changes. When the emission angle lays within two angles for which the HeliX-tool computed the noise than a linear interpolation between the points is made. Note that at this stage the noise source is computed without the Doppler shift correction that is used in the Helicoidal Surface theory. This is done delibaretely since the Doppler effect is taken into account as a time delay which will be explained together with other propagation effects in the following sections.

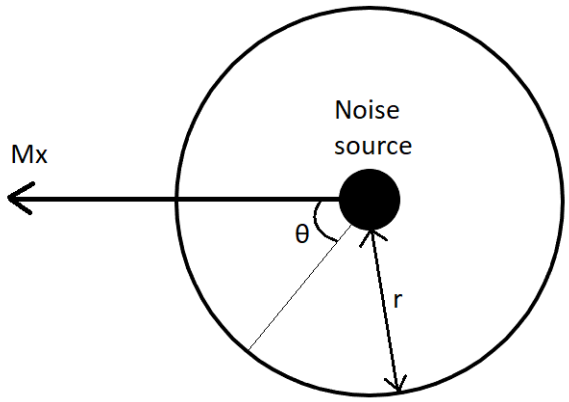

Figure 5.1: Schematic of noise source for which the spectral content is known at a constant distance r from the source

5.2. Propagation Effects

The noise that is observed by the receiver is different from the noise that is emitted by the source. Due to propagation effects the noise signal generated by the propeller is altered. The propagation effects that are considered here are the ground reflection, Doppler effect, atmospheric absorption and spherical spreading.

Ground Reflection

Reflection occurs when an object is located between the source and observer. For the auralization that is performed in this chapter the reflection is assumed to be caused by the ground. The reflection is assumed to be 100% for the analysis performed in this chapter. The sound that propagates from the source to the observer is modeled using two ray paths. Each has a different path length and is denoted by r_1 and r_2 as can be seen in Figure 5.2.

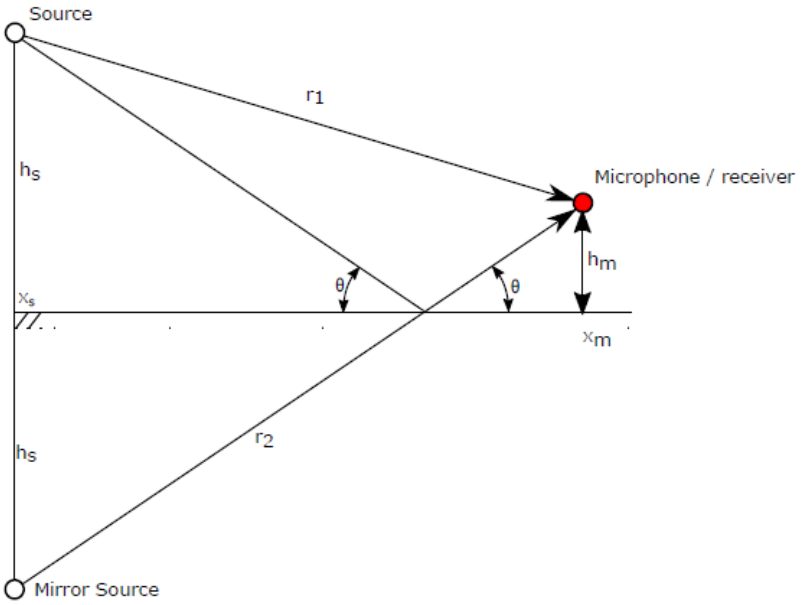

Figure 5.2: Schematic of noise source and the receiver showing the direct path of a sound ray and the reflected path which are both taken into account for the auralization [8].

Doppler Frequency Shift

When a source is moving relative to the observer, a shift in the frequency is perceived by the observer. This can be calculated using

$$f_o = \frac{f_s}{1 - M_x \cos\theta}, \tag{5.1}$$

where f_o is the frequency perceived by the observer and f_s is the frequency at the source. When sound is emitted by a source, it takes some time to travel the distance to the receiver. The amount of time it takes for the observer to receive the noise signal can be calculated since the path length and speed of sound is known. Instead of using equation 5.1 the Doppler effect can also be taken into account using a variable time delay. Each ray path has a separate source signal and receiver signal. A difference between the two sound rays is the travel time to get to the receiver. By using a Variable Delay Line a signal can be delayed and the time a signal needs to travel from the source to the observer can be incorporated [8]. When applying this for moving sources, it effectively incorporates the Doppler shift.

Atmospheric Absorption
Atmospheric absorption occurs due to the fact that sound energy is absorbed when it travels through the atmosphere. This is mainly caused by internal friction in the air. The rate at which sound energy is absorbed depends on the sound attenuation coefficient. The sound attenuation coefficient is a function of the frequency, temperature and humidity. In Figure 5.3 the atmospheric attenuation factor α is depicted as a function of the frequency. The transmission loss can then be computed using equation 5.2.

$$\Delta SPL = \alpha \Delta r \tag{5.2}$$

Where α is the atmospheric attenuation factor in dB per meter and Δr is the distance that the sound ray travels, i.e. path length . The atmospheric attenuation is incorporated by applying an atmospheric filter on the signal. This is done for the direct and reflected sound rays.

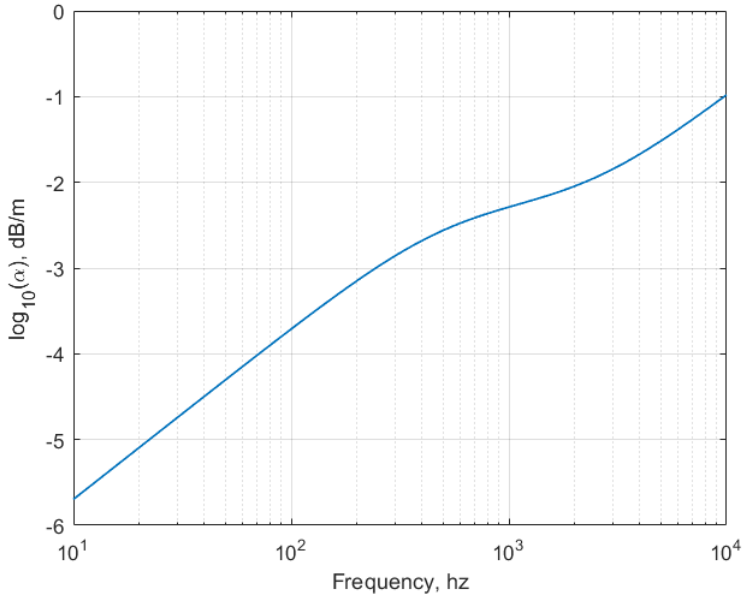

Figure 5.3: The atmospheric attenuation factor α for relative humidity RH = 80%, p=101200 Pa and T=293.15K

Spherical Spreading

Spherical spreading leads to a decrease of the amplitude of the sound. The amplitude of the sound is inversely proportional to the distance of the source. The spherical spreading can be incorporated by using a gain. A gain is used to multiply the signal by a factor that can amplify or attenuate a signal. In the case of spherical spreading the gain is equal to 1/r where r is the path length. Note that the path length is different for the direct and reflected sound ray.

The above mentioned propagation effects are taken into account using the signal processing steps that are shown in Figure 5.4.

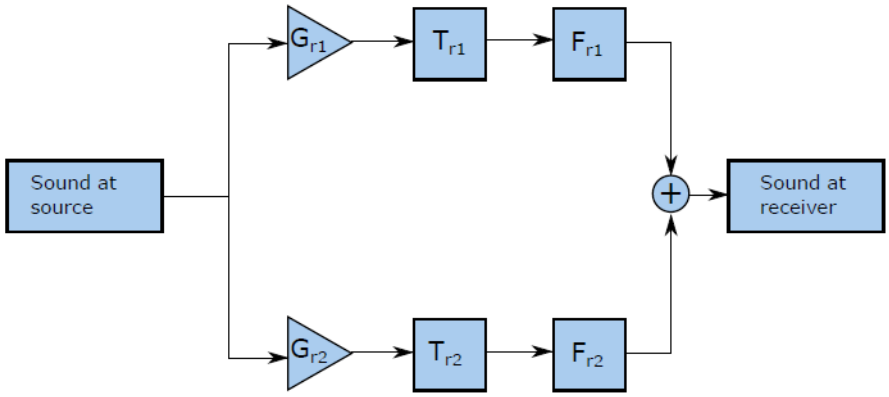

Figure 5.4: Schematic showing the signal processing steps used to incorporate the propagation steps. For this a Gain, Time delay and atmospheric Filter is applied for both the direct path and the reflected path [8].

5.3. Result of the auralization

The propagation effects discussed in section 5.2 are successfully implemented in the HeliX-tool. These are used to generate a propeller fly-over. The operating condition that is selected for the auralization is similar to take-off conditions of a turboprop aircraft. A description of the operating condition can be seen in Table 5.1.

M_x	0.23
J	1.1
M_H	0.69
M_T	0.65
$\beta_{0.75}$	33.5 deg

Table 5.1: Operating condition used for the auralization obtained from the HeliX-tool

The propeller configuration used for the auralization has the following parameters as can be seen in Table 5.2.

B	6
D	3.66 meters

Table 5.2: SR-2 propeller configuration parameters used for the auralization

The propeller configuration used is inspired by the Fokker 50 propeller. The diameter is 3.66 meters and the number of blades is 6 which is similar to that of the Fokker 50 propeller. Using the operating condition from Table 5.1 and the configuration from Table 5.2 the performance coefficients for this condition are computed. These can be seen in Table 5.3.

C_T	0.2652
C_P	0.4164

Table 5.3: Performance coefficients obtained using the operating condtion from table 5.2

With the operating condition known, the source noise is computed. This is done by using sufficient amount of data points at a constant distance away from the source. This distance is chosen to be 4R and an increment of 1 degree is used for the computation of the source noise. This means that at a distance 4R from the propeller noise source, noise data is known for angles ranging from 10 to 170 (as the noise during the fly-over is observed below the source) with increments of 1 degree. It is chosen

to use this range of angles as the propeller noise source at a certain altitude above the receiver would need to be at a infinite distance away from the source in order have an angle of 0 or 180 degrees. Angles ranging from 10 to 170 are found to be sufficient for this. If more data points are needed for the noise source then this can be changed easily. During a fly-over the emission angle changes. Therefore the spectrum of the noise source changes. It is possible that the emission angle is at an angle where no data points are computed. By means of linear interpolation between two known adjacent data points the amplitude of a single tone is then determined. Finally a summation is used to add the different tones resulting in the total tonal acoustic pressure. This technique is known as additive synthesis.

Using the operating condition and the propeller configuration parameters results in the following

$BPF[Hz]$	117.6
rpm	1175.7

The next step in the auralization process is defining the propeller fly-over. The fly-over is defined as a steady flight at a constant altitude. The altitude is chosen to be 304.8 meters. By default a pressure time signal of 30 seconds is generated. Therefore the starting point of the fly-over is defined by the following

$$x_s = \frac{-V_x\, t_{end}}{2}, \tag{5.3}$$

where x_s is the x-coordinate of the position of the propeller noise source at the beginning of the fly-over. See Figure 5.2 for a schematic. For the current operating condition this results in an x_s of approximately 1183 meters to the left of the receiver.
After the source noise data is known and the fly-over is defined the signal processing steps are executed. As is explained before, two ray paths are used. These are used to take into account ground reflection. The direct and reflected path of a sound ray are used to correct for the spherical spreading. This is corrected using a gain element. The effect of this is that the source noise signal is attenuated since the distance between the source and receiver is bigger than the distance (4R) for which the source noise is computed. Note that the path length of the direct and reflected sound ray are different and therefore the gain correction is different for the two paths. Furthermore, the angles of the direct and reflected path also differ as can be seen in Figure 5.2. After the spherical spreading is incorporated, the next step is to apply the time delay filter is applied. This incorporates the Doppler frequency shift. Finally the atmospheric filter is applied to correct the signal for atmospheric absorption. The result of the signal processing steps can be seen in Figure 5.5. The reduction in acoustic pressure can clearly be seen due to the spherical spreading and atmospheric absorption. Also the effect of the time delay filter can be seen as the maximum perceived acoustic pressure is shifted slightly to the right.

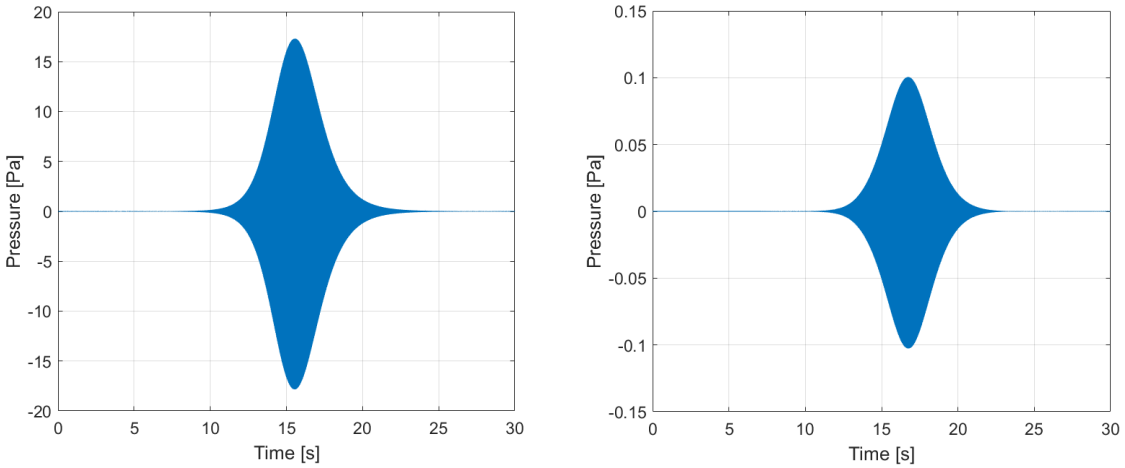

(a) Pressure time signal of the direct path at the source before the signal processing steps are executed

(b) Filtered pressure time signal at the receiver obtained after the signal processing steps are executed.

Figure 5.5: Pressure time signal obtained from the fly-over

The filtered time pressure signal of the propeller is used to generate an audible simulation of the propeller fly-over and a spectrogram. Figure 5.6 shows the frequency content of the propeller fly-over signal as a function of the time. When the signal from the two paths, with different delays, are summed an interference pattern emerges which can be observed. Only the tonal components are taken into account in this version of the HeliX-tool which can clearly be seen in Figure 5.6. Furthermore the effect of spherical spreading and atmospheric absorption are also noticeable since the high frequency noise are filtered out for a great part. Finally the Doppler frequency shift is also noticeable. From 0 to 15 seconds the propeller is approaching the receiver. From 15 to 30 seconds the propeller is moving further away from the receiver. Hence resulting in a higher frequency for the first part and a lower frequency of the second part.

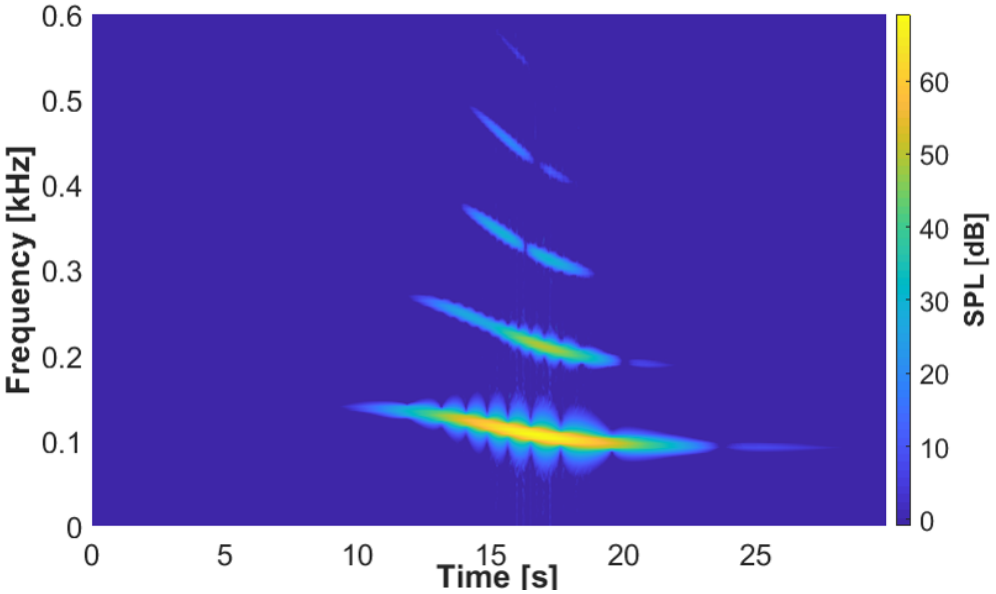

Figure 5.6: Spectogram of the propeller fly-over in isolated condition with a total duration of 30 seconds. altitude = 304.8 meters, sampling frequency fs = 44100 Hz, height of receiver = 1.8 meters

6

Conclusion & Recommendations

In this chapter the conlusion of the work performed is described. Also, recommendations regarding the research are given for future improvements.

The objective of this master thesis was the implementation and validation of a source noise model for propellers with a future goal of being integrated in a tool like the VCNS or an aircraft design chain. The ability to compute the noise coming from a certain propeller design can be used for optimization purposes of a propeller design. Also, the predicted noise can be used for auralization. The focus is put on the harmonic noise contribution and therefore the following propeller noise sources are considered:

- Steady loading noise
- Thickness noise

For the calculation of these noise sources it is chosen to implement the Helicoidal Surface theory developed by Hanson. The Helicoidal Surface theory was found to be suitable for a fast prediction of the harmonic noise sources of a propeller in the far-field. Furthermore in several studies the Helicoidal Surface theory is proven to generate promising results. The result of this implementation is the HeliX-tool which is based on the Helicoidal Surface theory for the acoustic part and uses XFoil in combination with XRotor for the aerodynamics part of the propeller. The implementation of the theory together with the two tools is successfully performed in Matlab.

The validation is performed using data from literature and using two NLR tools, MAEPROP and Rollac. MAEPROP is used to validate the aerodynamics part of the propeller and Rollac is used to compute the acoustic part of the propeller. For the validation the SR-2 propeller is selected which is a propeller that is extensively studied and developed by NASA. The validation of the propeller performance shows a good agreement between the MAEPROP and HeliX-tool. From the comparisons that are made it can be concluded that the overall agreement with MAEPROP is good provided that the operating conditions result in local Mach number that are below the transonic Mach numbers (<0.7 Mach). For Mach numbers that are in the transonic region or sonic region, non-linearity starts to become more prominent. This is not taken into account in the current version of the HeliX-tool and hence large deviations can be expected in this region.

For a good prediction of the acoustics a good prediction of the aerodynamics of the propeller is needed. Several comparisons are made. Comparisons are made with literature data that is collected during an in-flight measurement. Other data that is used comes from wind-tunnel measurements. The agreement with the data that is obtained during an in-flight measurement is bad. This can be due to several factors. One is the operating condition that is used. With local Mach numbers varying between 0.73 to 0.95 non-linear effects arise. This is not incorporated in the HeliX-tool. Furthermore, the measurements are taken very close to the source which can mean that the data is measured in the near-field. The HeliX-tool is based on a far-field theory which means that deviations can be expected. Furthermore, no performance data of the propeller is measured during the in-flight measurements which makes it

hard to check whether the computed performance is close to reality. Finally, other noise sources like air-frame noise or installation effects can be present during the measurements which are not taken into account in the noise prediction of the HeliX-tool. In the HeliX-tool the propeller is considered in isolated conditions with axial inflow.
The comparisons that are made with wind-tunnel data showed a better agreement. Overall the predicted directivity pattern is in line with the measured one and also with the computed one by Rollac. For operational conditions that result in Mach numbers that are lower than Mach numbers in the transonic region, a good agreement is found with the data as well with Rollac. The deviations obtained for the performance part of the propeller increase when higher Mach numbers are present. The aerodynamics of the propeller are used as input for the acoustic computations and therefore also larger deviations are obtained for the acoustic results. Also, often wind-tunnels are not acoustically treated and no damping material is used. This can lead to reflections being present in the wind-tunnel which affects the measured data. Nevertheless, the data from the windtunnel is measured in a more controlled environment compared to that of the in-flight measurement and is therefore considered to be useful.

Additional comparisons for operating conditions and design parameters that are not treated in the literature data are made using the NLR-tools and the HeliX-tool. An analysis is performed using different number of blades. Both HeliX-tool and MAEPROP showed similar results for the performance. The effect of changing the number of blades on the acoustics is checked. Increasing the number of blades for a certain operating condition resulted in lower SPL values. Similar results are obtained from the HeliX-tool and Rollac. Next to changing the number of blades, the diameter is also altered to see whether both tools show similar results. This was indeed the case which confirms that the HeliX-tool is implemented correctly. Increasing the diameter of the propeller results in a reduction of the loading. Therefore the loading noise is reduced and lower SPL values for all radiation angles are obtained. Furthermore a comparison is made using higher harmonic numbers. A good agreement is found for the first few harmonics. The decay that is observed for higher harmonics is larger for the HeliX-tool than that of Rollac. Therefore the deviation for the acoustics between Rollac and the HeliX-tool increases for higher harmonic numbers. It was found that this could possibly be explained by the Bessel function which is an indicator of the radiation efficiency. Rollac is based on a near-field theory which uses another form of the Bessel function. Finally, the acoustic noncompactness effect is shown and evaluated by means of changing the chordwise lift distribution. It is found that the acoustic noncompactness effect becomes more important for higher harmonics.

Subsequently, the HeliX-tool is applied to perform an auralization. The auralization is successfully performed and only contains the tonal contributors of the propeller noise. The auralization is performed taking into account several propagation effects. The propagation effects taken into account are: spherical spreading, ground reflection, atmospheric absorption and the Doppler shift. The propagation effects are implemented by means of signal processing steps that consist of a gain element, time delay filter and an atmospheric filter. The result of the auralization is an audible simulation of a propeller fly-over and a spectrogram in which the propagation effects can clearly be noticed.

Some recommendations can be stated for future research with regard to the HeliX-tool. The current version computes the steady harmonic noise sources of a propeller in isolated configuration. An assumption that is made is that the propeller is at zero angle of attack. In reality there can be an inclination of the inflow with respect to the propeller disk. This inclination, i.e. angle of attack results in a non-uniform inflow and can change the noise levels and directivity significantly. For future research it is suggested to take these unsteady sources into account. Furthermore, installation effects can also significantly alter the aerodynamics and acoustics of the propeller. It is therefore suggested to analyze the effect of installation effects on the propeller noise.
The performance or aerodynamics of the propeller are computed using XFoil and XRotor. XFoil computes the 2D aerodynamic properties of a blade section. In reality the propeller is rotating and the flow is affected by the centrifugal and Coriolis forces that act on the boundary layer flow of the propeller. The 2D aerodynamic data of the blade sections is not corrected for this and therefore it is recommended to perform this correction. Another recommendation on the use of XFoil can be made. XFoil tends to have difficulties finding a converging solution for blade sections that have a small thickness, typically smaller than 3%. It is recommended to improve the stability of XFoil for thin blade sections.

XRotor is also used for the computation of the aerodynamics of the propeller. Some recommendations on the use of XRotor can be given. The chordwise loading and critical Mach number used during the calculations are assumed. It is recommended to perform an iteration and determine the chordwise loading using the local angle of attack, velocity and Reynolds number obtained from XRotor. Furthermore, for local Mach numbers above 0.7, the Prandtl-Glauert compressibility is considered no longer to be valid. It is therefore suggested to use more dedicated prediction codes at these kind of speeds. Also when these kind of speeds are used, quadrupole sources become more important and therefore should be implemented in the HeliX-tool.
The propeller used during the validation of the tool is a straight bladed propeller. It might be interesting to see how the HeliX-tool performs for propellers with other blade designs. Some deficiencies of XRotor came to light when a propeller with sweep is selected. According to the documentation of XRotor, the vortex formulation can be used for propellers with sweep. However, no geometric input for the sweep is supported in the version of XRotor that is used.
Finally a recommendation on the auralization is given. The auralization is performed using only the tonal contributors. It is recommended to also include broadband noise as this makes the sound of the audible simulation more realistic. Also the higher harmonics are important for the auralization. It is therefore recommended to perform more validation for the higher harmonics. Regarding the audible result made during the auralization, it might be interesting to compare this with real recordings of a fly-over of propeller driven aircraft. The same propeller geometry as the aircraft should then be implemented in the HeliX-tool.

Bibliography

[1] ATR, *Turboprop market forecast 2016-2035,* (2016).

[2] Bombardier, *Market forecast 2017-2036,* (2017).

[3] R. Atılgan, Ö. Turan, Ö. Altuntaş, H. Aydın, and K. Synylo, *Environmental impact assessment of a turboprop engine with the aid of exergy,* Energy **58**, 664 (2013).

[4] ICAO, *Aviation benefits 2017,* (2017).

[5] E. R. Boeker, E. Dinges, B. He, G. Fleming, C. J. Roof, P. J. Gerbi, A. S. Rapoza, J. Hermann, *et al.*, *Integrated noise model (INM) version 7.0 technical manual*, Tech. Rep. (United States. Federal Aviation Administration. Office of Environment and Energy, 2008).

[6] M. Arntzen, H. Visser, D. Simons, and T. van Veen, *Aircraft noise simulation for a virtual reality environment,* in *17th AIAA/CEAS Aeroacoustics Conference (32nd AIAA Aeroacoustics Conference)* (2011) p. 2853.

[7] M. Arntzen, L. Bertsch, and D. G. Simons, *Auralization of novel aircraft configurations*, Tech. Rep. (National Aerospace Laboratory NLR, 2015).

[8] M. Arntzen, *Aircraft noise calculation and synthesis in a non-standard atmosphere*, Tech. Rep. (National Aerospace Laboratory and Delft University of Technology, 2014).

[9] L. L. M. Veldhuis, *Propeller wing aerodynamic interference*, Ph.D. thesis, TU Delft, Delft University of Technology (2005).

[10] A. Filippone, *Aircraft noise prediction,* Progress in Aerospace Sciences **68**, 27 (2014).

[11] A. Filippone, *Advanced Aircraft Flight Performance* (Cambridge : Cambridge University Press, 2012).

[12] M. Schulz and L. Laube, *Identification of noise sources in a turboprop engine bay,* in *16th AIAA/CEAS aeroacoustics conference* (2010) p. 3852.

[13] B. Magliozzi, D. B. Hanson, and R. Amiet, *Aeroacoustics of Flight Vehicules: Theory and Practice,* NASA Reference Publication 1258, Vol. 1 WRDC Technical Report 90-3052 **1** (1991).

[14] J. H. Miles, *Separating direct and indirect turbofan engine combustion noise using the correlation function,* Journal of propulsion and power **26**, 1144 (2010).

[15] A. Sahai, *Consideration of Aircraft Noise Annoyance during Conceptual Aircraft Design*, Ph.D. thesis, RWTH Aachen University (2016).

[16] L. Bertsch, D. G. Simons, and M. Snellen, *Aircraft Noise: The major sources, modelling capabilities, and reduction possibilities*, Tech. Rep. (Delft University of Technology, 2015).

[17] R. H. Self, *Propeller noise,* Encyclopedia of Aerospace Engineering (2010).

[18] G. J. Ruijgrok, *Elements of aviation acoustics* (Delft University Press, 1993).

[19] J. E. Marte and D. W. Kurtz, *A Review of Aerodynamic Noise From Propellers, Rotors, and Lift Fans.* NASA JPL Technical Report 32-1462 (1970).

[20] G. Chirico, G. N. Barakos, and N. Bown, *Numerical aeroacoustic analysis of propeller designs,* The Aeronautical Journal **122**, 283 (2018).

[21] R. Schlinker and R. Amiet, *Helicopter rotor trailing edge noise,* in *7th Aeroacoustics Conference* (1981) p. 2001.

[22] H. Blackburn, *Quadrupoles in potential flow: two model problems,* Journal of Fluid Mechanics **116**, 507 (1982).

[23] A. B. Parry, *Theoretical prediction of counter-rotating propeller noise*, Ph.D. thesis, University of Leeds (1988).

[24] D. Hanson and M. Fink, *The importance of quadrupole sources in prediction of transonic speed propeller noise.* Journal of Sound and Vibration , 19 (1979).

[25] D. J. K. Hanson, *Helicoidal surface theory for harmonic noise of propellers in the far field,* AIAA Journal **18**, 1213 (1980).

[26] M. Drela and H. Youngren, *Xrotor user guide 2003,* (2003).

[27] P. Klein, *Parametric Modeling and Optimization of Advanced Propellers for Next-Generation Aircraft*, Master's thesis, TU Delft (2017).

[28] M. Hepperle, *Javaprop users guide,* (2010).

[29] C. N. Adkins and R. H. Liebeck, *Design of optimum propellers,* Journal of Propulsion and Power **10**, 676 (1994).

[30] M. Drela and H. Youngren, *Xfoil 6.94 user guide,* (2001).

[31] J. D. Anderson Jr, *Fundamentals of aerodynamics* (Tata McGraw-Hill Education, 2010).

[32] M. E. Goldstein, *Aeroacoustics,* New York, McGraw-Hill International Book Co., 1976. 305 p. , 305 (1976).

[33] G. L. Stefko and R. J. Jeracki, *Wind-tunnel results of advanced high-speed propellers at takeoff, climb, and landing mach numbers,* (1985).

[34] M. Hepperle, *Javafoil user's guide,* (2017).

[35] H. Brouwer, *On the use of the method of matched asymptotic expansions in propeller aerodynamics and acoustics,* Journal of Fluid Mechanics **242**, 117 (1992).

[36] H. Brouwer, *A lifting line model for propeller noise,* in *12th Aeroacoustic Conference* (1989) p. 1079.

[37] N. Ben Nasr, F. Falissard, J. Decours, R. Gaveriaux, Y. Delrieux, S. Canard-Caruana, M. Laban, H. Brouwer, M. Albreicht, C. Scholz, *et al.*, *Propeller analysis using low & high fidelity aero-acoustic methods,* in *35th AIAA Applied Aerodynamics Conference* (2017) p. 3573.

[38] J. Kooi and W. de Wolf, *Aerodynamic measurements on a 1/5 scale model of the Fokker 50 propeller and comparison with theoretical predictions* (NLR, 1990).

[39] P. LASAGNA, K. MACKALL, and R. COHN, *In-flight acoustic test results for the sr-2 and sr-3 advanced-design propellers,* in *19th Joint Propulsion Conference* (1983) p. 1214.

[40] J. H. Dittmar, *Further comparisons of wind tunnel and airplane acoustic data for advanced design high-speed propeller models,* The Journal of the Acoustical Society of America **77**, S76 (1985).

[41] D. B. Hanson, *Influence of propeller design parameters on far-field harmonic noise in forward flight,* AIAA Journal **18**, 1313 (1980).

[42] J. H. Dittmar, B. J. Blaha, and R. J. Jeracki, *Tone noise of three supersonic helical tip speed propellers in a wind tunnel,* The Journal of the Acoustical Society of America **65**, S139 (1979).

[43] D. B. Hanson, *Near-field frequency-domain theory for propeller noise,* AIAA journal **23**, 499 (1985).

[44] P. Block, *Experimental study of the effects of installation on singleand counter-rotation propeller noise,* (1986).

[45] B. M. Brooks and F. Metzger, *Acoustic test and analyses of three advanced turboprop models,* (1980).

[46] B. Brooks, *Acoustic measurements of three prop-fan models,* in *6th Aeroacoustics Conference* (1980) p. 995.